

# Modeling of tides and spreading of saline water in the Arabian Gulf and in the coastal area of Abu Dhabi with a flexible mesh model

---

Master thesis  
Frank Bosch van Drakestein



## Abstract

The coastal area of Abu Dhabi is characterized by a complex network of tidal channels and shoals. This area is rapidly evolving, and the increasing amount of desalination plants to provide the growing population with fresh water can have large consequences for the local ecology through the emission of highly saline water. In this study, tidal motion and the spreading of salt released by desalination plants in the Abu Dhabi area and the adjacent Arabian Gulf are investigated with the help of several numerical models, which use either a conventional curvilinear or an unstructured (finite volume) grid. The software that was used for modelling with unstructured grids (D-Flow FM) is still under development. Therefore this software is compared to conventional software as well.

In the first part of this study, the Arabian Gulf is represented as a rectangular basin, for which an analytical solution is available (Taylor, 1920). Different numerical models, which employ curvilinear and unstructured grids, have subsequently been used to simulate tides for that same idealized configuration. It was found that both Delft3D and D-Flow FM compare well and that they simulate overall tidal propagation patterns well.

In the second part, numerical models (using structured and unstructured grids) are discussed that simulate the Arabian Gulf using realistic coastlines and bathymetry. All models compare well to observations, and D-Flow FM has been found to be suitable for building a detailed model of the coastal waters around Abu Dhabi.

In the third and last part the fine-resolution, unstructured grid model around the area of Abu Dhabi is used to describe the spreading of highly saline water discharged by desalination plants. The results indicate that the effect of a single desalination plant is widespread. Close to a desalination plant a dynamic salinity equilibrium is reached approximately 2 months after the desalination plant started to emit brine. The flushing time and the residence time of salt have been computed for a channel neighboring a desalination plant. The total salt transport is separated in a mean and fluctuating part and fluctuations in salinity and water transport are found to be dominant at locations where the bathymetry or coastline varies strongly.

## Table of Contents

Abstract .....	2
1. Introduction .....	4
2. Material and Methods.....	8
2.1 The Arabian Gulf.....	8
2.2 Theory.....	10
2.3 Software .....	15
2.4 Methods of analysis.....	19
2.5 Transport of salt applied to the Abu Dhabi region .....	22
3. The Arabian Gulf as a rectangular basin .....	24
3.1 Setup of the experiment.....	24
3.2 Analytical solutions of amphidromic points.....	26
3.3 Modeling the amphidromic points using square cells in Delft3D.....	28
3.4 Modeling the amphidromic points using square cells in D-Flow FM.....	30
3.5 Modeling the amphidromic points using a mesh with triangular cells.....	31
3.6 Square cells versus triangular cells: some conclusions with regard to the simulation of a simplified analytical model.....	33
4. The Arabian Gulf using realistic geometry.....	34
4.1 Setup of the experiment.....	34
4.2 Numerical simulation of the Arabian Gulf.....	36
5. Modeling the Abu Dhabi area .....	40
5.1 Setup of the experiment.....	40
5.2 Model comparison with observations of the sea level.....	43
5.3 Spreading of salt in the coastal waters of Abu Dhabi .....	44
6. Conclusions .....	49
7. Acknowledgements .....	50
8. References.....	51
Appendix A. Qualitative details of grid building in Delft3D and D-flow FM .....	56
A1. The curvilinear grid as used by Delft3D .....	56
A2. The unstructured grid as used by D-Flow FM.....	56
Appendix B. The collocation method.....	60
Appendix C. Details of the alpha amphidromic points .....	62
Appendix D. Grids used for modeling the Arabian Gulf.....	64
Appendix E. Tidal motion in the Arabian Gulf .....	66

## 1. Introduction

Abu Dhabi is a city in the Middle East, bordering the Arabian Gulf (also known as the Persian Gulf), which is rapidly expanding. The quickly growing ports, airports and large increase in buildings and factories impose a large strain on the coastal waters around Abu Dhabi. In 2007 the large desalination plants produced more than 2.3 million cubic meter of fresh water per day, which accounted for 36% of the total water production (Environmental Agency Abu Dhabi, 2009). These desalination plants produce highly saline water with an elevated temperature as a byproduct, which is released into the coastal waters that are already salty due to the high evaporation and low rainfall in the area. In addition, these effluents contain chemicals that are used in the desalination process which can be toxic. A chlorine concentration that was more than 10 times the amount toxic to humans was found 1 km from a desalination brine outlet. The effluents can have a strong adverse effect on the flora and fauna (Hashim & Hajjaj, 2005). Sun et al. (2012) modeled the discharge of desalination plant effluent in Korea and concluded that an outlet should be as far as 0.5 km away from the coast in order to prevent harmful effects on the ecosystem. Since the winter cooling of the extremely saline waters near the United Arab Emirates strengthens the baroclinic exchange of the Arabian Gulf through the Strait of Hormuz (Kämpf & Sadrinasab, 2005), desalination plants might even affect Gulf wide water motion. This means that in order to effectively protect the environment



Figure 1-1: The Arabian (Persian) Gulf (google earth).

while not negatively influence the expanding city of Abu Dhabi, an accurate knowledge of the behavior of saline effluents in the coastal waters of is necessary. However, before it is possible to study flow patterns, and subsequently the behavior of effluents, it is important to have knowledge of the general water motion in the nearest large sea: The Arabian Gulf.

The Arabian Gulf (Figure 1-1) is a relatively small sea that is bounded on three sides by coasts, and its only connection to the great oceans is through the Strait of Hormuz. Since in a small sea like this the direct tidal effect is negligible, the tidal large tidal motion that is present in Gulf comes in from the large oceans through this Strait. This tidal motion is the dominant force that drives the water motion in the Gulf: it is more than ten times as high as any other driving mechanism (Reynolds, 1993). The tide in the Arabian Gulf is diurnal to semi-diurnal, of which the semi-diurnal  $M_2$  component is the strongest. It is this diurnal to semi-diurnal pattern which, like in the rest of the Gulf, determines the major water motion patterns of seawater in the coastal waters of Abu Dhabi.



Figure 1-2: Abu Dhabi and its coastal waters. From: Google earth.

Because of this strong dominance of the tides on the Gulf wide water motion it is this pattern that will determine where effluents produced by (desalination) plants will go. Therefore, a good understanding of the tides in the Arabian Gulf is required if one tries to determine the pathways followed by the effluents.

The increasing strains on the coastal waters of the ever growing Abu Dhabi require a good legislation that controls the issuing of permits for the building of factories, desalination plants etc. But in order to judge accurately what the environmental effects of a new plant on the areas neighboring the coastal waters will be, and hence whether a permit should be given out, the development of a model

that accurately predicts the flow in the coastal waters of Abu Dhabi is indispensable. The government of Abu Dhabi has realized this and has asked the company ARCADIS to set up the basics of such a model. This thesis is part of that project.

In line with the statements above, the aims of this study are outlined as follows:

- i. To develop a clear understanding of the tidal motion in the Arabian Gulf, with a special focus on the dominant components.
- ii. Quantify tidal and residual flow in the coastal area of Abu Dhabi.
- iii. Quantify spreading of salt as emitted by a desalination plant in the coastal area of Abu Dhabi.

The methods for achieving these aims are by (i) simulating tides in both a rectangular basin and a basin with realistic Gulf geometry using D-Flow FM, which employs a flexible mesh, and comparing the results with Delft3D, which uses a curvilinear grid. In the case of the rectangular basin, the results are also compared to an analytical solution. The similarities and differences are identified. (ii) To develop a prototype model of the coastal waters of Abu Dhabi and to analyze the model output of the prototype in terms of tidal constituents (including overtides). (iii) To use the prototype model developed for (ii) and assess the (dynamic) equilibrium pattern of salt concentrations that is present in the coastal waters after the placement of a desalination plant. In addition the mechanisms involved in the spreading of salt are investigated.

Many numerical simulations have been performed in order to describe the water motion in the Arabian Gulf accurately. Some of these models are 2-dimensional depth averaged (2DH) models,

for example (Proctor, et al., 1994), who modeled tidal and meteorological motion in the Arabian Gulf in order to model the spreading of an oil spill, and (Pous, et al., 2012) who reached high model accuracy by applying detailed bathymetry and 7 different tidal constituents at the boundary for the purpose of providing a basis for a more complicated model. Other models of the Arabian Gulf are fully 3-dimensional or 3D models. These 3D models have the advantage that flow governing processes have to be parameterized less, and are hence more accurate, and that certain processes which have a depth gradient are taken into account. One such process is the effect of salinity, which has an effect on the density and hence will be higher in the lower layers of the sea. Without the usage of a 3D model such vertical effects are ignored. Therefore 3D models are more suited for the detailed description of seas in which it is important to understand the effects that such processes have on the overall water motion. Examples of the usage of 3D models in the Arabian Gulf are (Kämpf & Sadrinab, 2005), who tried to find explanations for complicated circulation patterns in the Gulf, and (Elshorbagy, et al., 2006), who studied the general water motion.

The usage of models is also the main approach in this thesis; although in this thesis also an analytical model is used. This is possible because of the shape of the Arabian Gulf, which can be approximated by a rectangle. This analytical model will provide the understanding of the physics that govern the tides in the Arabian Gulf. However, despite providing a good initial understanding, the many simplification involved in the construction of an analytical model prohibit the study of detailed motion. Therefore, for a more comprehensive study of the aims mentioned above, several numerical models have been developed.

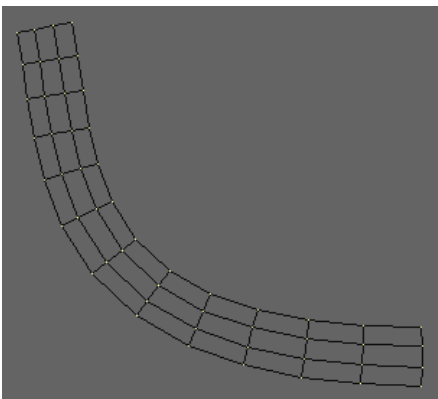


**Figure 1-3: A curvilinear grid: a grid that consists of rectangular cells that are allowed to curve somewhat.**

In order to develop these models use was made of the widely used flow modeling software package Delft3D, which is also the preferred software package of ARCADIS. This software package makes use of a so called curvilinear grid: a grid which consists of rectangles which are allowed to curve somewhat (Figure 1-3). However, the Abu Dhabi region has a very complicated coastline and bathymetry, with many small islands (see Figure 1-2) which makes it hard to model with curvilinear grids. The recent rise of so called finite element and finite volume solving techniques provides an alternative to the usage of rectangular cells. This method, as opposed to the traditional finite difference method used on curvilinear grids, can work with grids that are irregular and unstructured. This ability has two

major advantages over the finite difference method: it can follow the coastline more accurately and it allows for local refinement. In this way, the general practice of nesting models in order to get the required accuracy in a specific area is not required any longer. Although of course with respect to computation times this might still be necessary. The finite volume method was already usable for field problems in the mid-sixties (Gupta & Meek, 1996), but has only recently become interesting to commercial parties. With advancing numerical techniques the usage of the finite volume method is now starting to appear in many different kinds of software. With respect to ocean modeling, this method has already been used successfully for many years by, among others, the software package FVCOM (for details see Chen (sd)). Examples of studies that used FVCOM with considerable success are the modeling of radioactive cesium in the coastal waters of Japan after the Fukushima disaster (Lai, et al., 2013) and for the modeling of tidal dynamics (Chen, et al., 2011). Other main software packages that use this technique are Mike 21 (Warren & Bach, 1992); (Johnson, et al., 2005), and

ADCIRC (Luettich, et al., 1992); (Blain, et al., 2002). All of these software packages have their differences, but all have proven their worth in modeling the flows of shallow seas. Unlike Delft3D and D-Flow FM, which are both open source software, ADCIRC and Mike 21 require a paid license (or paid sub-software) in order to use it. FVCOM is open source but has no graphical user interface (yet) and is harder to use for inexperienced users.

The successor to Delft3D is currently being developed by the company Deltares, which is also the developer of Delft3D, and has the finite volume method incorporated. The working name of this new software package is D-Flow FM. D-Flow FM can use combinations of rectangles with triangles, pentagons etc. Despite being relatively new, a paper by Kernkamp et al. (2011) has been published that describes the technical details of D-Flow FM and validates its accuracy.

The complex geometry of the coastal waters of Abu Dhabi makes it ideally suited for the usage of D-Flow FM, because the generation of curvilinear grids that follow all the smaller and larger channels accurately is undoable. However, D-Flow FM is currently under development and might still have some errors. It is therefore important to test D-Flow FM's performance to that of Delft3D as well as observations.

In order to discuss the research goals in a comprehensive way, and taking into account the notes regarding D-Flow FM, the main body of this thesis was divided into four different parts (chapters 2, 3, 4 and 5 respectively):

1. This section introduces the Arabian Gulf, describes the physics necessary for understanding the research aims described above, and discusses the tools used for the analysis of these aims.
2. In this section that discusses only simple models, and provides a basic insight into the tidal patterns of the Arabian Gulf and the differences of the different modeling tools, the  $M_2$  tide is simulated in a rectangular basin with dimensions comparable to those of the Arabian Gulf. Both the horizontal and vertical tide are discussed.
3. As a more advanced section, this section uses the Arabian Gulf model built by ARCADIS as its foundation. In this section this model, which uses realistic boundaries and bathymetry, is compared to observations of the sea level and to equivalent D-Flow FM models that use both curvilinear grids and grids with triangular cells. The main focus is to study the large scale tidal motion in the Arabian Gulf of the dominant tidal constituents.
4. This section discusses detailed tidal motion in the coastal waters of Abu Dhabi. In addition to this, a scenario is discussed in which highly saline water is released into the ocean at an arbitrary location, thus simulating a desalination plant. In order to do this one of the Flexible Mesh models developed in the preceding section, after it has received a strong local refinement around the Abu Dhabi area, is used.

## 2. Material and Methods

Before going to the results it is important have an idea of the physics of the study area and to discuss in some more detail the tools that are used to achieve the research aims. This chapter serves that purpose. Section 2.1 gives an introduction to the Arabian Gulf, with a special focus on what is important for this study: the tides. In this way a clear starting point is defined that is used throughout the rest of this thesis. Section 2.2 describes the physics that apply to the motion of water and the simplifications made to them so that the Arabian Gulf might be represented by those physics. Sections 2.3 and 2.4 go into more detail about the tools that are used to study the tides and the transport of saline water in the Arabian Gulf and the Abu Dhabi area. Of these sections, section 2.3 focusses on the software used (Delft3D and D-Flow FM) and mentions some other similar software as a reference. Section 2.4 deals with analysis methods that are used to assess the output of the software packages. Details of how salt is transported in the ocean, including several time scales that describe this transport, are discussed in section 2.5.

### 2.1 The Arabian Gulf

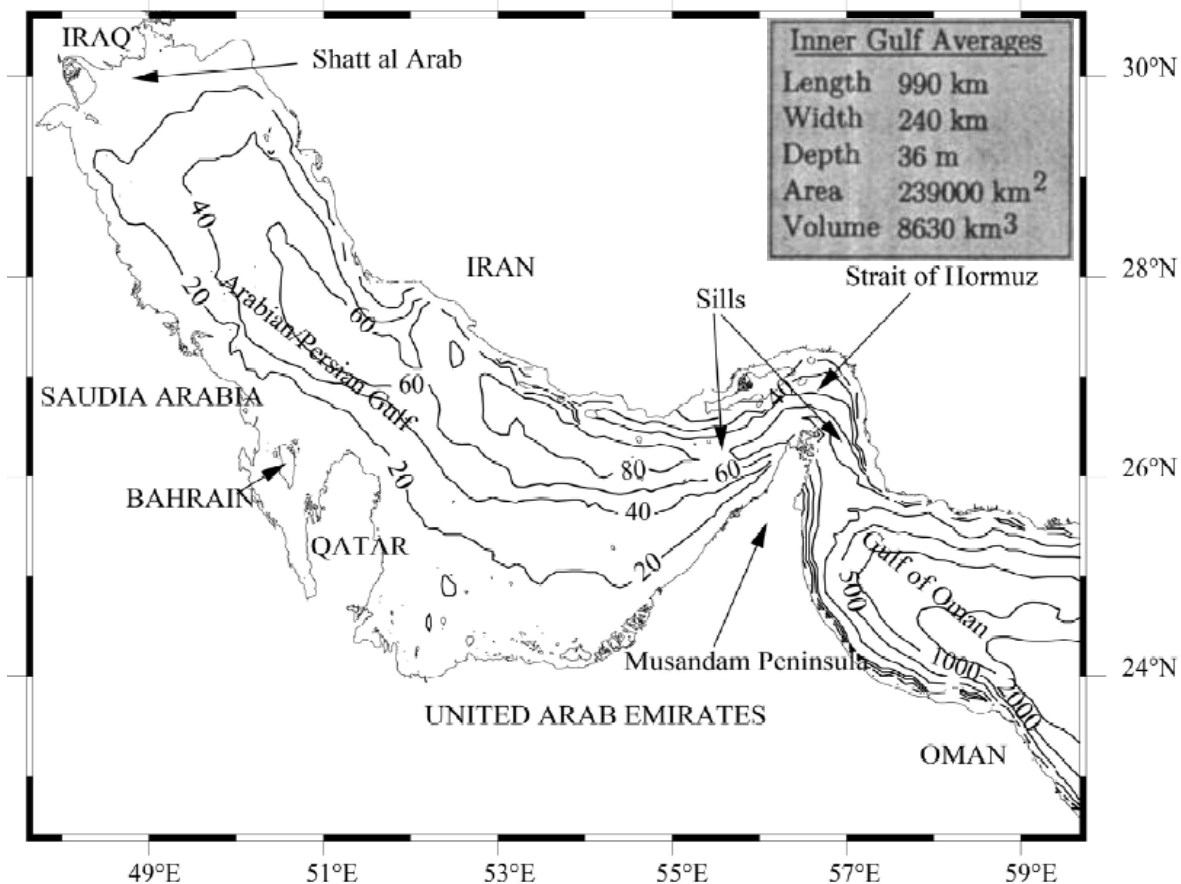


Figure 2-1: The bathymetry of the Arabian Gulf in meter and some landmarks. From: (Pous, et al., 2012). In the top right corner some averages of the Inner Gulf (Reynolds, 1993) are displayed.

The Arabian Gulf is a shallow sea surrounded by land and is connected to the Gulf of Oman through the 56 km wide Strait of Hormuz. The Gulf of Oman in turn connects to the Indian Ocean and hence the only connection of the Arabian Gulf to the larger ocean basins is the very narrow Strait of Hormuz. The Arabian Gulf is bordered by Iran, Qatar, Bahrain, Saudi-Arabia, Kuwait, Iraq and the United Arab Emirates. The latitude of the Arabian Gulf is between 24°N and 30°N. In a paper Reynolds (1993), describes an extensive survey of the Arabian Gulf, including, but not limited to, bathymetry, salinity, temperature and velocity measurements. The Arabian Gulf has an average

**Table 2-1: The maximum amplitudes of the 4 major tidal components in the Arabian Gulf, as inferred from the charts by (Admiralty co-tidal Atlas Persian Gulf, 1999)**

Tidal component	Maximum amplitude (m)
M <sub>2</sub>	1
S <sub>2</sub>	0.3
K <sub>1</sub>	0.5
O <sub>1</sub>	0.3

length of 990 km, an average width of 240 km and an average depth of 36 m (Figure 1-1). The Arabian Gulf has relatively shallow parts in the northwest and southeast, with depths of less than 20 meter, while close to the coast of Iran an isolated trough of about 80 meter deep is present. In the Strait of Hormuz the Gulf deepens to more than 100 m and it quickly deepens to more than 2000 m in the Gulf of Oman.

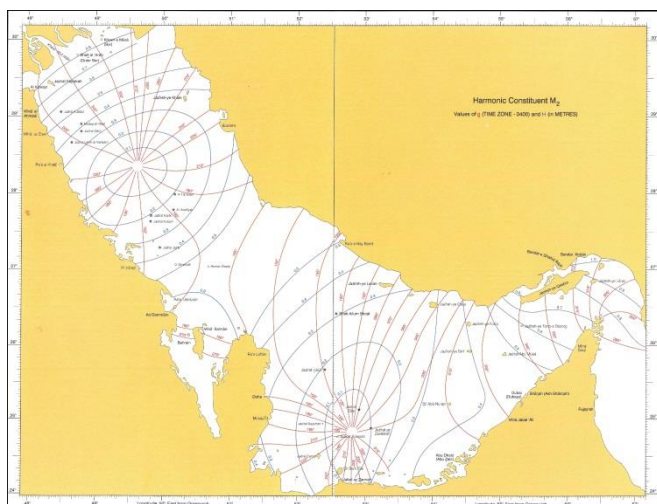
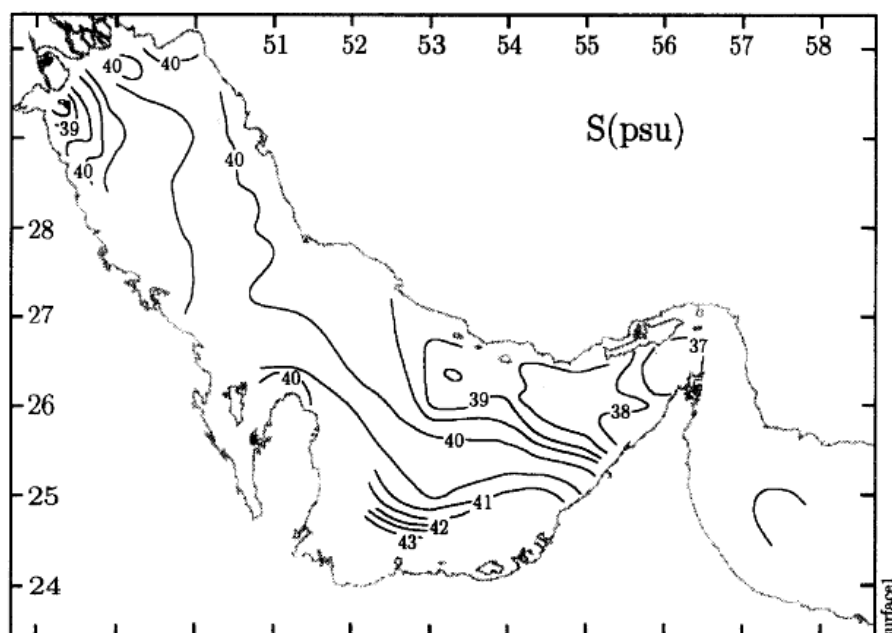


**Figure 2-2: The co-phase lines (in red) and the co-amplitude lines (in blue) of the M<sub>2</sub> tide in the Arabian Gulf. From: (Admiralty co-tidal Atlas Persian Gulf, 1999).**

The Arabian Gulf is a tide dominated sea; the kinetic energy in the tide driven water motion is about 10 times higher than the kinetic energy in wind driven water motion which in turn is about 10 times higher than the kinetic energy in density driven water motion (Reynolds, 1993). However, despite the strong tidal dominance in the Gulf, the net tidal water motion is negligible and residual water motion is mostly caused by the winds and density differences. The tide is predominantly diurnal to semi-diurnal, with the M<sub>2</sub>, S<sub>2</sub>, K<sub>1</sub> and O<sub>1</sub> being the most important constituents. The semi-diurnal M<sub>2</sub> and S<sub>2</sub> components have 2 amphidromic points: one in the northwest of the basin and one in the southeast. The diurnal

K<sub>1</sub> and O<sub>1</sub> components have one amphidromic point in the center of the Gulf (Admiralty co-tidal Atlas Persian Gulf, 1999). Figure 2-2 shows the amphidromic point pattern by displaying the co-phase and co-amplitude lines of the most dominant component in the Arabian Gulf: the M<sub>2</sub> tide. This chart has been created by observations, and interpolated in those locations where no measurements were available. Using the same charts for the other components, in order to give an impression about the amplitudes of the 4 major components, Table 2-1 displays the maximum amplitudes of these components in the Gulf.



The evaporation in the Arabian Gulf is very high. Because of the absence of rivers west of Abu Dhabi, these high evaporation rates lead to especially saline waters in that area (Reynolds, 1993). The highly industrial area of Abu Dhabi with its desalination and power plants discharges very saline water with high temperatures, which lead to even more saline waters

**Figure 2-3: The surface salinity of the Arabian Gulf (psu) during winter. From Reynolds (1993).**

(>43 psu) near Abu Dhabi. Figure 2-3, which shows the salinity of the Arabian Gulf during summer, clearly indicates that the salinity of the Arabian Gulf is higher than that of the Gulf of Oman. In summer this difference reduces somewhat, but it is still present. This dense seawater transported out through of the Arabian Gulf along the bottom and is replaced by less saline water that comes out of the Gulf of Oman along the sea surface.

## 2.2 Theory

An advantage of the shape of the Arabian Gulf, is that it can be approximated by a rectangular basin (see Figure 2-4), which allows for an analytical solution. The computation of an analytical solution of the tide in a rectangular, which is also called a semi-enclosed basin, was first performed by Taylor (1920). Hence this problem is also known as the Taylor problem. However, in

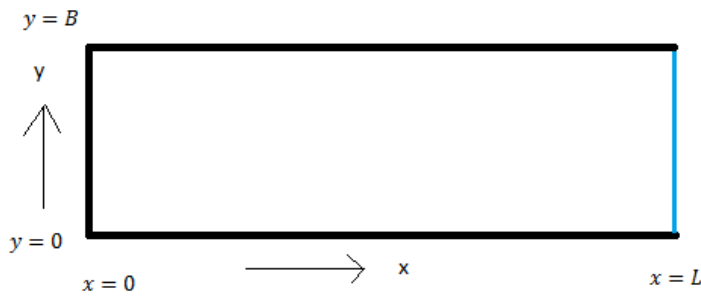


Figure 2-4: The semi enclosed basin that represents the Arabian Gulf that is used in this section.

order to fully understand the physics of the tides in a semi enclosed basin, first a semi-infinite channel that is bounded by two coasts is considered. In Figure 2-4 this would mean that the coast at  $x = 0$  has now become an open boundary, while the sea boundaries are no longer at a fixed location. The starting point is relatively simple: the depth averaged shallow water equations. In an ideal homogenous fluid on an f-plane they

are (see Vallis (2006)):

$$\frac{\partial \eta}{\partial t} + \frac{\partial}{\partial x}(u(H + \eta)) + \frac{\partial}{\partial y}(v(H + \eta)) = 0, \quad 1)$$

$$\frac{\partial u}{\partial t} + u \frac{\partial u}{\partial x} + v \frac{\partial u}{\partial y} - f v = -g \frac{\partial \eta}{\partial x} - r u, \quad 2)$$

$$\frac{\partial v}{\partial t} + u \frac{\partial v}{\partial x} + v \frac{\partial v}{\partial y} + f u = -g \frac{\partial \eta}{\partial y} - r v. \quad 3)$$

Here  $\eta$  is the sea surface elevation,  $H$  is the depth of the flat bottom,  $u$  and  $v$  are the respective components of the velocity in the  $x$  and  $y$  directions,  $f$  is the (constant) Coriolis parameter and  $r$  is a bottom friction parameter. This parameter can be a function of among others the velocity and/or sea level or be a constant, depending on the friction formulation that is used. In order to derive these equations some assumptions have been made, for example a flat bottom and the hydrostatic balance as the vertical momentum equation. In a semi-infinite channel there are 2 boundary conditions:  $v = 0$  at  $y = 0, B$ . When linearizing equations 1)-3) and ignoring friction, these equations become

$$\frac{\partial \eta}{\partial t} + H \left( \frac{\partial u}{\partial x} + \frac{\partial v}{\partial y} \right) = 0, \quad 4)$$

$$\frac{\partial u}{\partial t} - f v = -g \frac{\partial \eta}{\partial x}, \quad 5)$$

$$\frac{\partial v}{\partial t} + f u = -g \frac{\partial \eta}{\partial y}. \quad 6)$$

The linearizing procedure has some important effects, among which is that so-called overtides, which are generated by the nonlinear terms, are ignored. However, in order to solve the

equations analytically, linearization needs to take place. The bottom friction needs not be ignored, and is in fact quite significant for flow patterns. This has been proven in a number of studies, for example (Carbajal, 1997) and (Rienecker & Teubner, 1980). Despite its significance, including frictional effects into this analytical model is beyond the scope of this thesis. The effects caused by ignoring these effects, including a brief discussion of overtides, will be dealt with later in this chapter. The set of equations 4)-6) can be reduced to the so called Klein-Gordon equation:

$$\frac{\partial^2 \eta}{\partial t^2} - gH \nabla^2 \eta + f^2 \eta = 0. \quad 7)$$

This Klein-Gordon equation occurs in many branches of physics. Here, it describes long surface waves that are modified by the earth's rotation: Kelvin, Poincaré and Sverdrup waves. For a full derivation of the above equations the reader is referred to one of the many textbooks on geophysical fluid dynamics, for example Gill (1982), or for an alternative derivation of the three types of waves mentioned above to Vallis (2006).

In a channel of semi-infinite length bounded by coasts on two sides the Poincaré waves become discrete: for a fixed wavenumber  $k$  there is a fixed set of frequencies  $\sigma_n$  and  $T = \frac{2\pi}{\sigma}$  is the period. The dispersion relation of these Poincaré waves looks like this:

$$\sigma_n^2 = f^2 + c_0^2 \left( k^2 + \frac{n^2 \pi^2}{B^2} \right). \quad 8)$$

With  $c_0 = \sqrt{gH}$  is the phase speed for gravity waves,  $k$  is the wavenumber in the  $x$ -direction (along channel direction),  $n=1,2,\dots$ , and  $B$  is the width of the basin. When  $B \rightarrow \infty$ , this dispersion relation reduces to the dispersion relation for Sverdrup waves, waves that occur in a domain unbounded by coasts. Hence, for the Arabian Gulf these waves are not of interest and these waves will be ignored henceforth. From equation 8) it can be easily seen that the minimum frequency of Poincaré waves is

$$\sigma_{Min} = \left( f^2 + c_0^2 \frac{\pi^2}{B^2} \right)^{\frac{1}{2}}. \quad 9)$$

For the Arabian Gulf, with an average width of 240 km, a depth of 36 m and an average latitude of  $27^\circ N$ , the maximum period for Poincaré waves is 6 hours and 54 minutes. This is at least a factor 2 less than the periods of the semi-diurnal and diurnal tides found to be dominant in the Arabian Gulf. This means that in this semi-infinite channel both Sverdrup and Poincaré waves are absent. Hence, the tidal waves are only present in the form of Kelvin waves. In a channel, the tidal wave consists of a Kelvin wave on each side of the channel, which decays exponentially towards the interior. The equations for the sea surface elevation and horizontal velocities for the total Kelvin wave are (see for example (Hendershott & Speranza, 1971))

$$\eta = \Re \left\{ Z e^{-\frac{y}{a}} e^{i(kx - \sigma t)} + Z e^{-\frac{B-y}{a}} e^{-i(kx + \sigma t)} \right\}, \quad 10)$$

$$u = \Re \left\{ \frac{Z}{H} c_0 e^{-\frac{y}{a}} e^{i(kx - \sigma t)} - \frac{Z}{H} c_0 e^{-\frac{B-y}{a}} e^{-i(kx + \sigma t)} \right\}, \quad 11)$$

$$v = 0. \quad 12)$$

Here  $a = c_0/f$  is the Rossby radius of deformation and  $\Re$  indicates the real part. These Kelvin waves have a dispersion relation of  $\sigma^2 = gHk^2$ . With this relationship the wavenumber of a wave with a given tidal period in a basin with a known depth can easily be computed.

Taking the real part of equation 10) and 10) the equations are reduced to

$$\eta = Ze^{-\frac{y}{a}}\cos(kx - \sigma t) + Ze^{-\frac{B-y}{a}}\cos(kx + \sigma t), \quad (13)$$

$$u = \frac{Z}{H}c_0e^{-\frac{y}{a}}\cos(kx - \sigma t) + \frac{Z}{H}c_0e^{-\frac{B-y}{a}}\cos(kx + \sigma t). \quad (14)$$

In the cross shore middle of the channel, i.e. when  $y = 0.5B$  equation 13) reduces to

$$\eta = 2Ze^{-\frac{1}{2}\frac{B}{a}}\cos(kx)\cos(\sigma t). \quad (15)$$

This equation clearly shows that the sea surface elevation reduces to zero for all times when  $x = (0.5 + n)\pi/k$ , with  $n=0,1,2,\dots$ . Hence, for a semi-infinite channel bounded by coasts on two sides, amphidromic points occur at the locations given by  $\left(\frac{(0.5+n)\pi}{k}, \frac{1}{2}B\right)$ .

In a similar way, equation 14) yields

$$u = \frac{2Z}{H}c_0e^{-\frac{1}{2}\frac{B}{a}}\sin(kx)\sin(\sigma t). \quad (16)$$

And the location of the x-velocity amphidromic point (or stagnation point) at  $\left(\frac{n\pi}{k}, \frac{1}{2}B\right)$ .

However, the Arabian Gulf is not a semi-infinite channel bounded by two coasts, but a semi-enclosed bay, with coasts on three sides. In this case an additional boundary condition exists, namely:

$$u = 0 \quad \text{at } x = 0. \quad (17)$$

Where  $x=0$  indicates the location of the closed boundary (where the incoming Kelvin wave is reflected) and  $x=L$  indicates the location of the open boundary (see Figure 2-4).

From equation (13) it follows that there exists no location  $x=\text{constant}$  that the amplitude of the sea surface equals zero for all values of  $y$ . At the coast therefore the solution of two superimposed Kelvin waves does not satisfy the boundary condition. The waves that do exist in this region close to  $x=0$  are so called trapped Poincaré waves. They have the following form (after (Hendershott & Speranza, 1971))

$$\eta_n = \Re \left\{ Z_n \left[ \cos\left(\frac{n\pi y}{B}\right) - \frac{iB}{n\pi} \frac{f s_n}{\sigma} \sin\left(\frac{n\pi y}{B}\right) \right] e^{-s_n x} e^{-i\sigma t} \right\}, \quad (18)$$

$$u_n = \Re \left\{ \frac{Z_n}{H} \frac{B}{\sigma n \pi} \left[ \frac{igHs_n n \pi}{B} \cos\left(\frac{n\pi y}{B}\right) - \sigma f \sin\left(\frac{n\pi y}{B}\right) \right] e^{-s_n x} e^{-i\sigma t} \right\}, \quad (19)$$

$$v_n = \Re \left\{ \frac{iZ_n}{H} \frac{B}{\sigma n \pi} \left( f^2 + \frac{gHn^2\pi^2}{B^2} \right) \sin\left(\frac{n\pi y}{B}\right) e^{-s_n x} e^{-i\sigma t} \right\}. \quad (20)$$

With  $n=1,2,\dots$ ,  $Z_n$  the (complex) amplitudes of each successive trapped Poincaré wave and  $s_n$  the (real) wavenumber of the trapped Poincaré waves. This wavenumber obeys the dispersion relation:

$$\sigma^2 = f^2 - gHs_n^2 + gH \frac{n^2\pi^2}{B^2}. \quad (21)$$

Hence, when one boundary of the channel is closed, the total solution is a combination of an incoming Kelvin wave, a reflected outgoing Kelvin wave and an infinite number of trapped Poincaré waves:

$$\eta = \Re \left\{ Z R e^{-\frac{y}{a}} e^{i(kx - \sigma t)} + Z e^{-\frac{B-y}{a}} e^{-i(kx + \sigma t)} + \eta_n \right\}, \quad 22)$$

$$u = \Re \left\{ \frac{Z}{H} c_0 \left( R e^{-\frac{y}{a}} e^{i(kx - \sigma t)} - e^{-\frac{B-y}{a}} e^{-i(kx + \sigma t)} \right) + u_n \right\}, \quad 23)$$

$$v = v_n. \quad 24)$$

In these equations a new (complex) reflection coefficient R has been introduced. This is because the properties of the outgoing Kelvin wave are affected by the presence of the trapped Poincaré waves. Now, since Z is arbitrary, these equations still have the unknowns R and  $Z_n$ . They can be found by using the boundary condition (equation 17)) and applying a so called collocation method. For details the reader is referred to Appendix B. When these equations are plotted the amphidromic points can easily be spotted. Figure 2-5 shows the co-phase lines (lines where high water occurs at the same time) and the co-range lines (lines where the tidal range is equal) from the original experiment performed by Taylor (1920).

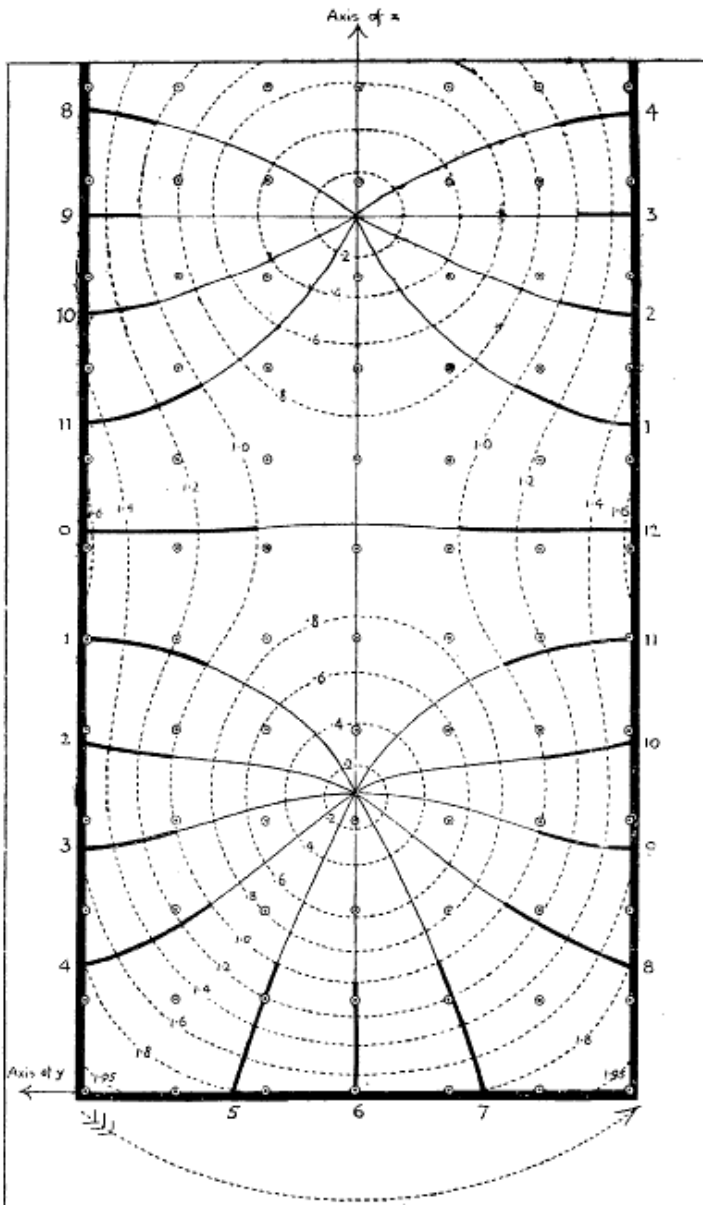


Figure 2-5 shows the co-phase lines (lines where high water occurs at the same time) and the co-range lines (lines where the tidal range is equal) from the original experiment performed by Taylor (1920).

The presence of Poincaré waves influences the location of the amphidromic points. For instance, a partially absorbing coast (a coast in which the incoming Kelvin wave loses energy when it hits the coast and is hence only partially reflected) can lead to a shift of the amphidromic points away from  $y = \frac{B}{2}$  (Hendershott & Speranza, 1971). Furthermore, the co-phase and co-tidal range lines can show very strange behavior when the tidal period is close to or smaller than the maximum period of Poincaré waves. This is because the energy of the incoming wave is now distributed not only over an outgoing Kelvin wave, but over several Poincaré waves as well (Hutter, et al., 2011).

In the case of the Arabian Gulf however these Poincaré waves are not excited and for this analytical solution a partially absorbing coast is not considered. Hence, at a distance far enough away from the west end coast (further than  $s_n$ ), the only waves present are the incoming and outgoing Kelvin waves. The only effect of

Figure 2-5: Co-range lines in basin where a Kelvin wave is being reflected. Full lines are co-phase lines. Figures outside the edge of the basin show time of high water on corresponding co-phase line. Dotted lines are co-range lines. Figures inside basin show amount of tidal range. The curved arrow shows direction of rotation of system. From Taylor (1920).

the trapped Poincaré waves that is present in this region is due to the reflection coefficient. As demonstrated below, this reflection coefficient causes a westward shift of the amphidromic points.

Because in this model the incoming Kelvin wave is fully reflected,  $|R| = 1$ , and  $R$  can be written as  $R = e^{i\phi}$ , where  $\phi = \arctan\left(\frac{\Im\{R\}}{\Re\{R\}}\right)$  is the argument of  $R$ . Inserting this into equation (22) and taking  $y=B/2$  this yields after rewriting:

$$\eta = \Re\left\{e^{-i\sigma t} e^{-\frac{1}{2a}B} e^{\frac{i\phi}{2}} \left(e^{i(kx+\frac{\phi}{2})} + e^{-i(kx+\frac{\phi}{2})}\right)\right\}. \quad (25)$$

Taking the real part yields

$$\eta = 2e^{-\frac{1}{2}B} \cos\left(\sigma t - \frac{\phi}{2}\right) \cos\left(kx + \frac{\phi}{2}\right), \quad (26)$$

and the amphidromic point locations at  $x = \frac{1}{k}\left(\pi(0.5 + n) - \frac{\phi}{2}\right)$ ,  $y = \frac{1}{2}B$ , with  $n=0,1,2,\dots$

Similarly, taking the real part of equation (23) yields after rewriting

$$u = \frac{2Z}{H} c_0 e^{-\frac{1}{2a}B} \sin\left(\sigma t - \frac{\phi}{2}\right) \sin\left(kx + \frac{\phi}{2}\right), \quad (27)$$

with the stagnation points at  $x = \frac{1}{k}(n\pi - \frac{\phi}{2})$ ,  $y = \frac{1}{2}B$ , with  $n=0,1,2,\dots$

This means that at locations where the influence of the trapped Poincaré waves themselves is negligible, their presence still leads to slight shift of the amphidromic points.

As mentioned earlier, the nonlinear terms in the shallow water equations make it impossible to solve these equations analytically. Therefore, these terms have been removed. However, these nonlinear terms are the cause an important physical phenomenon: overtides. In order to understand this better consider a wave of the type

$$A\sin(\sigma t). \quad (28)$$

The advection term  $u\partial u/\partial x$  can also be written as

$$\frac{1}{2}\frac{\partial u^2}{\partial x}. \quad (29)$$

Thus, the term  $u^2$  in equation 29) yields with simple trigonometry that

$$(A\sin(\sigma t))^2 = \frac{A^2}{2}(1 - \cos(2\sigma t)). \quad (30)$$

Thus, the advection term produces both a residual, steady component ( $A^2/2$ ) in equation 30) and constituent of frequency  $2\sigma$  (Prandle, 1991). A similar thing occurs through the interaction between  $u$  and  $\eta$ . In the case of nonlinear bottom friction, i.e., the last terms in equations 2) and 3) looks like this:

$$r'|u|u, \quad (31)$$

where the vertical brackets indicate the absolute value, to allow for negative values, and  $r'$  is, like  $r$ , a friction parameter that can be a function of velocity and or sea level or a constant, depending on the bottom friction schematization that is used. The absolute value prevents the usage of simple trigonometric relations as in equation 30), but it can be shown that (Cartwright, 1968)

$$A^2 \sin(\sigma t) |\sin(\sigma t)| = \frac{8}{3}\pi A^2 \left(\sin(\sigma t) - \frac{1}{5}\sin(3\sigma t) - \frac{1}{35}\sin(5\sigma t) \dots\right). \quad (32)$$

Hence, the advection term and the continuity equation produce even higher harmonics, while the bottom friction term produces odd higher harmonics. Thus, through a nonlinear term frequencies are produced that are a multiple of the original frequency. The tidal components that are created by the non-linear terms are called overtides or compound tides. Overtides are tides produced by a tidal component interacting with itself, while compound tides are tides produced by

the interactions of a tidal component with another. Some major examples are: the interaction of  $M_2$  with itself generates the  $M_4$  tide and the interaction of the  $M_2$  tide with the  $S_2$  tide generates the  $MS_4$  tide. In this way, many different tidal constituents are created that are not directly caused by astronomical forcing, but are simply generated by the tides themselves. There are more complicated ways to describe the generation of overtides, like for example with a perturbation method (see for example (Le Provost, 1991) or (Godin, 1991)).

## 2.3 Software

When simulating a body of water like the Arabian Gulf, the first step is generally to choose a software package suitable for solving the problems at hand. Then a grid is constructed and a model is set up. The first results of such a model often do not compare sufficiently to observations. Therefore, after the initial model setup, it is important to calibrate the model. This is generally done by changing the bathymetry of the model at certain locations until sufficient accuracy is reached. This method is specifically useful to change inaccuracies in the velocity field. Another option for calibration is changing the bottom friction or viscosity parameters in the model. For large scale models the viscosity does not have much effect, but the bottom friction has a significant influence on the amplitude of the water level. Before setting up a model and calibrating it however, it is important to have some knowledge of how the chosen software package operates. In this section the different kinds of software packages that are used in this study are described, in addition to some other similar software that is available. In the final section some considerations that are important when considering numerical models are presented.

### 2.3.1 Delft3D

Delft3D is software used to predict the flow in lakes, shallow seas, lagoons estuaries and other shallow water bodies and has been proven and validated numerous times (for example (Luijendijk, 2001), (Kuijper, et al., 2004)). It can describe flow characteristics like water level, velocity, salinity and temperature, depending on what the user requires. In addition to this, Delft3D can be used to model sediment transport, changes in bathymetry and more. Delft3D is composed of several different modules, of which is the Flow model is the cornerstone. Delft3D-Flow describes the flow patterns in bodies of water.

Delft3D-Flow solves the three dimensional nonlinear shallow water equations. This can either be done by solving the depth averaged two dimensional equations or the fully three dimensional equations; the user determines which method is used. The equations differ significantly from equations 1)-3) because they include more terms. The shallow water equations in Cartesian coordinates on the terrain following  $\sigma$ -plain as the vertical coordinate used by Delft3D, of which only the continuity equation is depth-averaged, read (Deltares, 2011):

$$\frac{\partial \eta}{\partial t} + \frac{1}{\sqrt{G_{xx}\sqrt{G_{yy}}}} \frac{\partial [(d+\eta)U\sqrt{G_{yy}}]}{\partial x} + \frac{1}{\sqrt{G_{xx}\sqrt{G_{yy}}}} \frac{\partial [(d+\eta)V\sqrt{G_{xx}}]}{\partial y} = Q, \quad 33)$$

$$\begin{aligned} \frac{\partial u}{\partial t} + \frac{u}{\sqrt{G_{xx}}} \frac{\partial u}{\partial x} + \frac{v}{\sqrt{G_{yy}}} \frac{\partial u}{\partial y} + \frac{w}{d+\eta} \frac{\partial u}{\partial \sigma} - \frac{v^2}{\sqrt{G_{xx}\sqrt{G_{yy}}}} \frac{\partial \sqrt{G_{yy}}}{\partial y} + \frac{uv}{\sqrt{G_{xx}\sqrt{G_{yy}}}} \frac{\partial \sqrt{G_{xx}}}{\partial x} - fv = \\ - \frac{1}{\rho_0 \sqrt{G_{xx}}} P_x + F_x + \frac{1}{(d+\eta)^2} \frac{\partial}{\partial \sigma} \left( \nu_V \frac{\partial u}{\partial \sigma} \right) + M_x, \end{aligned} \quad 34)$$

$$\begin{aligned} \frac{\partial v}{\partial t} + \frac{u}{\sqrt{G_{xx}}} \frac{\partial v}{\partial x} + \frac{v}{\sqrt{G_{yy}}} \frac{\partial v}{\partial y} + \frac{w}{d+\eta} \frac{\partial v}{\partial \sigma} + \frac{uv}{\sqrt{G_{xx}\sqrt{G_{yy}}}} \frac{\partial \sqrt{G_{yy}}}{\partial x} - \frac{u^2}{\sqrt{G_{xx}\sqrt{G_{yy}}}} \frac{\partial \sqrt{G_{xx}}}{\partial y} + fu = \\ - \frac{1}{\rho_0 \sqrt{G_{yy}}} P_y + F_y + \frac{1}{(d+\eta)^2} \frac{\partial}{\partial \sigma} \left( \nu_V \frac{\partial v}{\partial \sigma} \right) + M_y, \end{aligned} \quad 35)$$

with

$$Q = H \int_{-1}^0 q_{in} - q_{out} d\sigma + P - E. \quad (36)$$

In these equations Q represents the total influx and withdrawal of water through discharge ( $q_{in}$  and  $q_{out}$  respectively), evaporation (E) and precipitation (P),  $G_{xx}$  and  $G_{yy}$  represent conversion terms from spherical to Cartesian coordinates,  $d$  is the bottom depth,  $H = d + \eta$  is the total water depth,  $U$  and  $V$  are the depth averaged velocities in the  $x$  and  $y$  directions,  $w$  is the vertical velocity,  $P_x$  and  $P_y$  are hydrostatic pressure gradients in the  $x$  and  $y$  directions,  $F_x$  and  $F_y$  are radiation stress gradients in the  $x$  and  $y$  directions,  $\nu_v$  is the vertical eddy viscosity and  $M_x$  and  $M_y$  are sources of momentum in the  $x$  and  $y$  directions.

The vertical velocity ( $w$ ) is computed from the continuity equation:

$$\frac{\partial \eta}{\partial t} + \frac{1}{\sqrt{G_{xx}\sqrt{G_{yy}}}} \frac{\partial[(d+\eta)u\sqrt{G_{yy}}]}{\partial x} + \frac{1}{\sqrt{G_{xx}\sqrt{G_{yy}}}} \frac{\partial[(d+\eta)v\sqrt{G_{xx}}]}{\partial y} + \frac{\partial w}{\partial \sigma} = H(q_{in} - q_{out}). \quad (37)$$

Salinity, in addition to temperature, of course influences the density of the seawater through the equation of state and can hence induce flows that are induced by density differences. In Delft3D the equation of state is

$$\rho = \frac{1,000P_0}{\lambda + \alpha_0 P_0}, \quad (38)$$

where

$$\lambda = 1779.5 + 11.22t - 0.0745t^2 - (3.80 + 0.01t)s, \quad (39)$$

$$\alpha_0 = 0.6980, \quad (40)$$

$$P_0 = 5890 + 38 - 0.375t^2 + 3s. \quad (41)$$

In these equations  $t$  is the temperature in  $^{\circ}C$  and  $s$  the salinity in ppt (parts per thousand). The mass balance equation for salt is represented through the transport equation, which is valid for any dissolved substance or temperature through the following equation, where  $s$  can be replaced by the concentration of any dissolved substance or the temperature:

$$\frac{\partial(d+\eta)s}{\partial t} + \frac{1}{\sqrt{G_{xx}\sqrt{G_{yy}}}} \left( \frac{\partial[(d+\eta)us\sqrt{G_{yy}}]}{\partial x} + \frac{\partial[(d+\eta)vs\sqrt{G_{xx}}]}{\partial y} \right) + \frac{\partial ws}{\partial \sigma} = \frac{d+\eta}{\sqrt{G_{xx}\sqrt{G_{yy}}}} \left\{ \frac{\partial}{\partial x} \left( D_H \frac{\sqrt{G_{yy}}}{\sqrt{G_{xx}}} \frac{\partial s}{\partial x} \right) + \frac{\partial}{\partial y} \left( D_H \frac{\sqrt{G_{xx}}}{\sqrt{G_{yy}}} \frac{\partial s}{\partial y} \right) \right\} + \frac{1}{d+\eta} \frac{\partial}{\partial \sigma} \left( D_V \frac{\partial s}{\partial \sigma} \right) - \lambda_d (d + \eta)s + S. \quad (42)$$

With  $D_H$  the horizontal diffusion coefficient,  $D_V$  the vertical diffusion coefficient,  $\lambda_d$  representing the first order decay process and  $S$  the source and sink terms per unit area due to the discharge  $q_{in}$  or withdrawal  $q_{out}$  of water and/or the exchange of heat through the free surface  $Q_{tot}$ :

$$S = (d + \eta)(q_{in}s_{in} - q_{out}s) + Q_{tot}. \quad (43)$$

Note that in this thesis the temperature is kept constant throughout all experiments.

In the sigma coordinate system, the vertical velocity is relative to the sigma plane. The impermeability of the free surface ( $\sigma = 0$ ) and the bottom ( $\sigma = -1$ ) is taken as

$$w|_{\sigma=-1} = 0 \text{ and } w|_{\sigma=0} = 0. \quad (44)$$

Through all closed boundaries there is no transport of salt or water and in this thesis at the open boundaries only a vertical tide is imposed.

Many other effects on ocean flow are incorporated into these equations plus the other equations that have here been left out for the sake of brevity. A few of them are tides, bottom friction, winds, bathymetry and density differences. Delft3D solves the shallow-water equation on a so-called curvilinear Arakawa C-grid (a staggered grid). This type of grid computes the water level at the cell centers, but the velocity halfway between cell centers in their respective directions (Figure 2-6).

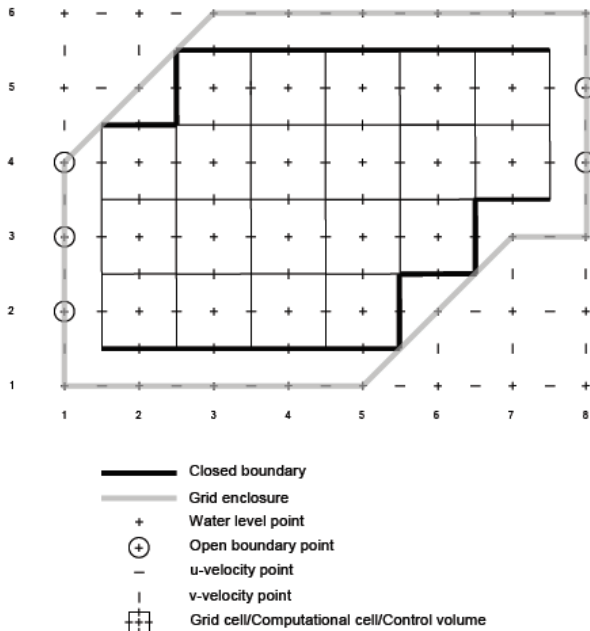


Figure 2-6: The Arakawa-C grid that is used by Delft3D. In this example square cells are displayed.

This curvilinear grid is rectangular in principle, but it allows for a slight stretching of grid cells, leading to grid cells that differ in size and shape from each other (see also Figure 1-3). For further details on the analytical and numerical aspects of Delft3D the reader is referred to the user manuals, i.e. (Deltares, 2011) and Delft3D describing literature, for example (Lesser, et al., 2004). Delft3D-Flow is linked to other different modules like a grid generator (RGFGRID) and a wave simulator. These modules combined lead to a very a large model which is capable of describing complicated processes in the oceans.

An important limitation however is the use of the curvilinear grid. This curving of cells provides for a grid that follows the coast better than a grid that uses square grid cells. However, there are of course limits to how much the cells can curve and vary in size. This means that the coast cannot be followed as perfectly

as one might hope. Especially in highly detailed models this is problematic. And in models that require both a low resolution area (like an offshore zone) and a high resolution area (like a harbor) a compromise needs to be made. For details about constraints and preferences with respect to building a grid with Delft3D and their differences with grid building in D-Flow FM the reader is referred to Appendix A.

### 2.3.2 D-Flow FM

D-Flow FM is the successor of Delft3D and is developed by the same company: Deltares. D-Flow FM is the core of Deltares' so-called 'Next generation hydro software project'. This project includes, besides the development of D-Flow FM, the adaptation of many previously developed software packages (for example in Delft3D) to D-Flow FM. The goal of this project is to develop new flow modeling software that works faster, is more accurate and is easier to work with (Deltares, sd).

The recent rise of the finite volume method and its success in other software packages has lead Deltares to incorporate this method into D-Flow FM. As is stated before, the major difference between D-Flow FM and Delft3D is the incorporation of this method. This is best visible through its unstructured grid: a grid that uses differently shaped grid cells in order to better follow coastlines and to allow for a local higher resolution without the need to build completely new models. For a more extensive discussion of the differences between the grid types the reader is referred to Appendix A. This project is still highly under development and for this thesis a beta version is used. In this version still many of the features that are present in Delft3D are missing, including water temperature and sediment transport.

Some of the features that are present in the used D-Flow FM version are bathymetry, wind, bottom friction and tides. In many ways, D-Flow FM is similar or even identical to Delft3D: it solves the same equations, uses similar theory and the methods of defining boundaries have the same roots. However, the change in grid is not the only difference. The numerical schemes used to solve the equations of motions have been updated for the curvilinear grids as well. These schemes essentially compute faster, but they lead to slight differences in model output as well. All in all, D-Flow FM as it is available for this thesis allows for basic flow modeling with rivers and tides but does not allow for more complicated flows induced by for example temperature.

Because of the relatively early stage of development most post-processing tools available for Delft3D are absent and even the ability to convert models from Delft3D to D-Flow FM has only recently been developed. Despite these early development stages, the 2D modeling functionalities have proven to have similar accuracy and computational costs as the current structured grid modeling programs Delft3D and WAQUA/TRIWAQ (Kernkamp, et al., 2011).

### ***2.3.3 Considerations regarding the differences between numerical and analytical models***

As stated in the previous sections, quite some assumptions are made in order to solve the equations of motions analytically. Numerical models are a lot less restricted, which allows the solving a much wider range of problems. However, numerical have their limits too, and care should be taken when applying them. Also, many processes, turbulence foremost among them, are not clearly understood yet and hence it is impossible to incorporate these processes into models without simplifications.

Turbulence for example takes place on scales varying from medium to very small. Depending on the resolution of the model, there is always a part of the turbulence that is neglected, and parameterizations need to be implemented. If the resolution is higher than the largest scales of turbulent eddies ( $\sim 1/4^\circ$ ), all turbulent effects are filtered out. The methods that are used to parameterize the effects of all turbulent processes below the scale of resolution can lead to approximations that neglect entire parts of the energy cycle (Dijkstra, 2012).

Other important considerations are the effects of numerical modeling itself. There are many different methods (so called 'schemes') to program the equations numerically, and none of these methods is perfect. Depending on which scheme is used, processes like 'numerical diffusion', 'numerical dispersion' and 'unphysical modes' can distort the solution (Røed, 2011). These processes are purely caused by the numerical scheme that is used and they have nothing to do with the actual result. Often the need to reduce these effects as much as possible poses constraints on time and/or space resolution. In Delft3D modules have been developed to visualize the so-called 'Courant-number', a parameter which is of high importance in determining the effects of the numerical distortions.

On the other hand, these numerical distortions can be utilized in order to improve the solution as well. For example, turbulent dissipation acts on such a wide range of scales that it cannot be resolved by general ocean models (Moin & Mahesh, 1998). Therefore, energy that disappears in natural situations cannot be removed in the model and large amounts of energy accumulate. Numerical diffusion can be utilized to remove this unnatural amount of energy from the system (Lesieur & Métais, 1996).

Of course, since most flow modeling software packages (including Delft3D and D-Flow FM) are highly complicated and try to simulate reality in the best way possible, they take into account

many additional processes than just those described in this study. One of the most important differences with respect to the analytical case, besides the presence of nonlinear terms, is the presence of friction. In Delft3D the bottom friction  $\tau_b$  for depth-averaged flow has the following form:

$$\tau_b = \frac{\rho_0 g U |U|}{C_{2D}^2}. \quad 45)$$

In this expression  $\rho_0$  is the constant reference density,  $U$  is the depth averaged velocity,  $|U|$  is the magnitude of the depth averaged velocity, and  $C_{2D}$  is a drag coefficient for which multiple formulations are possible. From this equation it is clear that in Delft3D friction is another source of nonlinearities and hence overtides. But the important thing about friction is that it evens out numerical instabilities that arise at the start of a model run (Deltares, 2011). This means that the friction term is used as a means to counter some of the problems that are caused purely by the numerical scheme. In numerical simulations it therefore remains an important term, even if this term is absent in the analytical solution.

## 2.4 Methods of analysis

Because there are good datasets available about the location of the amphidromic points of different tidal constituents, for example the Admiralty tide tables (Admiralty co-tidal Atlas Persian Gulf, 1999), and the analytical theory of these amphidromic points (section 2.2), this amphidromic point location has been used as the main method for comparing the differences between the different models in the experiments where the entire Arabian Gulf is reviewed. The basic principle of harmonic component analysis, which is used to isolate the different tidal components from each other, is described in section 2.4.1. Since even when only a single tidal component is regarded, the effects of the trapped Poincaré waves lead to a tidal range that is not truly zero, even though there is minimum tidal range. This effect is obviously stronger if the amphidromic point lies closer to the coast. For model comparison it can be useful to attach a numeric value to the location and value of the tidal range in that level. It is possible to do this by defining the amphidromic point as a point where the tidal range has a minimum. When the amphidromic point is computed point according to this definition, this point is referred to as a ‘range amphidromic point’. Determining the exact location of the amphidromic points with this method provides the possibility to compare the results between the different models in detail. The method to find the range amphidromic point is described in section 2.4.2.

All analysis methods were performed using Matlab versions 2012b and 2013a. This program’s inability to process unstructured data requires the use of time consuming interpolation functions, which greatly increases post-processing times for the unstructured grids. This slower post-processing should be taken into account when evaluating the models. However, Deltares is currently working on Matlab functions that avoid these interpolation functions so that post-processing should become considerably faster in the near future.

### 2.4.1 Harmonic component analysis

The water level in the oceans is always a superposition of many different tidal constituents. As mentioned before, in the Arabian Gulf the main constituents are the  $M_2$ ,  $S_2$ ,  $K_1$  and  $O_1$  tides. For the separation of the different tidal components a technique was used called ‘Harmonic analysis’; a technique that is described by (Chatfield, 1975). The basic concept is that every harmonic signal (like the sea level as a function of time) can be described by

$$X(t) = \alpha + \beta \cos(\sigma_1 t) + \gamma \sin(\sigma_1 t) + \delta \cos(\sigma_2 t) + \epsilon \sin(\sigma_2 t) + \dots, \quad (46)$$

in which  $X$  is the value of the signal at a certain time  $t$ ,  $\alpha$  is the mean level of the signal,  $\beta, \gamma, \delta, \epsilon, \dots$  are the amplitudes of the harmonic components with imposed frequencies  $\sigma_1, \sigma_2, \dots$

In order to solve for the amplitudes of the harmonic components, it is possible to expand equation (46) for multiple time steps and put it into matrix form:

$$X(t) = A(\sigma t) * B, \quad (47)$$

$$X(t) = \begin{pmatrix} X(1) \\ X(2) \\ \vdots \end{pmatrix}, B = \begin{pmatrix} \alpha \\ \beta \\ \gamma \end{pmatrix}, A(\sigma t) = \begin{pmatrix} 1 & \cos(\sigma_1) & \sin(\sigma_1) & \dots \\ 1 & \cos(2\sigma_1) & \sin(2\sigma_1) & \dots \\ \vdots & \vdots & \vdots & \ddots \end{pmatrix}. \quad (48)$$

In the matrix  $A$ , the length of the vertical dimension is equal to the length of  $X$ , and the length of the horizontal dimension is equal to two times the amount of frequencies specified plus 1. From this equation it is possible to find the vector  $B$ . The least square estimate of  $B$  which minimizes  $\sum_{t=1}^N (X_t - \alpha - \beta \cos(\sigma_1 t) - \gamma \sin(\sigma_1 t) - \delta \cos(\sigma_2 t) \dots)^2$  is found by matrix division. Using Matlab, this is a simple matter. A single component tidal wave can be written as  $\eta = R * \cos(\sigma t - \phi)$ , with  $R$  the amplitude of the wave and  $\phi$  the phase. Combining this with equation 46) yields:

$$X(t) = \alpha + \sum_{p=1}^P R_p \cos(\sigma_p t - \phi_p). \quad (49)$$

For this it was used that

$$\beta \cos(\sigma t) + \gamma \sin(\sigma t) = R * \cos(\sigma t - \phi), \quad (50)$$

with

$$R = \text{sgn}(\beta) \sqrt{\beta^2 + \gamma^2}, \phi = \text{atan}\left(-\frac{\gamma}{\beta}\right). \quad (51)$$

Using these equations it is possible to compute the amplitudes and phases of all tidal components (with given frequencies) that are relevant for this study.

Useful as this relatively simple analysis is, on longer timescales with many components this analysis no longer suffices. The reasons for this are for example celestial effects on the amplitude of the tidal components (Rijkswaterstaat, 2013). In time series analysis, these effects can be corrected for by using 'nodal correction', a method which modifies the amplitudes and phases of tidal components in order to correct for the celestial effects. For this reason, when considering the realistic model, use was made of the more sophisticated Matlab based harmonic analysis program

called `t_tide`. More information regarding this program can be found in (Pawlowicz, et al., 2002).

### 2.4.2 Amphidromic point

#### location

In order to determine the exact location of an amphidromic point and the tidal range in that point, consider Figure 2-7. This figure displays a typical tidal range as a function of the along channel distance. In this figure clearly 2 minima are visible.

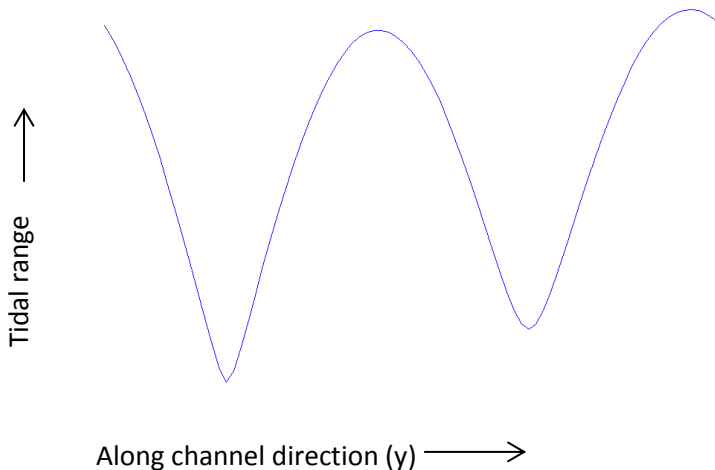


Figure 2-7: Typical shape of the tidal range

These minima indicate the along channel location of the amphidromic points, i.e., if this figure would have been given for  $y = 1/2B$  in the analytical solution, these minima would have been the amphidromic points. Close to the minima this curve seems to have a quadratic shape. Similarly, close to actual amphidromic point, the tidal range as a function of the cross channel distance approximately has a quadratic shape as well. Therefore, close to the amphidromic point, the tidal range may be approximated by

$$tidal\ range = a + bx + cx^2 + dxy + ey + fy^2, \quad 52)$$

where a...f are coefficients determined by the shape of the curve. These coefficients can subsequently be computed using Matlab's curve fitting toolbox. From these coefficients it is possible to, using the derivatives in the x and y direction of the quadratic equation, find the location of the minimum value of this curve. The minimum value of the tidal range can then be computed by inserting the found x and y values with the coefficients into equation 52).

## 2.5 Transport of salt applied to the Abu Dhabi region

In chapter 5 it is described how highly saline water coming from a desalination plant is transported through the coastal waters of Abu Dhabi. This section provides some mathematical details of mechanisms that are important for the transport of salt in the ocean. In addition, time scales are presented that can be used to determine how fast salt moves through a selected domain.

In section 2.2 it has been shown that in a rectangular basin with a flat bottom and no friction the tide is purely linear and no overtides or residual flow is generated. When friction, varying coasts or a varying bathymetry are used (as is the case in the realistic Arabian Gulf models), this is certainly not the case and nonlinear terms in the equations of motion lead to the generation of overtides and residual water motion. These nonlinear terms will also cause net transport of water (in particular because of a correlation between tidal velocity and sea surface height). If the bottom is irregular, tide-bathymetry interactions result in strong residual circulation cells and the joint action of tides and residual circulation cells cause efficient transport and mixing of dissolved substances like salt (Ridderinkhof & Zimmerman, 1992).

To quantify this, the residual velocity is defined as (definition from Ridderinkhof (1988)) is

$$\vec{u}_m = \langle \vec{u} \rangle = \frac{1}{T} \int_{-\frac{1}{2}T}^{\frac{1}{2}T} \vec{u}(t) dt. \quad (53)$$

In this equation an arrow indicates vector notation,  $\vec{u}$  consists of the two-dimensional velocity components, the  $\langle \rangle$  indicate tidally averaged,  $\vec{u}_m$  is the mean velocity,  $\vec{u}(t)$  is the velocity and  $T$  is one tidal period. In this thesis, because the dominant tide is the  $M_2$  tide, averaging is performed over a multiple of one tidal  $M_2$  period. The mean velocity is also called the 'residual' velocity. To determine how much water is transported, it is possible to take the water depth into account. In this case the mean transport ( $\vec{U}_m$ ) is defined as

$$\vec{U}_m = \langle \vec{u}(H + \eta) \rangle = \frac{1}{T} \int_{-\frac{1}{2}T}^{\frac{1}{2}T} \vec{u}(t)(H + \eta(t)) dt. \quad (54)$$

Equation 54) can be extended to include the salinity ( $s$ ). The result is an expression for the mean salt transport ( $\vec{T}$ ):

$$\vec{T} = \langle \vec{u}(H + \eta)s \rangle = \frac{1}{T} \int_{-\frac{1}{2}T}^{\frac{1}{2}T} \vec{u}(t)(H + \eta(t))s dt. \quad (55)$$

These definitions are a good starting point to predict how ocean water and salt are transported through the coastal waters of Abu Dhabi. In reality however this Eulerian approach is an approximation that is too simple for the net movement of water, and more so for the transport of dissolved substances in it (Zimmerman, 1978). This is especially the case when the coast and bathymetry are highly complex, such as the coastal waters around Abu Dhabi. In such complex areas the transport of dissolved substances is often chaotic, which results in some locations in which the dissolved substances are dispersed very quickly, while in other locations it is almost stagnant (Ridderinkhof & Zimmerman, 1992).

For an arbitrary time series the tidally averaged velocity equals zero. However, the tidally averaged water or salt transport is unequal to zero. This can be explained by applying Reynolds decomposition (where an arbitrary variable  $\xi$  is decomposed in a mean and a fluctuation, i.e.  $\xi = \langle \xi \rangle + \xi'$ , where the prime indicates a small fluctuation). By substituting the Reynolds

decomposed variables into the mean salt transport equation given by 55) the residual salt transport can be decomposed into a part consists of a product of the mean of the variables and a fluctuating part (see for example (Díez-Minguito, et al., 2013)):

$$\langle \vec{u}(H + \eta)s \rangle = \vec{T}_m + \vec{T}' \quad (56)$$

with

$$\vec{T}_m = \langle \vec{u} \rangle \langle H + \eta \rangle \langle s \rangle, \quad (57)$$

$$\vec{T}' = \langle s \rangle \langle \vec{u}'\eta' \rangle + \langle \vec{u} \rangle \langle s'\eta' \rangle + \langle H + \eta \rangle \langle \vec{u}'s' \rangle + \langle \vec{u}'s'\eta' \rangle. \quad (58)$$

Alternatively, in order to separate the salt transport from the water transport,  $\vec{T}'$  can be separated into

$$\vec{T}' = \langle \vec{U}_m \rangle \langle s \rangle + \vec{T}'', \quad (59)$$

$$\vec{T}'' = \langle \vec{u}'s' \rangle \langle H + \eta \rangle + \langle \eta's' \rangle \langle u \rangle + \langle \vec{u}'s'\eta' \rangle. \quad (60)$$

Thus, because the mean salt transport is the sum of a product of means and a fluctuation term, the mean salt (or water) transport is unequal to zero.

By using the first separation all fluctuation terms are separated from the mean, while using the second separation only the turbulent terms that include salt fluctuations are separated. Deviations from the mean are expected most where the residual flow has large spatial gradients. In Abu Dhabi, where the bathymetry and coasts vary greatly,  $\vec{T}'$  and  $\vec{T}''$  are expected to contribute significantly to the total salt transport.

Related to the definition of mean salt transport, it is possible to define several time scales that give an impression of how fast the salt moves through the waters of Abu Dhabi. Prandle (1984) identified several of them, and three are used in this study: the turnover time, the residence time and the flushing time. The turnover time is defined as the e-folding time-scale of replacement of material within a selected domain by material from outside the domain. The flushing time  $\tau_f$  is a measure for how fast a selected domain is refreshed by water flow through the selected domain. It is defined as the ratio between the total volume of water in a selected domain ( $V$ ) and the flow through the domain ( $q$ ):  $\tau_f = \frac{V}{q}$ , where  $q$  is defined as the total flux of water through a selected domain. In the case of a straight channel this is the velocity in the direction of the flow integrated over the area of a cross section of the channel. In mathematical form this is:  $q = \int \vec{u} \cdot \vec{n} \, dA$ , with  $n$  the vector normal to the cross section and  $A$  the area of the cross section.

The residence time ( $\tau_r$ ) gives the time required for a water parcel at an arbitrary location to leave a certain region. It is defined as the ratio between the total mass of the substance in a selected domain ( $M = Vc$ , with  $c$  the concentration of the substance, in this case the salinity  $s$ ) and the flux of the substance out of the region. Since in this study tides are important, it is important to use tidally averaged values. Hence, the definition for flushing time becomes  $\tau_f = \frac{\langle V \rangle}{\langle q \rangle}$ , and the definition for residence time becomes  $\tau_r = \frac{\langle M \rangle}{Y}$ , with  $Y = \int s * \vec{u} \cdot \vec{n} \, dA$  the value of the residual salt transport out of the region.

### 3. The Arabian Gulf as a rectangular basin

This chapter is based on a quote by Einstein “Make everything as simple as possible, but not simpler”. In order to get a first impression about the performances of Delft3D and FM, one of the simplest experiments possible was set up: the Arabian Gulf schematized as a rectangular basin with a single tidal constituent as the only forcing. This simple setup has the advantage that an analytical model can be used to compare the model results to. The theory of this analytical solution has been described in section 2.2. Section 3.1 describes the experiment setup that was used for this configuration. In section 3.2 the analytical solutions of the tides in a rectangular basin are described. Sections 3.3, 3.4 and 3.5 discuss the solutions using rectangular cells in Delft3D and D-Flow FM and triangular cells in D-Flow FM respectively. Section 3.6 summarizes the results of the sections prior to it and draws some conclusions.

#### 3.1 Setup of the experiment

The domain that was used has dimensions following the paper by Reynolds (1993), who presented accurate measurements of the Arabian Gulf. Recall from Figure 2-1 that the Arabian Gulf has an average length of 990 km, an average width of 240 km and an average depth of 36 m. Hence these will be the reference values used for the calculations in the coming subsections, both analytical and numerical. Since these experiments are meant to provide a basic understanding of the tidal patterns and understand the differences between analytic, Delft3D modeling and D-Flow FM modeling the only forcing applied is the tidal force. This forcing is applied through the wave shape described in the theory for the analytical model and in the form of a harmonic signal at the open boundary for the numerical models. The tides are composed of many different tidal constituents, caused by different celestial effects. Recall that in the Arabian Gulf the most important tidal constituents given in the charts by Admiralty are the semi-diurnal  $M_2$  and  $S_2$  tides, and the diurnal  $K_1$  and  $O_1$  tides (Admiralty co-tidal Atlas Persian Gulf, 1999). Of these, the  $M_2$  tide is by far the strongest. Therefore, despite the many other tidal constituents present in the Arabian Gulf, in this chapter the focus is on the  $M_2$  tide, with an occasional trip to one of the three other main tidal components. It is therefore this component that determines the forcing.

In this very simple first configuration, the analytical equations are the main foundation. Matlab2012b has been used to solve the trapped Poincaré waves and to later visualize the results. This has been done with a resolution of 10,000 km in both x and y-directions and a time step of 1 minute. However, the grid was shifted in such a way that a grid cell center occurred at the exact location of the analytically computed amphidromic point that was closest to the open boundary (for the location of this point see Table 3-1). The choice for the amphidromic point closest to the open boundary was made in order to have the least influence of trapped Poincaré waves possible and hence the location of the amphidromic point as close as possible to the location predicted by equation 26). This grid size and time step are also the values used by the numerical models, but for the models an additional experiment was performed using a grid size of 2.5 km. In all these experiments, both analytical and numerical models, an  $M_2$  tide with an amplitude of 1 meter for the sea surface was prescribed at the open boundary. Since this experiment tries to simulate the analytical solution, in the numerical model both the incoming wave and the outgoing wave receive this amplitude. In practice this will prove to be erroneous, because due to the friction the outgoing wave will have a decreased amplitude. In this thesis this is regarded in favor of attempt to not deviate from the analytical solution any further by lowering the outgoing wave even more.

Both Delft3D and D-Flow FM require boundary conditions at all open boundaries. In this study, as with the analytical solution, the superposition of two Kelvin waves is modeled, one incoming wave and one reflected outgoing wave. That is why the imposed boundary conditions consist of the values of these two separate waves at 7 points distributed equally along the boundary. Delft3D and D-Flow FM interpolate these values linearly between two points. The imposed phase difference between those two waves was computed by using equation (13). From this equation it can be derived that the phase difference between the incoming and the outgoing Kelvin waves is equal to  $2kL$ . Note that experiments performed by the author have shown that the phase difference is only marginally important, as the inclusion of the reflection coefficient, leading to a phase difference of  $2kL + \phi$ , only marginally affects the results interesting for this study.

As specified in section 2.3.3, the numerical models require a friction term. After several experiments it turns out that a Chézy type of bottom friction with a value of  $100 \text{ m}^{1/2}/\text{s}$  ( $=C_{2D}$  in equation (45)) for the Chézy friction coefficient combined with a viscosity of  $50 \text{ m}^2/\text{s}$  yields the best solutions based on tidal ranges and amphidromic point locations that are closest to those of the analytical solution. It should be noted however that the value of the viscosity has no effect on the results important for these experiments. The friction term could be set lower than the one chosen in order to approach the analytical solution as close as possible. However, the lower the friction is set, the longer it takes for numerical stabilities to filter out. For example, if the friction term is set 5 times as low, the water levels become numerically stable after more than 100 simulated days, against only 5 days for the chosen friction value. Besides this, friction is important in virtually all numerical models as well as in nature. These are the reasons that instead of trying to simulate the analytical solution as exact as possible, it was chosen to use a somewhat higher friction.

Amphidromic points can only be found per tidal component, and because in reality the sea level caused by the tides is a sum of many components, there is no location in which the tidal sea level is zero. In fact, due to friction even for single tidal components the sea level is non-zero at all locations. In the analytical solution the friction is ignored, and since only a single tidal component is simulated, this must yield amphidromic points with a zero water level. However, because of the generation of overtides by the numerical models, this zero water level amphidromic point ceases to exist even when using simple numerical models and only a minimum in the tidal range is visible. In these experiments, the  $M_2$  component can be assumed to be dominant enough to treat the total water level as found by the (both numeral and analytical) models as the water levels of the  $M_2$  tide. To obtain a measure for the influence of the higher order components, this assumption can be used to introduce a so called alpha line. Here, an 'alpha line' is defined as the line that indicates zero water levels across the domain at a single time step. An alpha line looks quite similar to the co-phase lines that Taylor used, and is in fact equal to a co-phase line for the analytical solution, but alpha lines can be used for sea levels that do not consist of a single component as well. In this way a measure is obtained for the deformation of the  $M_2$  amphidromic point by its higher order components. By defining the amphidromic point as the point where the alpha lines intersect, another indicator for differences between the different models is obtained. This 'amphidromic point' is henceforth named as 'alpha amphidromic point'. Of course, an alpha amphidromic point is no true amphidromic point, since it is derived from the total sea level, and not a single component, but in these experiments it is near enough to a true amphidromic point to give it that name. Since in numerical models alpha lines do not intersect at the same point, a mean and standard deviation of the amphidromic point can be found. This is a measure of the area in which the amphidromic point deviates to zero and if this

deformation is stronger in one direction. A more in depth treatment of these alpha amphidromic points and a comparison with range amphidromic points is given in Appendix C.

### 3.2 Analytical solutions of amphidromic points

**Table 3-1: The locations of the sea level and u amphidromic points for the analytical simulation of the Arabian Gulf, computed with different methods. The columns  $\phi = 0$  and  $\phi = 4.4^\circ$  show the analytical point locations with and without the effects of Poincaré waves respectively, in which  $\phi$  is the phase introduced by the reflection coefficient R, computed with equations (15), (16), (26) and (27). All values are in km, with the standard deviations of the alpha amphidromic point denoted between brackets.**

Type	Point 1					Point 2				
	$\phi = 0$	$\phi = 4.4^\circ$	Alpha point	Range point	M <sub>2</sub> range point	$\phi = 0$	$\phi = 4.4^\circ$	Alpha point	Range point	M <sub>2</sub> range point
$\eta$ x-location	210.0	204.9	206.1 (10 <sup>-14</sup> )	205.7	205.7	630.0	624.9	624.9 (10 <sup>-13</sup> )	624.9	624.7
$\eta$ y-location	120.0		120.0 (10 <sup>-14</sup> )	120.0	120.0	120.0		120.0 (10 <sup>-13</sup> )	120.0	120.0
$u$ x-location	420.0	414.9	414.8 (10 <sup>-14</sup> )	414.8	414.8	840.0	834.9	834.9 (10 <sup>-13</sup> )	834.9	834.9
$u$ y-location	120.0		120.0 (10 <sup>-14</sup> )	120.0	120.0	120.0		120.0 (10 <sup>-13</sup> )	120.0	120.0

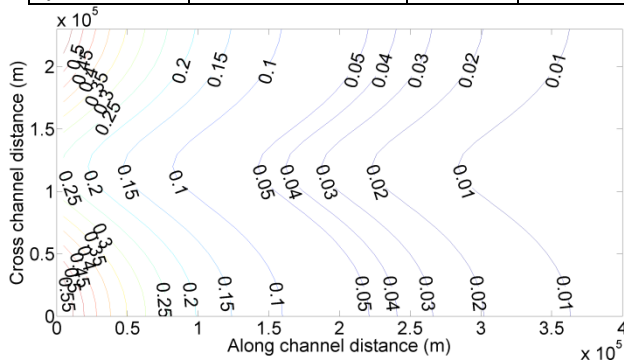


**Figure 3-1: The effects of trapped Poincaré waves in the west side of the basin, closest to the closed boundary. The lines display the tidal range caused by the trapped Poincaré waves only.**

In order to get a first impression of the accuracy of the alpha and range amphidromic points, Table 3-1 shows the location of the amphidromic points according to 5 computation methods. The first two columns are the values that have been derived analytically with the equations in section 2.2, without the effects of trapped Poincaré waves ( $\phi = 0$ ) and with the effects of trapped Poincaré waves through the reflection coefficient R ( $\phi = 4.4^\circ$ ), where the value 4.4 is derived using Arabian Gulf parameters. In the case of the alpha amphidromic points the order of magnitude of the standard deviations is noted between

brackets. By looking at the first sea level amphidromic point in this table, it can be seen that the alpha and range amphidromic points differ considerably from the locations derived by the equations in section 2.2. This difference is caused by the influence of the trapped Poincaré waves near the coast, which still have a range of approximately 3 cm at this location (see Figure 3-1). In the equations in the theory the direct effect of the Poincaré waves was not taken into account but only their effect through the reflection coefficient. This is the cause of this difference. A bit further into the basin, at the first velocity amphidromic (or stagnation) point, a slight difference occurs, but the velocity trapped Poincaré waves have an amplitude of only 5 mm at this location, which could make this shift either an inaccuracy in the computation methods or a small trapped Poincaré wave effect. The alpha amphidromic points in the right side of the basin matches almost exactly with the

analytical computations, which proves that the alpha amphidromic point method is a valid method to compute the location of the amphidromic point. The range amphidromic points differ somewhat more, which implies that this method is somewhat less accurate than the alpha amphidromic point method. It should be noted however, that when the grid is shifted in the y-direction, the interpolation errors cause an increase in the standard deviation to an order of magnitude of  $10^0$  when the amphidromic points lie on the edge of grid cells. This means that the numeric approximation does lead to some inaccuracies.

Similar to the results of Taylor's experiment in Figure 2-5, Figure 3-2 a-b shows the tidal range of the horizontal and vertical tide, together with the locations of the computed alpha amphidromic points (with standard deviations as error bars) and range amphidromic points. Note that since this is the analytical case, these alpha lines are equal to the co-phase lines. This is displayed in the same figure, as c-d shows the same as a-b, but this time only the isolated  $M_2$  component is displayed. It matches exactly with the total solution, which corresponds to the earlier statements. Note that the standard deviation is very small ( $\sim 10^{-10} m$ ) so that the error bars are hardly visible and that the alpha amphidromic location points and their standard deviations were computed using around 7000 intersections during 5 tidal periods.

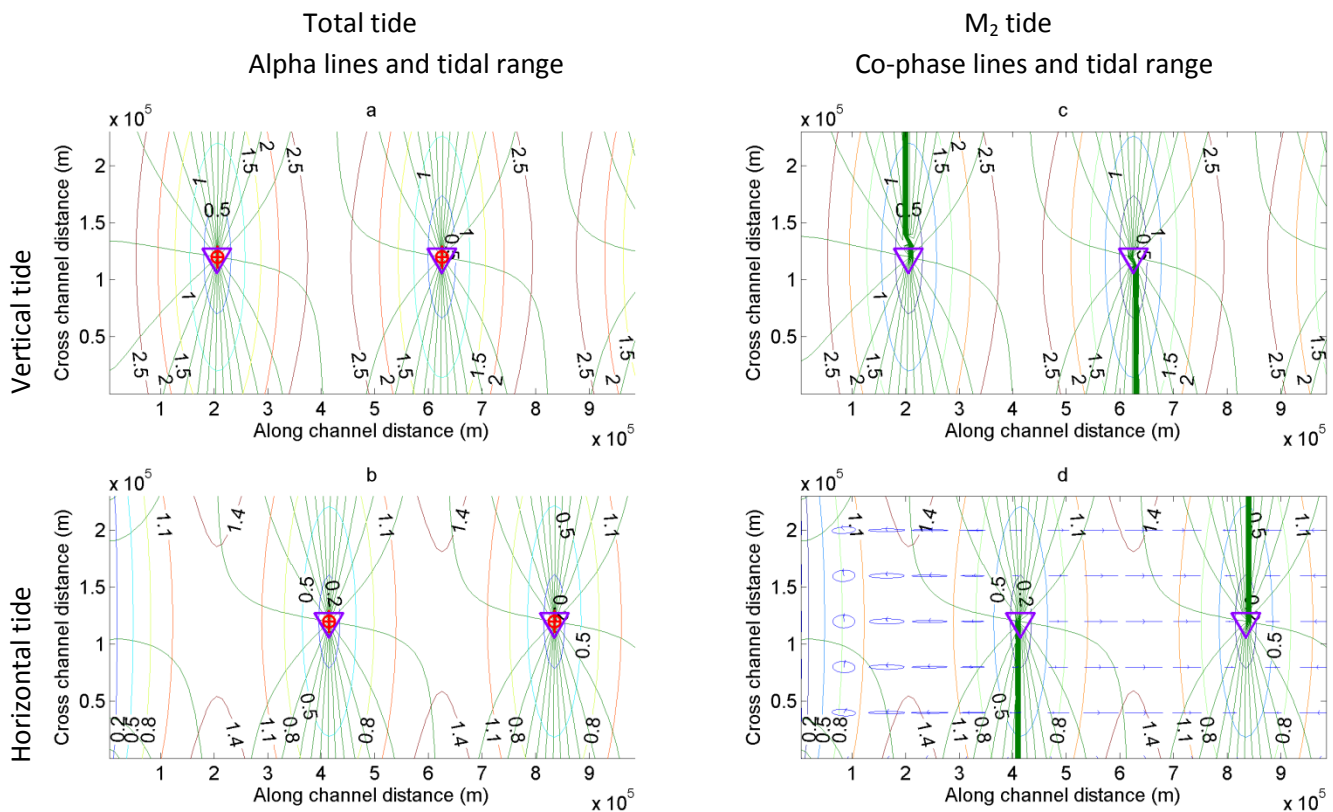


**Figure 3-2: Results of the analytical solution. (a) And (b) show the total vertical ( $\eta$ ) and horizontal ( $u$ ) tides respectively. The green lines are the alpha lines, with the distance between each line being  $1/12^{\text{th}}$  of a tidal period, while the colored lines with labels indicate the tidal range. The red circles with error bars of one standard deviation are the alpha amphidromic points, the violet triangles are range amphidromic points. (c) And (d) are similar to (a) and (b), but this time only the isolated  $M_2$  component is displayed. The green lines in these 2 figures indicate co-phase lines. The tidal ellipses in circles are displayed in figure (d), with the arrows indicating direction of rotation.**

### 3.3 Modeling the amphidromic points using square cells in Delft3D

Figure 3-3 shows the results of the model run by Delft3D. What strikes immediately is that the alpha lines no longer have a ‘point’ in which they converge, but a ‘spot’. This spot is clearly shown by the error bars that show the standard deviations, which are in the order of  $10^4$  m. Another striking feature is that the more to the right the amphidromic point lies, the further down it moves. This downward shift is caused by the friction. Recall that a Kelvin wave propagates on the north side

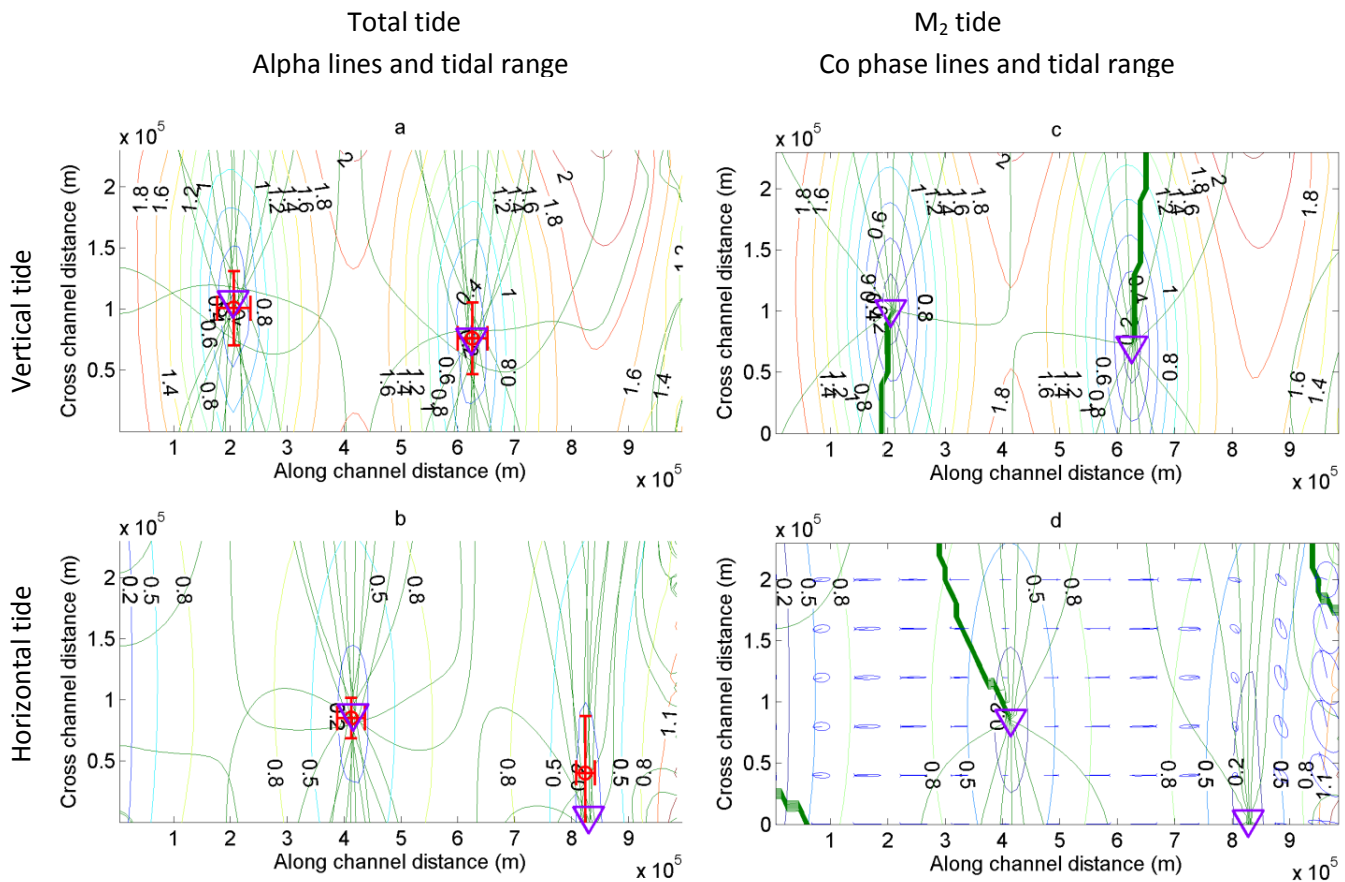


Figure 3-3: Similar to Figure 3-2, the results of the model run by Delft3D are displayed. Panel (a) and (b) show the total vertical ( $\eta$ ) and horizontal ( $u$ ) tides respectively. The green lines are the alpha lines, with the distance between each line being  $1/12^{\text{th}}$  of a tidal period, while the colored lines with labels indicate the tidal range. The red circles with error bars of one standard deviation are the alpha amphidromic points, the violet triangles are range amphidromic points. (c) and (d) are similar to (a) and (b), but this time only the isolated  $M_2$  component is displayed. The green lines in these 2 figures indicate co-phase lines. The tidal ellipses in circles are displayed in figure (d), with the arrows indicating direction of rotation.

of the basin to the left and via trapped Poincaré waves provides the energy for the eastward propagating outgoing Kelvin wave. Hence, friction lowers the outgoing Kelvin wave for a longer period of time, leading to Kelvin waves of unequal strength and a downward shift of the amphidromic points. This unequal strength of the Kelvin waves is also visible by the tidal ranges that are highest in the northeast and lowest in the southeast. This deviation of the amphidromic points away from the line  $y = 1/2B$  has been studied extensively using analytical models that extend the shallow water equations with extra terms. Starting with a relatively simple bottom friction term, in which the bottom friction coefficient is equal to a constant (Rienecker & Teubner, 1980); (Rizal, 2002), to the inclusion of viscous effects (Roos & Schuttelaars, 2009), these studies have all found this downward shift of amphidromic points away from the closed boundary. When studying the

actual amphidromic points of the  $M_2$  tide in the Arabian Gulf (see for example Figure 2-2), this downward shift of the amphidromic points away from the middle of the basin is actually present in the Arabian Gulf. In that respect the numerical models perform better than the analytical description that is described in this chapter. It shows that the incorporation of friction into the analytical model would have allowed for a better comparison between the numerical and analytical models.

The range amphidromic points now more clearly differ from the alpha amphidromic points than with the analytical solution, but this time they lie within less than a standard deviation. The  $M_2$  range amphidromic point locations are almost identical to the alpha and range amphidromic point locations of the total tide, showing that in the numerical model too, even though other tidal components are not negligible, in the total tide the  $M_2$  tide is clearly dominant. The standard deviation is only in Figure 3-3b more dominant in the x-direction. This, like the strange tidal ellipses seen in the right most part of Figure 3-3d are caused by Delft3D's numerical instabilities at the open boundary. The instabilities are generated by the fact that the prescribed outgoing Kelvin wave has a larger amplitude than the Kelvin wave that moves along the southern boundary towards the open boundary. This wave has a lower amplitude than prescribed because the friction has worked upon this wave. These instabilities could be reduced by lowering the amplitude of the prescribed outgoing wave at the open boundary.

Figure 3-4 shows that the  $M_4$  and  $M_6$  components are clearly present in Delft3D. What strikes in this figure is that the vertical  $M_4$  tide is strongest at the locations of the  $M_2$  amphidromic points. This however has nothing to do with the strength of the  $M_2$  tide, but only with the frequency of the  $M_4$  tide. This can be seen when calculating the locations of the  $M_4$  and  $M_6$  amphidromic points with equation 26), which yields locations for the amphidromic points that are very close to the locations seen in Figure 3-4. Despite the fact that the higher order components are generated in the entire basin, and are not just imposed like the  $M_2$  tide, these constituents do behave according to the theory described in the previous sections. The fact that the higher order constituents dominate over the  $M_2$  component at the  $M_2$  amphidromic points are the cause of the non-zero minima in the total

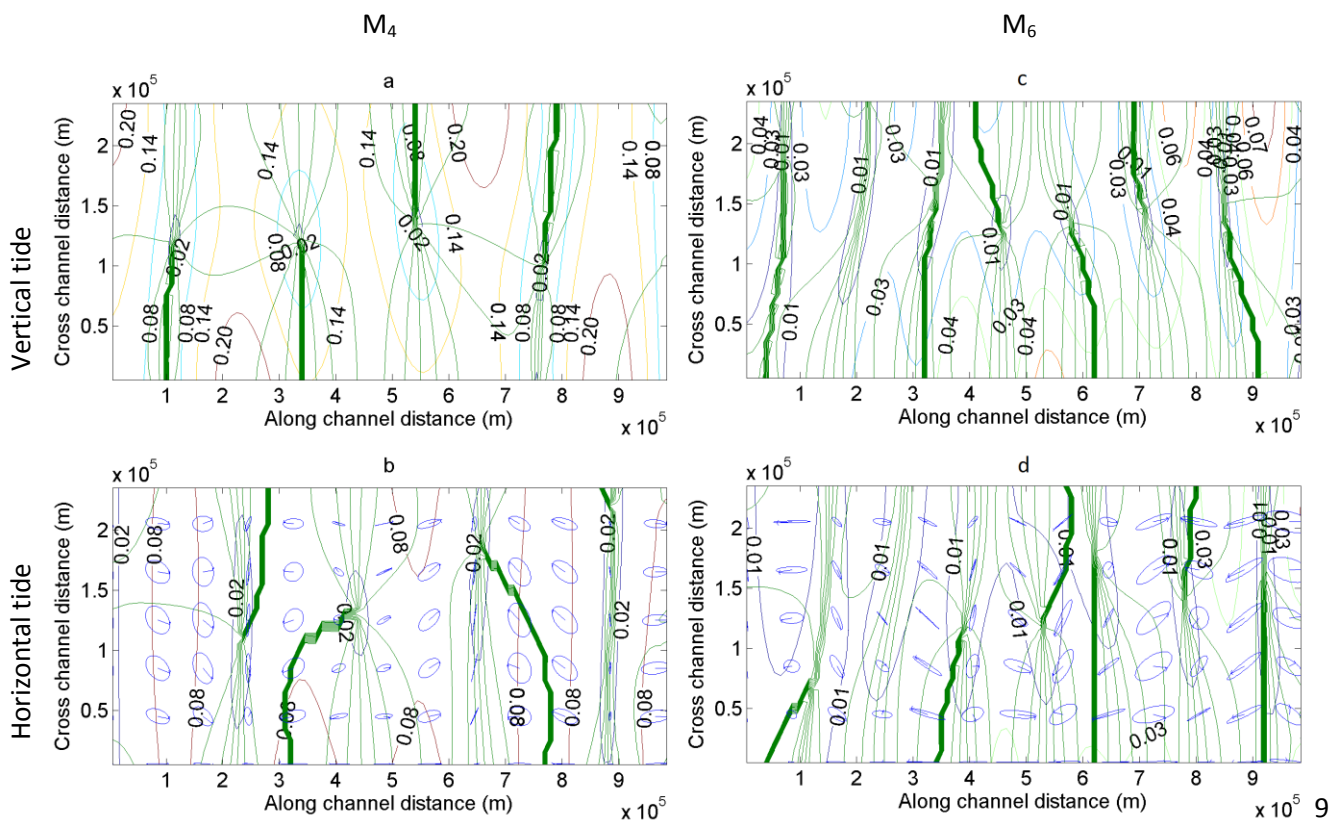


Figure 3-4: The  $M_4$  and  $M_6$  components isolated from the total tide of the Delft3D solution. The green lines are co-phase lines and the colored lines with labels are the co-range lines. (a) And (b) are the vertical and horizontal  $M_4$  tide respectively. (c) And (d) are the vertical and horizontal  $M_6$  tide respectively.

solution. When the tidal ranges of the  $M_2$ ,  $M_4$ ,  $M_6$ ,  $M_8$  and  $M_{10}$  constituents are added (and are corrected for their phases) the total tidal range (Figure 3-3a-b) is almost exactly reproduced (a local maximum of 3 mm difference, with a mean of order  $10^{-5}$  m). Since in the theory described in section 2.2, the  $M_2$  can only cause higher order M tides by itself, this means that Delft3D performs according to theory in this regard. However, the equilibrium sea level, of both the total solution and the one found by tidal component analysis, is consistently between 0.5 and 1 cm above zero in Delft3D. It is known that nonlinearities in the equations can lead to mean sea levels unequal to zero (see for example (Parker, 1991)), and this is probably the cause of nonzero sea level here.

### 3.4 Modeling the amphidromic points using square cells in D-Flow FM

Since D-Flow FM came with an updated numerical scheme for solving the equations of motion, it is likely that even an exact copy of a Delft3D model produces somewhat different results than Delft3D. Fortunately, these results are only small, since figures comparable to Figure 3-3 and Figure 3-4 are nearly identical. There are however differences, some of which are shown in Figure

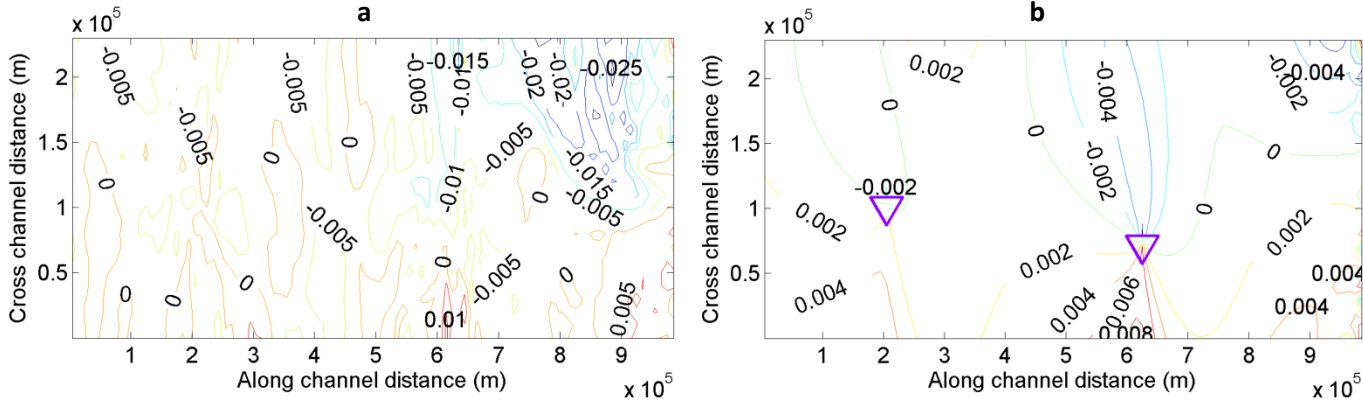


Figure 3-5: The difference between the Delft3D and D-Flow FM squares vertical tide. (a), The total vertical tide and (b), the vertical  $M_2$  component only. In Figure (b) the locations of the  $M_2$  range amphidromic points as produced by Delft3D are given (the purple triangles) as a reference.

3-5. These figures show that the absolute difference in the total solution varies between 0 and 2.6 cm, with a basin average of 4 mm, while the isolated  $M_2$  tide has differences that are much less, between 0 and 8 mm, with an average of 0 mm. When the grid size is 4 times as low, these values reduce considerably, with a mean difference of only 1 mm and a maximum of 7 mm for the total vertical tide. For the  $M_2$  these values change hardly, but the pattern around the amphidromic point in Figure 3-5b is now visible in the left amphidromic point as well. These differences are small, considering that the relative differences between sea level observations and models often are around a few percent. The pattern visible in Figure 3-5b, with negative values in the northern side of the basin and positive values in the southern side of the basin, suggests that the imbalance between the incoming and outgoing  $M_2$  Kelvin waves is stronger in D-Flow FM. This in turn would indicate a slightly greater friction term in D-Flow FM. However, with the values between these differences so low and the fact that a similar pattern is completely absent in Figure 3-5a makes this conclusion highly unlikely. The other components show differences between the models of a few millimeters which are substantially lower than those of the  $M_2$  tide at the original resolution. When the higher resolution is used, the model differences are approximately equal for all components. This means that model differences in the total solution can be explained by the model differences in the tidal

constituents for the higher resolution, but for the original resolution a part of these differences must be the results of differences in frequencies other than the M components.

As with the Delft3D solution, in D-Flow FM the mean sea level deviates from zero too, though approximately 3 mm less in the entire basin. The standard deviation of the alpha line intersections is on average 4 km lower than for the Delft3D solution. The velocities in the x-direction show no specific patterns like Figure 3-5b, but there does exist variation between the D-Flow FM and Delft3D square cell solutions. This variation is mostly present at the eastern and western boundary: in the interior the relative difference with respect to the Delft3D solution is less than 0.5% (corresponding to approximately 2 mm/s) when considering the total solution, but close to the boundaries the percentages go up to 10%. The same is true for the  $M_2$  only, where the difference between the models in the interior is less than 0.05%, but in this case close to the stagnation point the percentages rise to a maximum of 15%. The high percentages at the eastern boundary, like strange tidal ellipses at the eastern boundary displayed in Figure 3-3d, are caused by the numerical instabilities at the open boundary. For the higher resolution these values are similar, with the exception that no high values or percentages occur at the western boundary, but only at the (open) eastern boundary. The fact that the models perform similarly in the interior is a good result, but often the results close to the boundary are the most important results. One obvious example is the modeling of Abu Dhabi, where boundaries are present everywhere. A 15% difference in sea level or velocity between models at the boundary can lead to significantly high differences in the conclusions based upon these results. The numerical performance (computation time per grid cell per time step) of D-Flow FM with square cells in these experiments was significantly better than the numerical performance of Delft3D (see Table 3-2), for both the normal and the high resolution grid.

### 3.5 Modeling the amphidromic points using a mesh with triangular cells

Since in the grid with triangular cells, the results need to be interpolated to a regular, structured grid (in this case the grid that was used in the previous sections) for post-processing, this can cause inaccuracies that are not present in the results described in the previous sections. Despite that potential problem, as in the previous section, again the results are rather similar to the results of the Delft3D figures. However, the differences are much larger (Figure 3-6). For one, the absolute

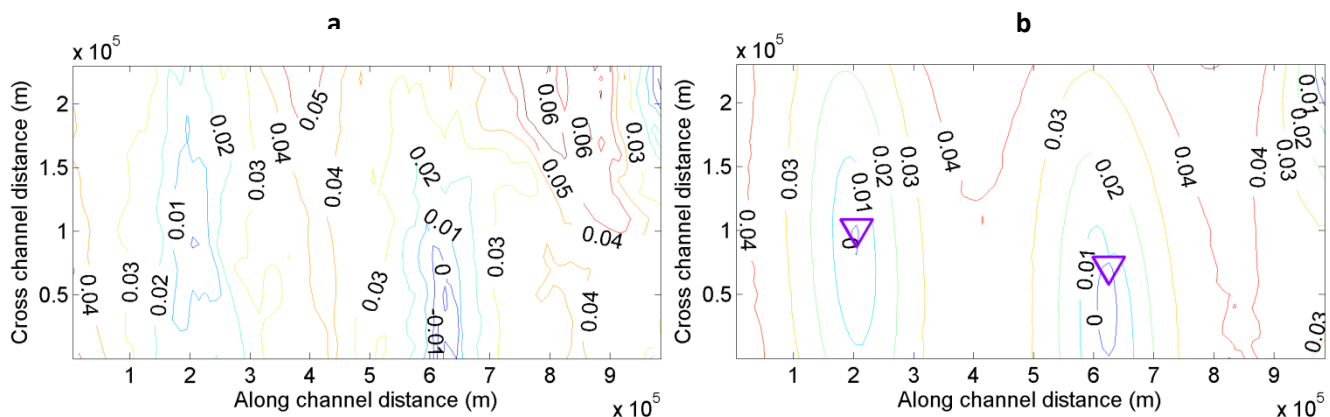


Figure 3-6: The difference between the square and triangular cells in the D-Flow FM solution of the vertical tide. (a), The total vertical tide and (b), the vertical  $M_2$  component only. In Figure (b) the locations of the  $M_2$  range amphidromic points as produced by the triangular grid are given (the purple triangles) as a reference.

differences in the total solution of the triangular grid are between 0 and 7 cm lower than the square

cells in D-Flow FM solution, with an average of 3 cm (for the higher resolution models these values are 4 cm and 8 mm respectively). The M<sub>2</sub> component is less, but still relatively large: between 0 and 4 cm, with an average of 3 cm (4 cm and 4 mm respectively for the high resolution). Considering that the relative difference in the total solution is up to 3% for the triangular grid, this is quite significant. As with the previous section, the other components show only slight differences between the rectangular and triangular grids.

When comparing Figure 3-6b to Figure 3-3c it can be seen that the M<sub>2</sub> component for the triangular grid cells is around 2% lower than the M<sub>2</sub> component for the square grid cells in the entire basin. Computed this percentage is 1.9% lower than the Delft3D solution, and 2.3% lower than the D-

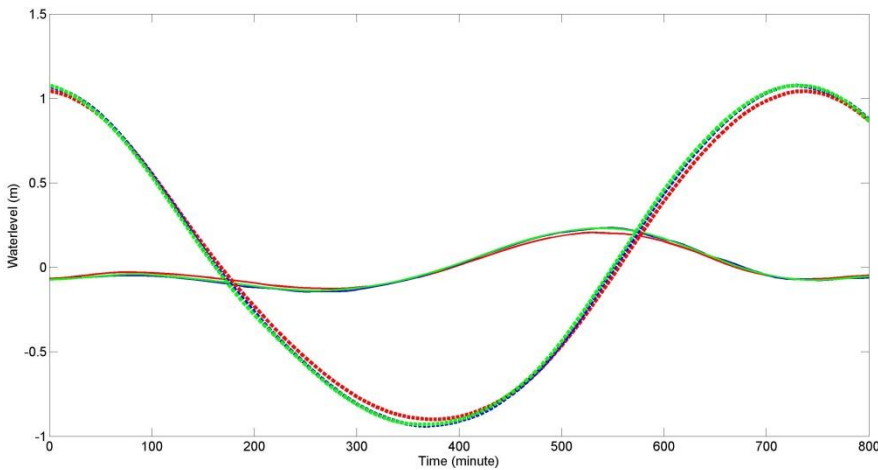


Figure 3-7: Time series for a point near an amphidromic point (dotted lines) and near the northern coast (solid lines) for the three numerical models. Green is Delft3D, blue is D-Flow FM square cells and red is D-Flow FM triangular cells.

flow FM square grid cell solution, with extremes going to 4.5% (both positive and negative). For the higher resolution grid this systematic difference disappears though, and only around the amphidromic points the percentages deviate from zero. The mean sea level is comparable to the mean sea level of the Delft3D results but the standard deviations of the alpha line intersections are approximately 10 km lower.

Figure 3-7 shows time

series of the sea level for two points, one close to an amphidromic point, and one close to the northern coast. This figure shows that Delft3D and D-Flow FM square cells match nearly completely, and that D-Flow FM triangular cells is slightly further away, but still the models match well. The slight deviation of D-Flow FM triangular cells might be explained by the fact that for Delft3D and D-Flow FM the observation point are exactly equal, but for D-Flow FM the observation point was shifted slightly away. This is due to the different grids with their different sea level computation points.

Table 3-2: The numerical performance in % of D-Flow FM with respect to Delft3D.

	Normal resolution	Resolution is 4 times higher
Delft3D	Reference	Reference
D-Flow FM square cells	21	10
D-Flow FM triangle cells	28	2

The differences of velocities in the x-direction between D-Flow FM triangular cells and square cells show more variation than between the two models with square cells. Close to the boundary the velocities in the x-direction have differences of up to 15 cm/s, while in the interior this is 'only' 5 cm/s, with a mean of 1.3 cm/s. For the high resolution models these values go down to 13 cm/s at the eastern boundary, with a basin mean of only 1 mm/s. In percentages averaged over the entire basin, triangular cells give velocities that are 1.9% lower than the Delft3D results, while they are 2.4% lower than the D-Flow FM square cell

result. The M<sub>2</sub> component has nearly identical values. These differences are acceptable, if not for the local differences of more than 80%, which are present in both the high resolution and original resolution grids. The numerical performance of triangular cells was even better than that of square cells in D-Flow FM, although this was less so for the high resolution grid (see Table 3-2).

### 3.6 Square cells versus triangular cells: some conclusions with regard to the simulation of a simplified analytical model

The goal of the experiments in this chapter was to get a first impression about how the tide behaves in the Arabian Gulf, and how much the analytical and numerical results overlap. The analytical model differed significantly from the numerical models. This difference, which has been induced by friction and nonlinear terms in the equations of motion, could have been lessened by incorporating friction into the analytical model (as in for example (Rizal, 2002) or (Roos & Schuttelaars, 2009)), or by regarding a tidal wave with a smaller amplitude. This last notion would have the effect that the nonlinear affects would have become smaller.

With respect to the differences between the numerical models, it has been shown that the differences between the sea levels for the three models were relatively small: only about 3%. The velocities in the x-direction differed considerably more, with differences of more than 80% locally. The numerical performance of D-Flow FM is significantly faster than Delft3D, for both square and triangular cells. Improving the resolution reduces the differences between the models, but the long post-processing time required for the unstructured grids partly negates this time improvement.

Despite the fact that the differences found are significant, they do not imply that one model is better than another, because at this point in this study it is impossible to make any conclusions about that. The reason for this is that the models described in this chapter can only show approximate results, like the amount of amphidromic points per component or their approximate location. When comparing these results with Admiralty tidal charts (Admiralty co-tidal Atlas Persian Gulf, 1999), they match to a large extent, the numerical models more so than the analytical model. This is only to be expected after the assumption made to set up the analytical model. After all, Delft3D and D-Flow FM are software packages that have been created to simulate realistic situations. The theoretical concepts described earlier differ too much from realistic situation that an exact duplication of the analytical results by Delft3D or D-Flow FM cannot be expected.

#### 4. The Arabian Gulf using realistic geometry

The goal of this chapter is to develop a model that is suited to serve as a large scale model in which a detailed Abu Dhabi model can be nested. Such a model needs to be able to reproduce the tidal components throughout the Gulf and near the Abu Dhabi area in particular. Such a model exists already in Delft3D and is has been developed by Alkyon, now part of ARCADIS (Alkyon, 2004). The original goal of this model was to provide an overall Arabian Gulf water motion model that could be used to provide boundary conditions for smaller, nested models in the Arabian Gulf. This model differs from the numerical models in the previous section in the sense that more tidal components are prescribed at the boundary and that a realistic coastal boundary and bathymetry is used. The usage of realistic geometry and bathymetry unfortunately does not allow for analytical solutions but it does provide for a better opportunity to investigate the tidal motion in the Arabian Gulf and to test the model performances against observations.

However, since the ultimate of building a realistic large scale Arabian Gulf model is to be able to nest a detailed Abu Dhabi model in it, it is necessary that a D-Flow FM model is developed and compared to both the Delft3D model (as a reference) and to observations. Therefore, in this chapter two D-Flow FM model are shown, one which has a curvilinear grid and is essentially the same as the Delft3D model, and one model which uses a grid with triangular cells. The three models are compared to each other and to observations. Since the observations (Admiralty tide tables , 2002) include only amplitudes and phases of the four major tidal constituents ( $M_2$ ,  $S_2$ ,  $K_1$  and  $O_1$ ), the amplitudes and phases of these values are the only indicators of model accuracy.

The experiment setup, including grid and boundary conditions is given in section 4.1. The results of simulating the tides in the Arabian Gulf using a realistic geometry and bathymetry and the comparison of the three different numerical models is given in section 4.2.

##### 4.1 Setup of the experiment

The model built by ARCADIS starts in the Gulf of Oman at approximately the line Sur (in Oman) to Chah Bahar (in Iran) and includes the entire Arabian Gulf (see Figure 4-1). The equations solved are equal to the equations described and solved in the previous sections: the depth averaged shallow water equations. The model was designed in order to simulate tidal propagation in the Arabian Gulf as accurate as possible so that it can be used as boundary input for smaller models in

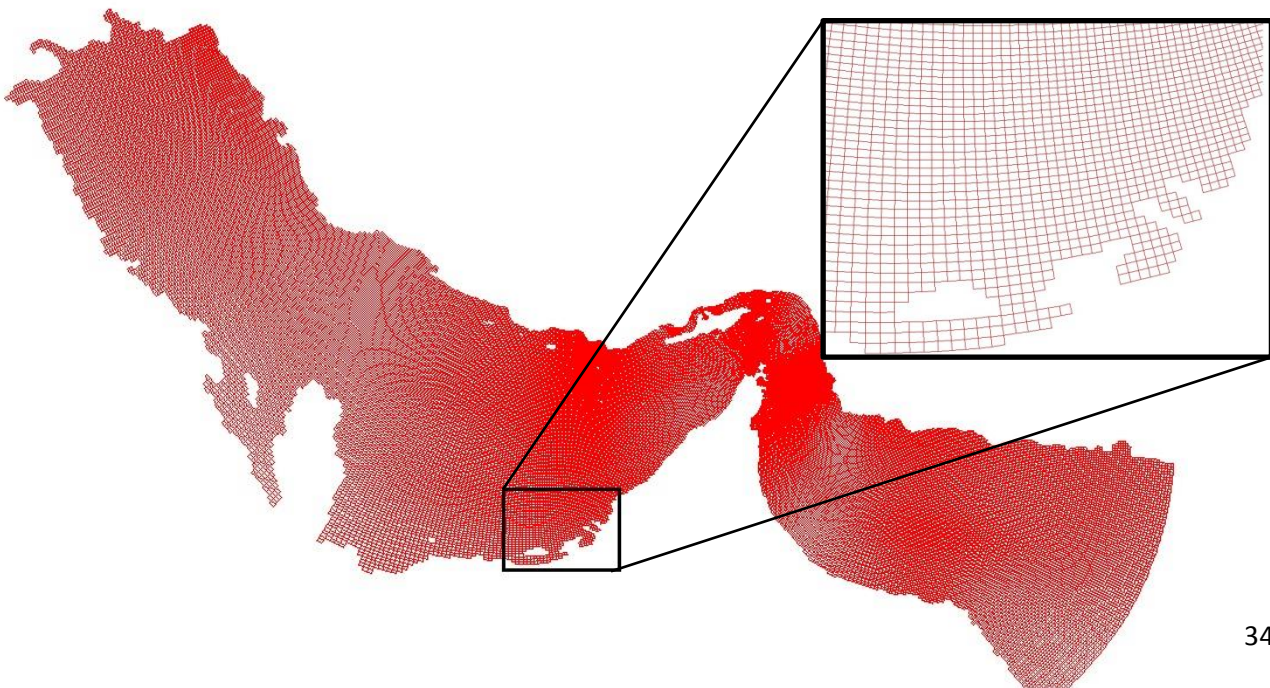


Figure 4-1: The grid of the model built by ARCADIS displayed in D-Flow FM with the Abu Dhabi area magnified. This grid is identical to the grid used by the curvilinear D-Flow FM model.

the region. ARCADIS has used the model for this purpose for multiple projects and the model has proved to be functioning well. For some of these projects a Gulf wide wind driven water motion was used as well.

The model was built using a spherical grid to allow for a varying Coriolis parameter and it has a resolution varying between 0.5 and 2.5 geographical minutes. At a latitude of 30° N this corresponds with a resolution between 800 and 4000 meter. For the bathymetry of the model the ETOPO2 global 2 minutes (NOAA, 2001) database was compared with Admiralty charts to infer the most accurate data. These data are however not as accurate as one could want, and this allows for some room to adjust the bathymetry for model calibration. It should be noted that the grid resolution and bathymetry data are accurate enough for the simulation of the entire Arabian Gulf, but for more detailed models it is important to get more accurate bathymetry data and to use a higher resolution.

The tidal boundary conditions in this model are derived from TOPEX/POSEIDON satellite altimeter data (Matsumoto, et al., 2000). Included in this model are the main 16 short-period tidal constituents (M<sub>2</sub>, S<sub>2</sub>, K<sub>1</sub>, O<sub>1</sub>, N<sub>2</sub>, P<sub>1</sub>, K<sub>2</sub>, Q<sub>1</sub>, M<sub>1</sub>, J<sub>1</sub>, OO<sub>1</sub>, 2N<sub>2</sub>, Mu<sub>2</sub>, Nu<sub>2</sub>, L<sub>2</sub> and T<sub>2</sub>) and 7 long-period constituents (M<sub>tm</sub>, M<sub>f</sub>, M<sub>Sf</sub>, M<sub>m</sub>, M<sub>Sm</sub>, S<sub>Sa</sub> and S<sub>a</sub>). All these components are given at several different points along the boundary; this means that variation of the tidal constituents along the boundary was included. The model was calibrated using observational data of the four main constituents (Admiralty tide tables, 2002). The more than 140 observations that are used for this calibration are spread mostly along all coasts of the Arabian Gulf, but a few of them are on islands in the Gulf's interior. The observations only consist of the amplitudes and phases of the M<sub>2</sub>, S<sub>2</sub>, K<sub>1</sub> and O<sub>1</sub> tidal components. For further details about this model the reader is referred to the original report about the creation of this model (Alkyon, 2004). All the model characteristics described above are also applied to the two D-Flow FM grids, with the exception of the grid.

For the development of the curvilinear model in D-Flow FM, the Delft3D model was replicated exactly to a D-Flow FM model. Therefore, the grid of the D-Flow FM curvilinear model is identical to the Delft3D grid. Based upon this original model that has now been converted for use by D-Flow FM, an unstructured grid model has been developed which uses the advantageous grid properties of D-Flow FM (Figure 4-2). In this grid the boundaries of the original grid were taken and the

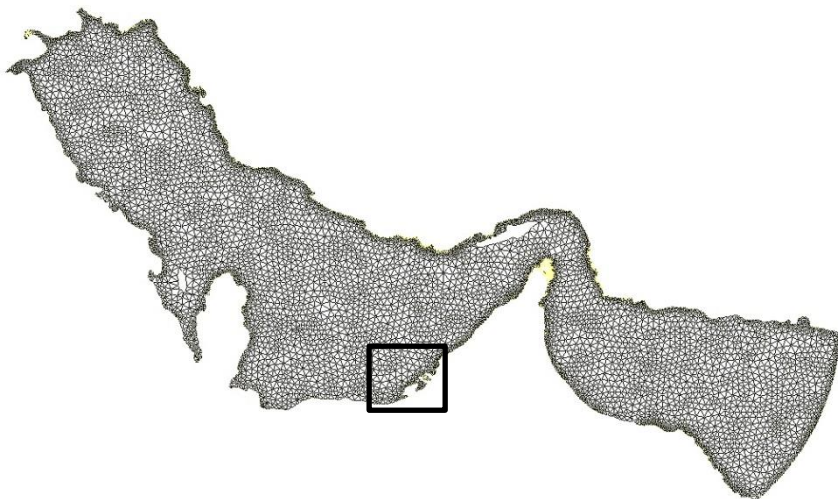


Figure 4-2: The grid with triangular cells. The black square is the area which is refined for the next section (Figure 5-1).

curvilinear cells replaced by triangular cells, but with a decreasing resolution towards the interior of the grid. The reason for this is that in the interior of the Arabian Gulf the nonlinear flow producing coasts and bottom are much farther away than at the coasts, and hence the flow changes on a much larger time and space scale than close to the boundaries. This means that in the interior of the Gulf a lower resolution is allowed. Another D-Flow FM feature applied to this grid is the projection of the

grid boundary to the land boundary, which results in a grid that follows the land boundary more closely than the curvilinear grids. For more images and technical details about the two grids the reader is referred to Appendix D.

#### 4.2 Numerical simulation of the Arabian Gulf

Figure 4-3 displays the amplitudes and phases of the M<sub>2</sub> tide compared to observations. For clarity, in this figure the locations of the range amphidromic points are given by purple triangles and the value of the M<sub>2</sub> amplitude in this point in yellow. This figure shows that the model compares well to observations; something that is illustrated in Table 4-1 as well. The figure shows that the amphidromic points do not occur on the middle of the basin, which was already shown by the results of the numerical model in the previous chapter as well. In that chapter it was caused by the application of friction, but studies have shown that a varying bathymetry, via bottom friction (larger depth means larger distance from the bottom and hence a lower bottom friction at the sea surface),

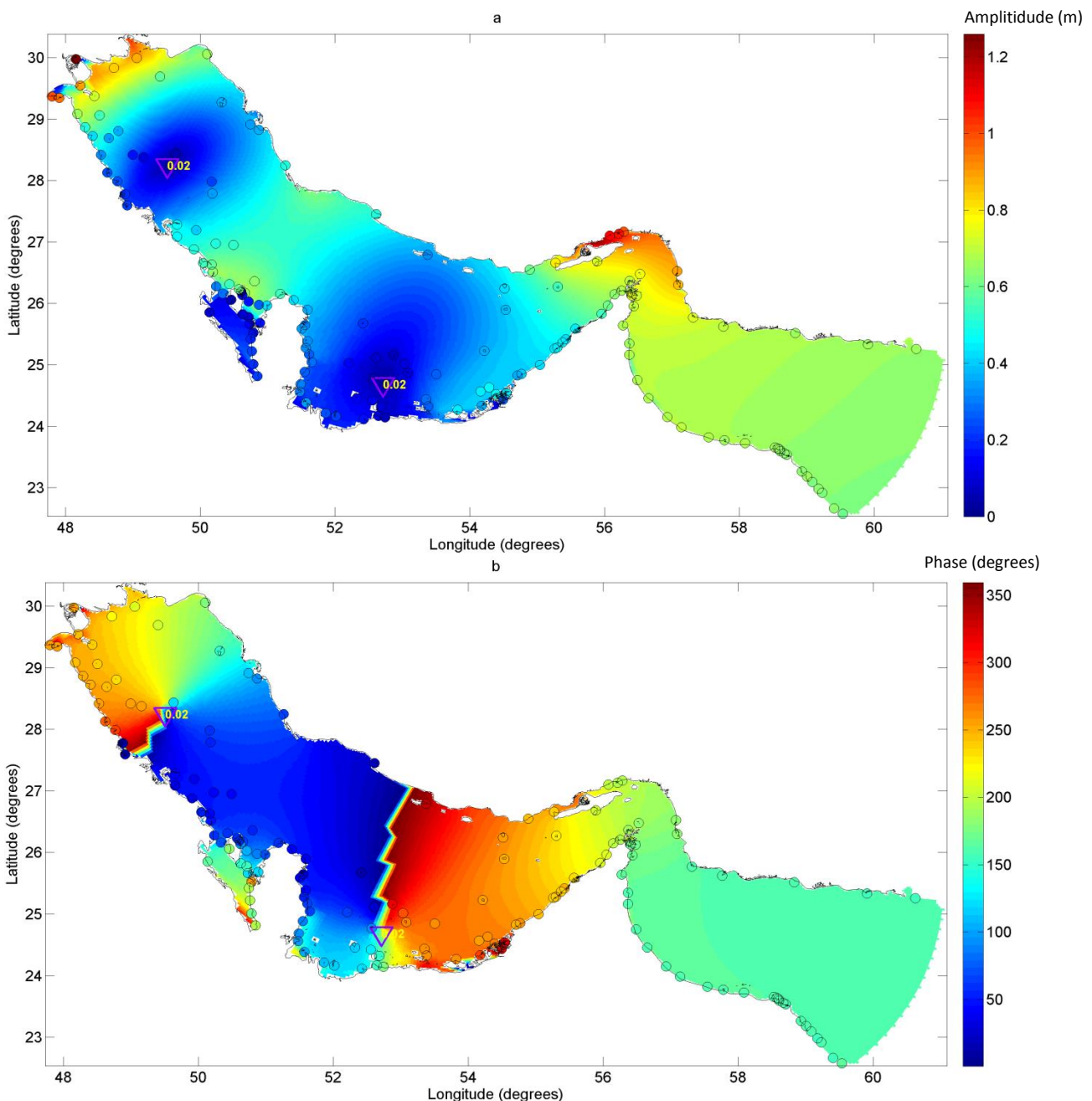


Figure 4-3: The tidal amplitude (a) and phase (b) of the M<sub>2</sub> tide as produced by ARCADIS' model. The purple triangles with yellow labels are the range amphidromic points with the amplitude of the M<sub>2</sub> tide in those points. The interior of the little circles displays the amplitudes and phases of the M<sub>2</sub> tide as given from observations by the Admiralty tide tables (2002) in the same color scale.

has a significant effect on the location of the amphidromic points (Davies & Jones, 1995). It is likely that the varying coast and Coriolis force have an effect as well. Images similar to Figure 4-3, that display the amplitudes and phases of the other 3 major tidal components, as well as the amplitudes and phases computed from observation from Admiralty co-tidal Atlas Persian Gulf (1999), are given in Appendix E. By subtracting the observational values of the amplitudes and phases from the

**Table 4-1: The means and standard deviations of the difference between the models and the observations for the different models for several components are displayed for all observation points with the values for the 9 observations near Abu Dhabi between brackets. The model that performs best across all observations is highlighted in green.**

M2	Delft3D	D-Flow FM curvilinear	D-Flow FM triangle
Mean Amplitude	0.018 (-0.019)	0.011 (0.001)	0.003 (-0.09)
Standard deviation Amplitude	0.146 (0.09)	0.135 (0.056)	0.166 (0.173)
Mean Phase	8.66 (4.469)	9.838 (0.665)	12.672 (36.254)
Standard deviation Phase	20.342 (7.642)	21.095 (17.725)	30.562 (47.199)
S2			
Mean Amplitude	0.015 (0.016)	0.013 (0.023)	0.011 (-0.015)
Standard deviation	0.053 (0.033)	0.05 (0.032)	0.06 (0.059)
Mean Phase	0.312 (-0.276)	1.861 (-5.288)	4.555 (32.652)
Standard deviation Phase	25.235 (28.683)	25.048 (14.332)	36.408 (57.817)
K1			
Mean Amplitude	-0.021 (-0.015)	-0.029 (-0.026)	-0.044 (-0.105)
Standard deviation Amplitude	0.06 (0.044)	0.061 (0.051)	0.094 (0.085)
Mean Phase	2.102 (3.329)	3.178 (-0.555)	6.004 (29.407)
Standard deviation Phase	17.339 (10.794)	17.843 (22.256)	27.933 (40.13)
O1			
Mean Amplitude	-0.007 (-0.003)	-0.012 (-0.008)	-0.026 (-0.061)
Standard deviation	0.032 (0.041)	0.03 (0.034)	0.047 (0.075)
Mean Phase	6.368 (4.499)	8.485 (1.817)	14.689 (44.712)
Standard deviation Phase	17.277 (18.951)	17.897 (24.962)	28.669 (48.941)

**Table 4-2: The mean difference of the amplitude of the 4 major components of the two D-Flow FM models with respect to the Delft3D solution in %.**

	Square cells	Triangular cells
M <sub>2</sub>	0.73	-0.97
S <sub>2</sub>	0.62	-0.68
K <sub>1</sub>	2.8	4.15
O <sub>1</sub>	2.5	6.56

amplitudes and phases produced by the numerical models in each station, and subsequently taking the mean and standard deviation, Table 4-1 is produced. This table shows that in general the model results compare well with observations, with differences of up to 2 cm for the Delft3D results. It also shows that the two curvilinear grids perform almost identically, with Delft3D only marginally better. The standard deviations are substantial, with standard deviations that are between ten and twenty percent their respective maximum tidal amplitudes in the Gulf. With respect to amplitudes, only the K1 tide is striking, since for this tidal component D-Flow FM shows a difference between amplitude

and observations of more than 4 cm. This is almost 10% of the maximum amplitude of the K1 tide in the Arabian Gulf. This is substantially more than for the other components and is undesirable. The standard deviations of the grid with triangular cells are consistently approximately 10 degrees larger than those of the other grids; this means that error margin is larger than for the other grids. Close to Abu Dhabi, where 9 of the 148 observation points lie, the grid with triangular cells performs considerably worse. A reason for this could be that the model that was used has not been calibrated to produce the most accurate results, and calibration, as well as increasing the resolution, of this model has the potential to

substantially improve the results when using this grid. Another possible explanation for the larger differences for the grid with triangular cells is that because of the higher resolution, observation points can lie up to 5 km away from the sea level computation points.

The differences between observations do not have the same mean and standard deviation throughout the basin, but differ regionally. This is illustrated by Figure 4-4, which shows the M2 amplitudes in all observation stations that were used during this study. From this figure it can be seen that all models compare better to observations for stations 100-150 than for stations 0-100. Since similar plots for the other 3 major components as well as well as similar plots for the phases show this pattern as well, this suggests that in the western half of the Arabian Gulf, where stations 0-100 lie, the models have been insufficiently calibrated. Since these models work with a uniform bottom friction parameter, these models could be improved by adjusting the bathymetry somewhat

in the western part of the Arabian Gulf. Especially the D-Flow FM model that uses a grid with triangular cells, which has not been calibrated, shows some large differences from observations. Therefore, if this grid is used for future projects it is recommended to improve the model results some more by adjusting the local bathymetry.

Table 4-2 shows differences of the amplitudes of the major tidal constituents between the three models. This table shows that the semi-diurnal constituents are modeled comparably by all three models. This is similar to the results in the previous chapter. The diurnal constituents differ somewhat more with means going up to 6.5% for the O1 component of the grid with triangular cells. For all components and both models there are local differences that go up as far as 80%. These high percentages arise at the amphidromic points and near coasts. This difference is remarkable, but in the end the most important thing is how close the model results are to observations. All grids

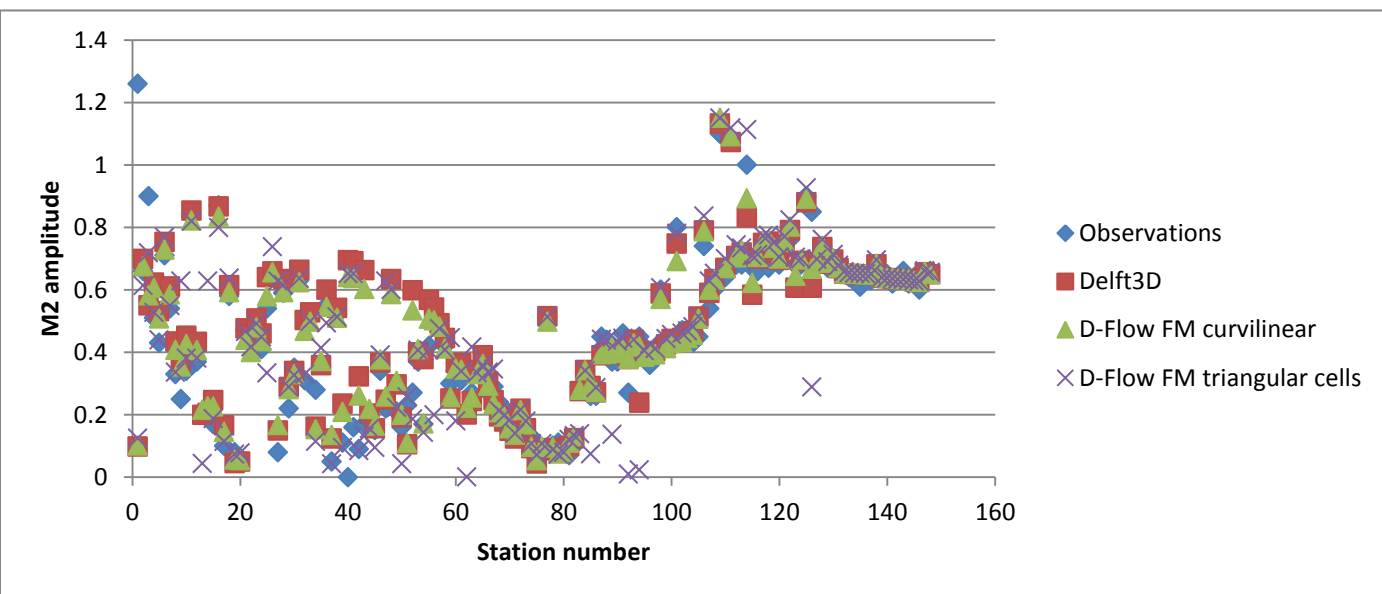


Figure 4-4: The M<sub>2</sub> amplitude of the three models compared to observations.

perform well in this regard for all components except for the grid with triangular cells for the K1 tide, but it is likely that this could be improved by calibrating the grid. Also, this grid has a resolution that is a lot lower than the other two grids. This shows itself through the computation times; the grid with triangular cells took less than 20 minutes to complete, while Delft3D and D-Flow FM square cells took almost 2 and almost 3 hours respectively. In terms of numerical performance (computation time per time step per grid cell) this translates to the grid with triangular cells being 5% faster than Delft3D while the grid with square cells is as much as 140% slower. This is remarkable, since in the previous chapter the D-Flow FM square cells grids performed the fastest of the three grids. Considering the results displayed above, the grid with triangular cells performs remarkably well compared with the other two grids, considering the low resolution and the grid not being calibrated. However, since ARCADIS' grid was not optimal with respect to grid standards (see Appendix A and Appendix D for details about the grids used in this chapter), it is expected that if this grid were to be properly optimized the results would be better compared with the grid with triangular cells. Despite this, the low computation time required for running the triangular grid and its relatively good comparability with observations make this a model that could be used for further projects/studies, especially considering that the Delft3D model has been used for years with good results. It also means this model can serve as the large scale Arabian Gulf model that is the foundation of the nested Abu Dhabi model that is described in the next section. The somewhat worse results near the

region of Abu Dhabi do not matter much, as the resolution will be enhanced greatly which is expected to greatly improve the results.

## 5. Modeling the Abu Dhabi area

After having constructed a large scale flow model with a flexible mesh and having concluded that this model simulates the overall water motion accurate enough, it is possible to construct a detailed model of the coastal waters around Abu Dhabi and to simulation the spreading of salt. In the introduction it was described that higher salt concentrations can have strong adverse effects on the environment. The goal of this part of this study is to gain insight in the area of influence of the salt emission of a desalination plant. Section 5.1 describes the experiment setup, including some details about the grid, information about different types of desalination plants and the desalination plant experiment setup. Section 5.2 compares the sea levels that are generated by the model to observations while section 5.3 discusses the spreading of saline water discharged by a desalination plant.

### 5.1 Setup of the experiment

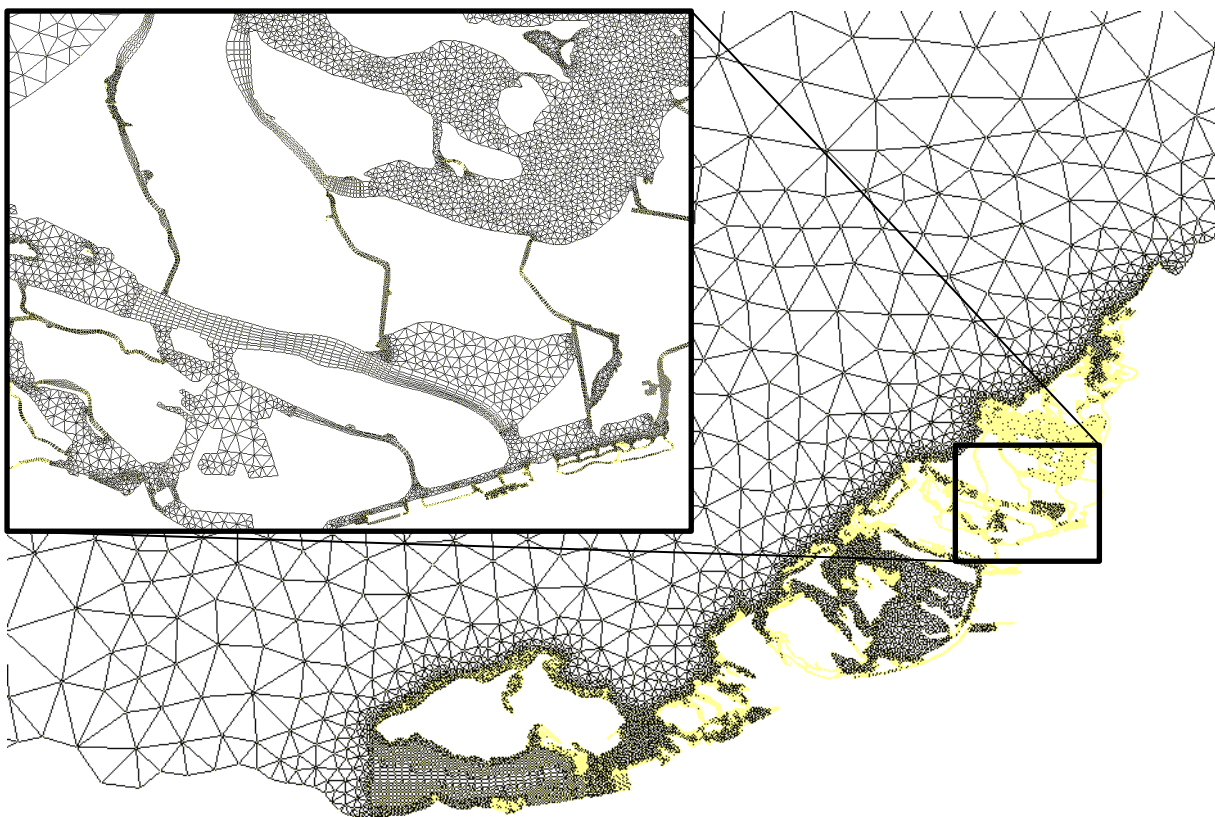


Figure 5-1: The part of grid outlined by a black square in Figure 4-2 after refinement near Abu Dhabi. An arbitrary section of this grid has been magnified for better visibility.

The grid that was used for this study was constructed separately from the large scale models described above and was subsequently connected to the grid with triangular cells described in the previous section. The overall Arabian Gulf grid with refinement had more than 5 times as many grid cells as the grid without refinement in the Abu Dhabi area. The grid in the Abu Dhabi region consists of curvilinear parts in the channels and parts with triangular cells where the coastal boundaries were too complex to allow for the usage of curvilinear grids (see also Figure 5-1). Since land boundary data were not available at the time of writing, the boundaries have been constructed by using Google Earth. For the bathymetry use was made of the Admiralty depth charts (3713, 2001) and (3715, 2001). These maps however contain very old data, going back as far as 1971, and contain many areas without data. To fill up these gaps and to get a more recent picture of the bathymetry around Abu

Dhabi, use was again made of Google Earth. For the bathymetry used in this study see Figure 5-2. The usage of Google Earth for both the boundary and the bathymetry was unavoidable, but since Google Earth images can be hard to interpret, the end result is a boundary and bathymetry that is strongly influenced by the opinion of the author. For example, large parts of the modeled area consist of mangroves, which are subject to flooding and drying. In this study, mangroves have been considered as land, since the shallow areas with a lot of obstruction will not affect the general flow too much.

This model, like the models in the previous sections, solves the depth averaged shallow water equations. Since salinity has an effect on the density, and thus leads to flow and salt concentrations that vary with depth, this is a strong simplification. It would have been preferred to use the three dimensional equations but at the time when this experiment was set up this functionality was not yet available for D-Flow FM and hence it is recommended that in future similar salinity experiments the three dimensional equations are solved. The boundary of the grid open to the Gulf of Oman has not changed, and hence the astronomical boundary conditions are identical to

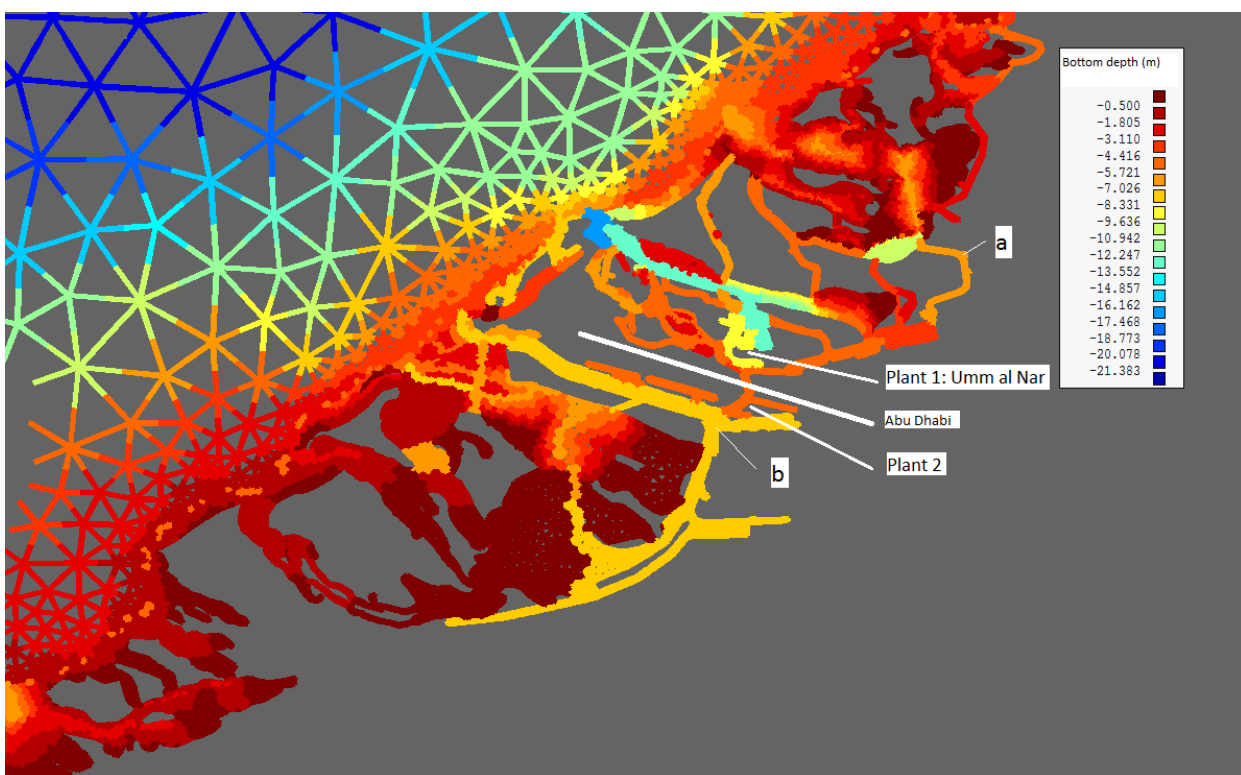


Figure 5-2: The bathymetry of the area of interest in the Abu Dhabi area. The locations of observation stations a and b have been marked as well as the locations of the two desalination plants used in this study.

the ones described in section 4.1. The initial salinity was chosen at 39 ppt (parts per thousand); a value which is on the low side for Abu Dhabi, even during summer, but it serves to enlarge the contrast between desalination and background water.

Next, the design of the sources of salinity in the form of desalination plants is discussed. There are several methods to produce fresh water from sea water. The two methods that are used most in the United Arab Emirates are Multi Stage Flash (MSF) and Reverse Osmosis (RO). Both methods have a different brine discharge to water intake ratio, and the salt concentrations and temperatures of the brine vary as well. For MSF plants, which require a lot of cooling water, 90% of the water that is taken in is released again. This released water consists of the brine, which has a concentration of 60-70 ppt, and the cooling water, which has ambient salinity. Combined this yields a

salinity of 45-50 ppt in the discharged water (Bleninger & Jirka, 2010). RO desalination plants do not require as much intake water and only 50% of the intake water is released as brine. This brine does have a concentration that is substantially higher than the combined brine released by MSF plants, namely between 65 and 85 ppt (Bleninger & Jirka, 2010).

For this study use was made of the Um Al Nar power and desalination plant as an example. This plant produces around  $136,400 \text{ m}^3/\text{day}$  of fresh water using RO desalination. In addition to this, it produces  $804,869 \text{ m}^3/\text{day}$  using MSF desalination. Combining the brine discharges for these RO and MSF modules, assuming the brines are mixed, this plant produces approximately  $7,300,000 \text{ m}^3 \text{ of brine}/\text{day}$  with an approximate concentration of 50 ppt. This corresponds to a salt flux of approximately 362 ton/day. The experiment with these characteristics will be called 'plant 1'. In addition to this, in order to study a case in which the brine discharge is lower, but the salinity of the brine is larger (even though it has no relation to a real desalination plant) another experiment called 'plant 2' has been conducted. In this experiment a smaller desalination plant with a brine discharge of  $3.4 \cdot 10^6 \text{ m}^3 \text{ of brine}/\text{day}$  and a brine concentration of 70 ppt (corresponding to approximately 238 ton salt/day) was placed near a channel in which the velocities are relatively high. The location was chosen such that the saline water spreads faster and an equilibrium state is expected to be reached faster.

In Delft3D a desalination plant can be specified by specifying a so-called 'intake point', a point where water taken up by the plant and thus removed from the ocean, and an 'outlet point', a point where the brine is discharged and hence water is added to the ocean. Between these points a difference in discharge and salinity of the removed/added water prescribed as well. This type of specifying a desalination plant leads to an accurate representation of reality. In D-Flow FM this functionality does not exist yet, and the boundary condition that functions to simulate the outlet of the desalination plant acts like a 'saline river'. This 'river' discharges water into the sea and has a salt concentration. Both the discharge and the salinity can vary in time, but in these experiments they are kept constant after the spin up time has passed (see below).

To validate the model, its output will be compared with observed sea surface variations only, as velocity or salinity measurements were not available. Unfortunately, the amount of sea level observation stations near Abu Dhabi is limited, and observation points suitable for these experiments were available for only two locations. Their locations are given in Figure 5-2 with their names being 'a' and 'b'. Despite the amount of observations being so limited, they can give an indication about the model performance. The data from these points have a reference level unequal to zero and are given in local time. Therefore, in order to be able to compare the observation data with model output the observation data have undergone some preprocessing.

The simulations ran from midnight on the first of September, 2012, until 10.40 hours on the 9<sup>th</sup> of November, 2012. In order to prevent numerical spin up effects of having an effect on the salt distribution, the brine discharge was started at midnight of the 6<sup>th</sup> of September, 2012.

## 5.2 Model comparison with observations of the sea level

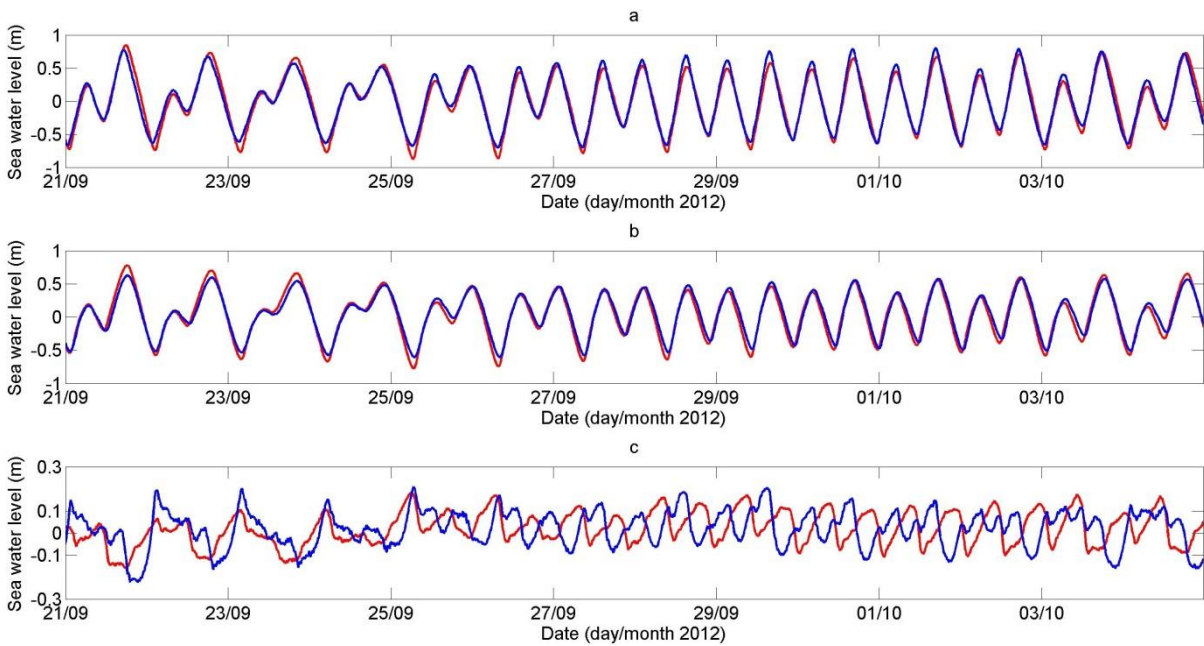


Figure 5-3: Model results (blue) and observations (red) of observation stations a (panel a) and b (panel b). Panel c displays the difference between model output and observations for station a (blue) and station b (red).

Table 5-1: Statistical parameters for the curves given in Figure 5-3, the difference between model output and observations. Values are given in cm.

	Station a	Station b
Mean	2	2
Maximum	22	18
Standard deviation	8	7

Figure 5-3 displays time series of both observations and model output during the period 21-09-2012 to 5-10-2012. This figure shows that the modelled and observed sea surface variations match well, though some mismatches, mostly at the high and low tides, occur. This is displayed in panel c, where the differences between model output and observations are given (see also Table 5-1 for some statistics

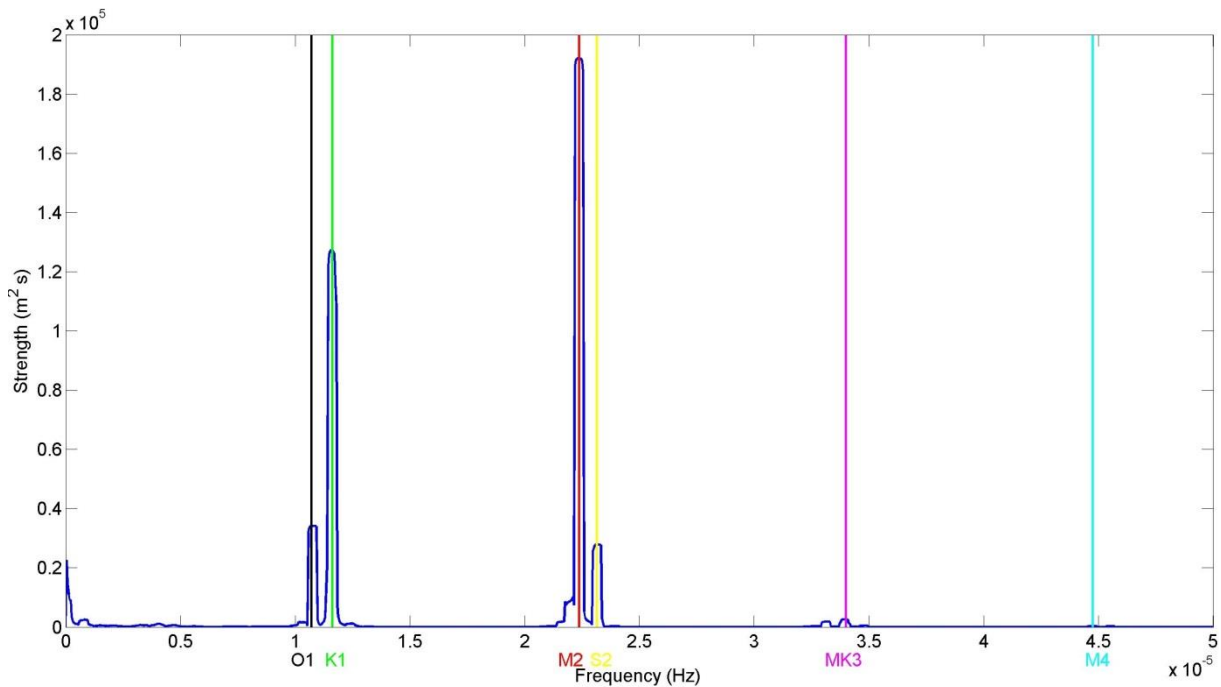


Figure 5-4: The tidal frequency spectrum from observation station a. Vertical lines indicate the frequencies of the major and other important or discussed tidal components.

regarding these curves). These results are reasonable, especially considering the lack of (accurate) data for bathymetry and land boundaries. Figure 5-4 shows the tidal frequency spectrum of observation station a. From this figure clearly the 4 main tidal components are visible. The tidal component that is produced by the two largest tidal components ( $M_2$  and  $K_1$ ), the  $MK_3$  component, is visible with a small peak. The component that is produced by the interaction of the  $M_2$  tide with itself, the  $M_4$  component, is only just visible but very small. In a similar graph produced for observation station b, a similar pattern is visible. This is reflected in the amplitudes of the  $MK_3$  and  $M_4$  tides, which are less than 10% of the  $M_2$  amplitude.

### 5.3 Spreading of salt in the coastal waters of Abu Dhabi

Figure 5-5 shows the salinity in the area of Abu Dhabi for the plant 1 experiment for several dates. These dates and times were chosen such that between each successive panel exactly  $36 M_2$

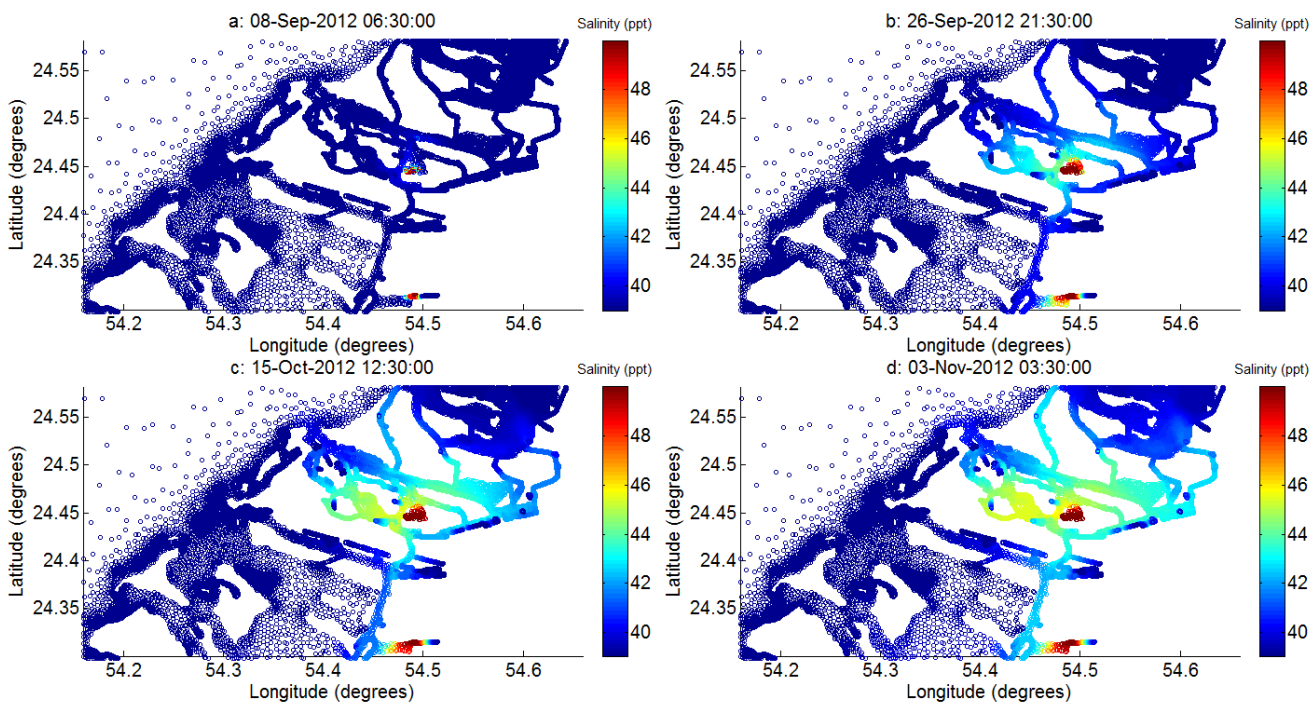


Figure 5-5: The salt concentration (in ppt) at 4 different dates. The high salt concentrations at the bottom of these figures were not prescribed and are expected to be software errors.

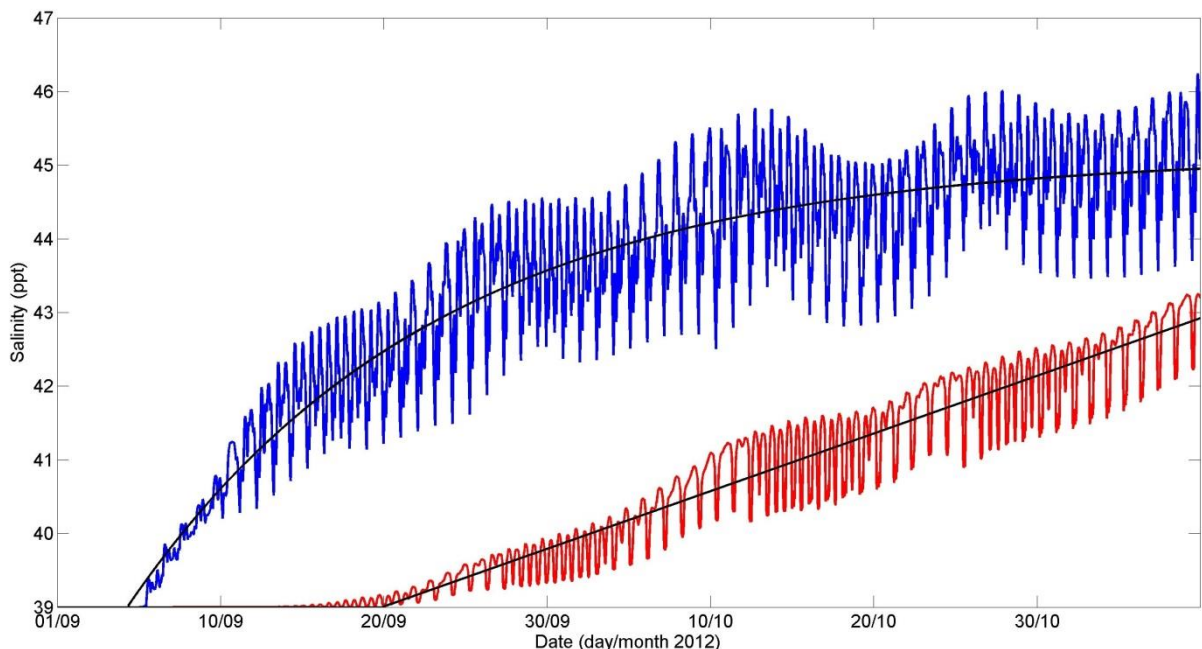


Figure 5-6: Salinity as a function of time for a point close to the location of plant 1 (blue) and in observation point b (red) with an exponential and a linear trend line respectively. Data are shown for the entire simulation.

periods have passed. This was done in order to have the smallest influence of tidal fluctuations possible. In this figure, the high salinity concentration visible in the south part of the picture was unexpected and unprescribed and no reason for its existence was found. The most likely explanation is that it's due to (unknown) software errors and it should

therefore be ignored when considering the figure. The figure shows that the effect of a desalination plant is quite large: in

panel d the salt has traveled more than 20 km away from the point of origin. Figure 5-6 shows that close to the desalination plant, the salinity is almost in dynamic equilibrium at the end of the simulation period. This is reflected in the trend line, which function is of the type  $s = s_0 + (s_e - s_0)(1 - e^{-\frac{t}{\tau}})$ , where  $s_0$  is the initial salinity at time (t in seconds) equals zero,  $s_e$  is the salinity of the adjusted state and  $\tau$  is the adjustment time scale. Fitting yields  $s_0 = 37.3$  ppt,  $s_e = 45.1$  ppt and  $\tau = 18.5$  days, with  $R^2 = 0.87$ . This suggests that the dynamic equilibrium concentration at this location is approximately 45 ppt, and the turnover time 18.5 days. This means that 18.5 days after the concentration starts to rise, the concentration has increased by 63% of the difference between final (dynamic equilibrium) and initial concentration. In this particular case that is approximately 2.2 ppt. Further away however, at observation point b, the salinity is still rising almost linearly. This means that given further time, the salinity as caused by the desalination plant would rise and spread even further than displayed by Figure 5-5d. In Abu Dhabi there exists not just a single desalination plant, but several, and no large sources of fresh water are present. The combined effects of these desalination plants are likely to have an effect that can be seen throughout the coastal waters of Abu Dhabi. In addition, the initial salinity that was used is lower than the values that can be found near Abu Dhabi (see for example Figure 2-3). In the case of a higher initial salinity, it is expected that the salt concentrations in the Abu Dhabi region will reach high levels.

Figure 5-7 shows time series of the salinity for 2 points of the Plant 2 experiment. In this experiment the location was chosen near a channel with high velocities so that equilibrium would be reached faster. The salinity does rise faster than in the plant 1 experiment, but the higher salinity of the brine prevents equilibrium from being reached as fast as in the plant 1 experiment. This means that the simulation time in this experiment was insufficiently long to determine how far the final influence of this desalination plant reaches. Another difficulty to determine this is that in addition to the unprescribed salt influx visible in near the bottom of Figure 5-5 another unprescribed salt influx appears at a different location.

Now to discuss the mechanisms of the salt spreading. Recall from section 2.5 that

$$\vec{T} = \langle \vec{u}(H + \eta)s \rangle = \frac{1}{T} \int_{-\frac{1}{2}T}^{\frac{1}{2}T} \overline{u(t)}(H + \eta(t))s dt, \quad (61)$$

$$\vec{T}_m = \langle \vec{u} \rangle \langle H + \eta \rangle \langle s \rangle, \quad (62)$$

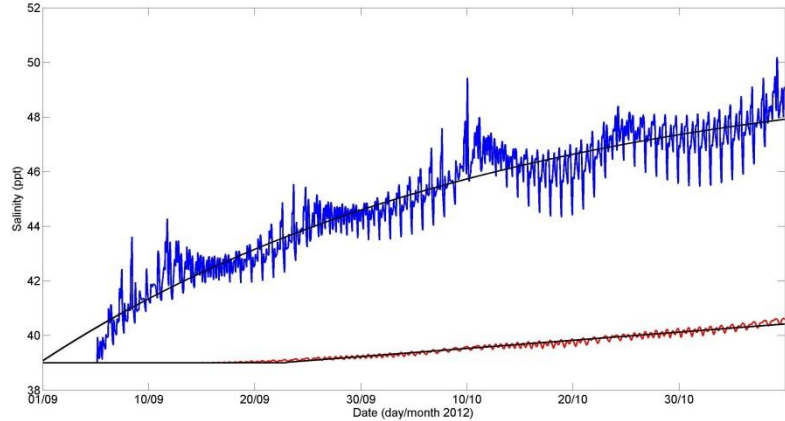


Figure 5-7: Salinity as a function of time for a point close to the location of Plant 2 (blue) and at a location a bit further away (red) with an exponential and a linear trend line respectively. Data are shown for the entire simulation.

$$\vec{T}' = \langle s \rangle \langle \vec{u}'\eta' \rangle + \langle \vec{u} \rangle \langle s'\eta' \rangle + \langle H + \eta \rangle \langle \vec{u}'s' \rangle + \langle \vec{u}'s'\eta' \rangle, \quad (63)$$

$$\vec{T}'' = \langle \vec{u}'s' \rangle \langle H + \eta \rangle + \langle \eta's' \rangle \langle u \rangle + \langle \vec{u}'s'\eta' \rangle. \quad (64)$$

In these equations  $\vec{T}$  is the residual salt transport,  $\vec{T}_m$  is the contribution to the residual salt transport due to the mean flow and mean salinity,  $\vec{T}'$  is the contribution to the residual salt transport by fluctuations in all variables and  $\vec{T}''$  is the contribution to the residual salt transport that only includes fluctuations of the salinity. From these equations the ratio of  $T_m$  and  $T$  can be computed through taking the absolute value of the velocity:

$$\frac{T_m}{T} = \frac{\sqrt{\langle u \rangle^2 + \langle v \rangle^2} \langle H + \eta \rangle \langle s \rangle}{\langle \sqrt{u^2 + v^2} (H + \eta) s \rangle}. \quad (65)$$

Similarly the ratios of  $T'$  and  $T''$  with  $T$  can be computed. In Figure 5-8 these ratios are displayed for the plant 1 experiment, but the plant 2 experiment gives nearly the same results. The fact that  $T'$  and  $T''$  can be both negative and positive means that the terms describing fluctuations in salt transport can both amplify and reduce the mean transport. The figure shows that  $T_m$  is dominant at most

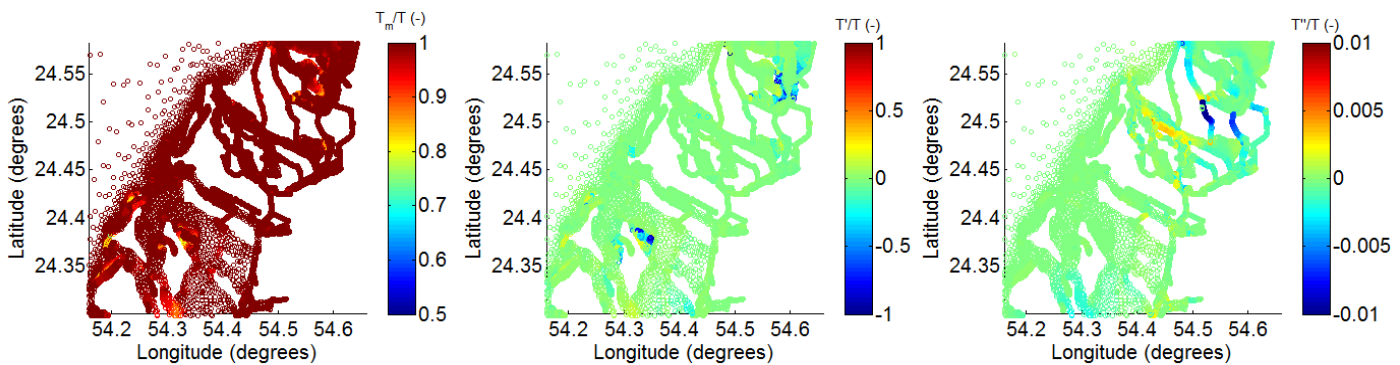


Figure 5-8: Ratios of the salt transport between the mean and fluctuation terms and the total salt transport in the coastal waters of Abu Dhabi. Results are displayed for the plant 1 experiment.

locations in Abu Dhabi, but that the fluctuation terms are important at a select few locations. Comparing this figure with Figure 5-2 it can be seen that these locations have in common that they occur at locations where the geometry and/or the bathymetry vary quickly.  $T''$  has its largest values in very narrow channels. From the fact that  $T'/T$  is much larger than  $T''/T$  it can be deduced that fluctuations in the water transport are much more important than fluctuations in salinity. Besides this, it is found that the first term on the right hand side of equation 63) is by far dominant in this equation, again showing that fluctuations in water transport are more important than fluctuations in salinity.

In order to compute some time scales, regard the selected domain around the plant 2 experiment as is displayed in Figure 5-9. In other areas, due to the large variability in bathymetry and coastal boundaries, and in addition to that the usage of triangles instead of rectangles, it is difficult to determine the average mass of salt  $\langle M \rangle$ , the average volume of water  $\langle V \rangle$ , the average salt transport out of or through a region



Figure 5-9: The part of the grid around plant 2 in which the residence and flux times are computed. In red the line along which the plant discharges, in green the sea boundaries and locations of the cross sections as defined in D-Flow FM.

$\langle |\vec{T}| \rangle$  and the average transport of water out of or through a region  $\langle q \rangle$  in this domain. Delft3D has tools that allow a user to determine area and volume of a grid, but these tools do not exist yet for D-Flow FM. This would produce high inaccuracies when computing the residence and flushing times in the region near plant 1, but plant 2 is located at the edge of a small channel with a constant depth (see also Figure 5-9). This is the reason that only this selected region is used for the computation of the time scales. Due to the simple geometry the area and volume of the domain can be estimated relatively accurately. In addition to this, the grid in this channel consists of 2 equal-size triangles in the cross channel direction, which makes the determination of the fluxes in the cross channel relatively accurate too. The usage of so called 'cross sections', which calculate water discharges through a certain cross section allows for an accurate determination of  $q$ . For the plant 2 experiment model results indicate that the velocity has amplitudes of about 0.5 m/s. In the selected domain around plant 2, where the cross sections are placed at the green lines in Figure 5-9, there is a net water transport into the channel through the southern cross section and net outward transport through the northern cross section. The difference between these ( $\approx 15 \text{ m}^3/\text{s}$ ) is not large enough to explain the influx of almost  $40 \text{ m}^3/\text{s}$  of brine that is discharged into the channel. Thus, approximately  $25 \text{ m}^3/\text{s}$  is unaccounted for. For the computation of the flushing time only the average flux of  $6 \text{ m}^3/\text{s}$  into the channel at the southern end was used, as the discharge of brine is not really 'fresh' water. The flushing time in this domain is approximately 3.4 days, meaning that the water in this basin of which the borders are defined by the green lines is completely refreshed by water coming from outside this basin and is not discharged by the desalination plant in approximately 3.4 days.

For the computation of the residence time the value of the salt transport out of the domain is required. Recall from section 2.5 that the residence time is given by  $\tau_r = \frac{\langle M \rangle}{Y}$ , with  $Y = \int s * \vec{u} \cdot \vec{n} dA$  the value of the residual salt transport out of the domain and  $\langle M \rangle$  the average mass of the salt present in the domain. Since the cross sections do not compute the salt flux across it, it is harder to determine  $Y$  than it is to determine  $q$ . For the computation of  $Y$ ,  $T$  in the direction normal to the cross section was computed for a location halfway between the two coasts of the channel at that point and successively multiplied with the depth and width of the channel at the location of the cross section. For the computation of the total mass both the volume and the average salinity in the selected domain are required. The volume of the domain was computed by simplifying the region displayed in Figure 5-9 to the geometry of Figure 5-10, where the domain consists of two channels with a constant width and depth. Thus, by using averages of the channel width (the depth is constant in each channel in the model) the volume in the domain is computed by adding the volume of the two channels. At the end of the simulation period, the salt concentration in the channel is not in dynamic equilibrium yet (see also Figure 5-7), and that is reflected by the salt flux out of the basin, which is more than 2 times smaller than the salt influx through brine. With this salt flux out of the basin and

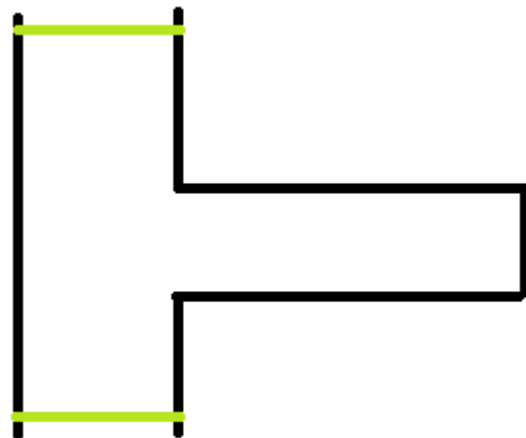


Figure 5-10: The simplified representation of the domain given in Figure 5-9 used for the computation of the volume of the selected domain

salinity, the residence time in this basin is approximately 44 hours. This means that a salt particle anywhere in this basin takes approximately 44 hours to leave this basin. If in the unsimulated future a dynamic equilibrium would be reached, in which the influx of salt is equal to the outflux of salt, that is, 238 ton salt per day, and the dynamic equilibrium concentration would be equal to the dynamic equilibrium concentration given by the trend line in Figure 5-7 (50 ppt), the residence time would be reduced to 19 hours.

## 6. Conclusions

In this study results have been shown of different models that simulate tide-induced flow in either the entire Persian Gulf, or in the coastal area of Abu Dhabi. The Arabian Gulf was first modeled as a rectangular basin and modeled using an analytical model and numerical models in Delft3D and in the newly developed D-Flow FM using both curvilinear and triangular cells. Subsequently the Arabian Gulf was modeled using a realistic representation using Delft3D and D-Flow FM, with the latter using again both curvilinear and triangular cells. In the last part of this study the coastal waters around Abu Dhabi were modeled using a flexible mesh and the influence of desalination plants on the salinity distribution in these waters was investigated. The research aims were to develop a clear understanding of tidal motion in the Arabian Gulf, to quantify tidal and residual flow in the coastal area of Abu Dhabi and to quantify spreading of salt as emitted by a desalination plant in the coastal area of Abu Dhabi. In addition differences between Delft3D and D-Flow FM were investigated.

With regard to the first aim it has been found that the dominant tidal motion is induced by the  $M_2$ ,  $S_2$ ,  $K_1$  and  $O_1$  tidal constituents, a result that matches well with observations and previous studies. With respect to the second aim it has been found that the tidal motion is comparable to that of the Arabian Gulf as a whole and that the residual flow plays an important role for the transport of salt. The role of fluctuations of the velocities, depth and salinity can play an important role for the salt transport of salt, predominantly at those locations where the bathymetry or the coasts vary within short distances.

With regard to the third aim, desalination plants have been found to have a large effect on the coastal waters of Abu Dhabi, and the salinity rises considerably in the environment of a desalination plant. Combined with high ambient salinities and presence of multiple desalination plants in Abu Dhabi, the desalination plants could pose a considerable risk for the environment. The model that was used to come to this conclusion performed well with respect to simulating sea levels, but still differences of up to 25 cm with observations existed. This could be improved by using an accurate land boundary and bathymetry. In all models the depth averaged shallow water equations have been solved. Salinity, through its relation with density, will vary over the vertical, and for a future experiment it is recommended that the model(s) solve the three-dimensional equations of motion.

In general, it is found that D-Flow FM compares well Delft3D. In the experiments with a rectangular basin both models were shown to compare very well, even though the model with triangular cells performs somewhat worse than the models with square cells. A better comparison could have been made by incorporating friction into the analytical solution, so that the numerical models can be compared to an analytical solution. For the models with a realistic geometry and bathymetry, both D-Flow FM and Delft3D compared well to observations. The differences were small, but are expected to increase when the quality of the Delft3D grid is improved. The grid with triangular cells in D-Flow FM had a low resolution, and its results can be further increased by improving that, and by calibrating it better to observations. But considering the low computation time this model is relatively good. It remains unclear whether D-Flow FM is faster than Delft3D or not, as sometimes Delft3D was faster (chapter 4) and at other times D-Flow FM was faster (chapter 2.5). The grids with triangular cells had a computation time per time step per cell that was consistently faster than either D-Flow FM with a curvilinear grid and Delft3D, but these conclusions were based on a limited number of simulations. The good results of the flexible mesh near the area of Abu Dhabi show that a flexible mesh is suited for numerical modeling. The possibilities for local refinement and flexible borders make it especially useful for areas like those around Abu Dhabi with

its strongly varying bathymetry and coastline. D-Flow FM in its current state is not recommended for professional use, due to the lack of functionalities like temperature modeling, sediment transport or the inclusion of salinity into the restart files, but this study has shown that it shows much promise once functionalities like these are incorporated.

## **7. Acknowledgements**

The author would like to thank Professor Huib de Swart for answering many questions and making sure that this study was scientific enough. The author is also very grateful to Jeroen Adema for his help with getting to understand Delft3D and his useful suggestions. Furthermore, the author would like to thank Wim van Balen from Deltares for his help with getting familiar with D-Flow FM, Gijs van Banning, Bart Grasmeijer and the other employees of ARCADIS Zwolle for their useful tips or help with software.

## 8. References

- 3713, A. m., 2001. *Approaches to Abu Dhabi (Abu Zaby)*. s.l.:s.n.
- 3715, A. m., 2001. *Abu Dhabi (Abu Zaby) and Umm An Nar*. s.l.:s.n.
- Abu Dhabi Department of Transport, n.d. [Online]  
Available at: [http://dot.abudhabi.ae/en/info/Maritime\\_Sector\\_in\\_DoT](http://dot.abudhabi.ae/en/info/Maritime_Sector_in_DoT)  
[Accessed 14 2 2013].
- Abu Dhabi Water & Electricity Company, 2012. *Existing projects*. [Online]  
Available at: <http://www.adwec.ae/Existing.html>  
[Accessed 16 10 2013].
- Admiralty co-tidal Atlas Persian Gulf, 1999. *Principal Harmonic constituents*, Taunton: United Kingdom Hydrographic Office.
- Admiralty tide tables, 2002. *Indian ocean and south china sea, Vol. 3, NP 203-02*. s.l.:United Kingdom Hydrographic Office.
- Alkyon, 2004. *Large-scale flow models; Persian Gulf*, Marknesse: Alkyon.
- Alkyon, 2006. *Mangrove Park Development, Abu Dhabi; Refreshment, beach profiles and sediment plume dispersion*, Marknesse: Alkyon.
- Blain, C. A., Preller, R. H. & Rivera, A. P., 2002. Tidal Prediction Using the Advanced Circulation Model (ADCIRC) and a Relocatable PC-based System. *Oceanography*, 15(1), pp. 77-87.
- Bleninger, T. & Jirka, G. H., 2010. *Environmental planning, prediction and management of brine discharges from desalination plants*, Muscat: Middle East Desalination Research Center.
- Carbajal, N., 1997. Two applications of Taylor's problem solution for finite rectangular semi-enclosed basins. *Continental Shelf Research*, 17(7), pp. 803-817.
- Cartwright, D. E., 1968. A unified analysis of tides and surges round north and east Britain. *Philosophical Transactions of the Royal Society of London*, 263(A. 1134), pp. 1-55.
- Chatfield, C., 1975. *The Analysis of Time Series: Theory and practice*. London: Chapman and Hall.
- Chen, C. et al., 2011. Tidal dynamics in the Gulf of Maine and New England Shelf: An application of FVCOM. *Journal of geophysical research*, Volume 116, p. C12010.
- Chen, C., n.d. [Online]  
Available at: <http://fvcom.smast.umassd.edu/index.html>  
[Accessed 29 7 2013].
- Chen, C. et al., 2008. Complexity of the flooding/drying process in an estuarine tidal-creek salt-marsh system: An application of FVCOM. *J. Geophys. Res.*, 113(C7).
- Cushman Roisin, B. & Beckers, J. M., 2011. *Introduction to geophysical fluid dynamics*. 2nd ed. Amsterdam: Elsevier.

Davies, A. M. & Jones, J. E., 1995. The influence of bottom and internal friction upon tidal currents: Taylor's problem in three dimensions. *Continental Shelf Research*, 15(10), pp. 1251-1285.

de Swart, H. E., 2012. *Ocean Waves, lecture notes*. Utrecht: s.n.

Deltares, 2011. *Delft3D-Flow, user manual*. Delft: Deltares.

Deltares, n.d. *Deltares website*. [Online]

Available at: <https://publicwiki.deltares.nl/display/nghs/Next+Generation+Hydro+Software>  
[Accessed 22 3 2013].

Deltares, n.d. *Open Earth tools*. [Online]

Available at: <https://publicwiki.deltares.nl/display/OET/OpenEarth>  
[Accessed 30 7 2013].

DHI, n.d. *mike DHI*. [Online]

Available at: <http://www.mike-by-dhi.com/>  
[Accessed 29 7 2013].

Díez-Minguito, M., Contreras, E. & Losada, M. A., 2013. Spatio-temporal distribution, along-channel transport, and post-riverflood recovery of salinity in the Guadalquivir estuary (SW Spain). *Journal of geophysical research*, Volume 118, pp. 2267-2278.

Dijkstra, H. A., 2012. *Lecture Notes: Turbulence and Mixing, The energy cycle of the ocean*. Utrecht: s.n.

Elshorbagy, W., Azam, M. & Taguchi, K., 2006. Hydrodynamic characterization and Modeling of the Arabian Gulf. *Journal of Waterways*, 132(1), pp. 47-56.

Environmental Agency Abu Dhabi, 2009. *Abu Dhabi water resources master plan*, Abu Dhabi: Environmental Agency Abu Dhabi.

Gill, A. E., 1982. *Atmosphere-ocean Dynamics*. 1 ed. San Diego: Academic Press.

Godin, G., 1991. Frictional effects in river tides. In: B. B. Parker, ed. *Tidal Hydrodynamics*. s.l.:John Wiley & Sons, Inc, pp. 379-402.

Gupta, K. K. & Meek, J. L., 1996. A brief history of the beginning of the finite element method. *International journal for numerical methods in engineering*, Volume 39, pp. 3761-3774.

Hashim, A. & Hajjaj, M., 2005. *Impact of desalination plants fluid effluents on the integrity of seawater, with the Arabian Gulf in perspective*. Santa Margherita, Elsevier.

Hendershott, M. C. & Speranza, A., 1971. Co-oscillating tides in long, narrow bays; the Taylor problem revisited. *Deep Sea Research and Oceanographic Abstracts*, 18(10), pp. 959-980.

Huang, H. et al., 2008. FVCOM validation experiments: Comparisons with ROMS for three idealized barotropic test problems. *J. Geophys. Res.*, 113(C7).

- Hutter, K., Wang, Y. & Chubarenko, I. P., 2011. Chapter 12: The Role of the Earth's Rotation: Oscillations in Semi-bounded and Bounded Basins of Constant Depth. In: *Physics of Lakes, Volume 2: Lakes as oscillators*. s.l.:Springer, pp. 49-113.
- Johnson, H. K. et al., 2005. Modelling of waves and currents around submerged breakwaters. *Coastal Engineering*, 52(10-11), pp. 949-969.
- Kämpf, J. & Sadrinassab, M., 2005. The circulation of the Persian Gulf: a numerical study. *Ocean science discussion*, pp. 129-164.
- Kernkamp, H. W. J., van Dam, A., Stelling, G. S. & de Goede, E. D., 2011. Efficient scheme for the shallow water equations on unstructured grids with application to the Continental Shelf. *Ocean Dynamics*, Volume 61, pp. 1175-1188.
- Kuijper, C. et al., 2004. *Morphological modelling of the Western Scheldt*, s.l.: s.n.
- Lai, Z. et al., 2013. Initial spread of 137Cs from the Fukushima Dai-ichi Nuclear Power Plant over the Japan continental shelf: a study using a high-resolution, global-coastal nested ocean model. *Biogeosciences*, Volume 10, pp. 5439-5449.
- Le Provost, C., 1991. Generation of overtides and compound tides (Review). In: B. B. Parker, ed. *Tidal Hydrodynamics*. s.l.:John Wiley & Sons, Inc, pp. 269-295.
- Lesieur, M. & Métais, O., 1996. New trends in large-eddy simulations of turbulence. *Annual Review of Fluid Mechanics*, Issue 28, pp. 45-82.
- Lesser, G. R., Roelvink, J. A., Kester, J. A. T. M. v. & Stelling, G. S., 2004. Development and validation of a three-dimensional morphological model. *Coastal engineering*, Volume 51, pp. 883-915.
- Luetlich, R. A., Westerink, J. J. & Scheffner, N. W., 1992. *ADCIRC: An Advanced Three-Dimensional Circulation Model for Shelves, Coasts, and Estuaries. Report 1. Theory and Methodology of ADCIRC-2DDI and ADCIRC-3DL*, s.l.: s.n.
- Luijendijk, A., 2001. *Validation, calibration and evaluation of a Delft3D-FLOW model with ferry measurements; Msc thesis*, Delft: s.n.
- Matsumoto, K., Takanezawa, T. & Ooe, M., 2000. Ocean Tide Models Developed by Assimilating TOPEX/POSEIDON Altimeter Data into Hydrodynamical Model: A Global Model and a Regional Model around Japan. *Journal of Oceanography*, pp. 567-581.
- Moin, P. & Mahesh, K., 1998. Direct Numerical Simulation: A Tool in Turbulence Research. *Annual Review of Fluid Mechanics*, Volume 30, pp. 539-78.
- NOAA, 2001. *ETOPO2 Global 2' Elevations*. s.l.:s.n.
- Parker, B. B., 1991. The relative importance of the various nonlinear mechanisms in a wide range of tidal interactions (Review). In: B. B. Parker, ed. *Tidal Hydrodynamics*. s.l.:John Wiley & Sons, Inc., pp. 237-268.

- Pawlowicz, R., Beardsley, B. & Lentz, S., 2002. Classical tidal harmonic analysis including error estimates in MATLAB using T\_TIDE. *Computers & Geosciences*, 28(8), p. 929–937.
- Perrone, T. J., 1979. *Winter Shamal in the Persian Gulf*, Monterey, California: Naval Environmental Prediction Research Facility.
- Pous, S., Carton, X. & Lazure, P., 2012. A Process Study of the Tidal Circulation in the Persian Gulf. *Open Journal of Marine Science*, Volume 2, pp. 131-140.
- Prandle, D., 1984. A modelling study of the Mixing of 137Cs in the seas of the European continental shelf. *Philosophical transactions of the Royal society of London*, A(310), pp. 407-436.
- Prandle, D., 1991. Tides in estuaries and embayments (review). In: B. B. Parker, ed. *Tidal hydrodynamics*. s.l.:John Wiley & Sons, Inc, pp. 125-152.
- Proctor, R., Flather, R. A. & Elliot, A. J., 1994. Modelling tides and surface drift in the Arabian Gulf-- Application to the Gulf oil spill. *Continental Shelf Research*, 14(5), pp. 531-545.
- Reynolds, R. M., 1993. Physical Oceanography of the Gulf, Strait of Hormuz, and the Gulf of Oman - Results of the Mt Mitchell Expedition. *Marine Pollution bulletin*, pp. 35-59.
- Ridderinkhof, H., 1988. Tidal and residual flows in the western Dutch Wadden Sea 1: Numerical model results. *Netherlands Journal of Sea Research*, 22(1), pp. 1-21.
- Ridderinkhof, H. & Zimmerman, J. T. F., 1992. Chaotic Stirring in a Tidal System. *Science*, 258(5085), pp. 1107-1111.
- Rienecker, M. M. & Teubner, M. D., 1980. Note on frictional effects in Taylor's problem. *Journal of Marine Research*, 38(2), pp. 183-191.
- Rijkswaterstaat, 2013. *Getijtafels voor Nederland 2014*. Den Haag: Sdu Uitgevers.
- Rizal, S., 2002. Taylor's problem—influences on the spatial distribution of real and virtual amphidromes. *Continental Shelf Research*, 22(15), p. 2147–2158.
- Røed, L. P., 2011. *Lecture notes: Atmosphere and Oceans on computers: Fundamentals*. Oslo: s.n.
- Roos, P. C. & Schuttelaars, H. M., 2009. Horizontally viscous effects in a tidal basin: extending Taylor's problem. *Journal of Fluid Mechanics*, Volume 640, p. 421–439.
- Sun, Y. et al., 2012. Simulation of brine discharge near sea farms in the Korea Strait. *Desalination and Water Treatment*, Volume 43, pp. 201-211.
- Taylor, G. I., 1920. Tidal oscillations in gulfs and rectangular basins. *Proceedings of the London Mathematical Society*, pp. 148-181.
- The university of north carolina, n.d. ADCIRC. [Online]  
Available at: <http://adcirc.org/>  
[Accessed 29 7 2013].

Vallis, G. K., 2006. *Atmospheric and Oceanic Fluid dynamics*. 1st ed. Cambridge: Cambridge University Press.

van Balen, W., 2013. Delft: s.n.

van Dam, A., Kernkamp, H., van der Pijl, S. & van Balen, W., 2012. *D-Flow Flexible Mesh, user manual*, Delft: Deltares.

Warren, I. R. & Bach, H. K., 1992. MIKE 21: a modelling system for estuaries, coastal waters and seas. *Environmental Software*, 7(4), pp. 229-240.

Weber, J. E. H., 2010. *GEF4610, dynamic oceanography: waves and wave-induced mass transport in the ocean, lecture notes*. Oslo: s.n.

Zimmerman, J. T. F., 1978. On the Euler-Lagrange transformation and the Stokes' drift in the presence of oscillatory and residual currents. *Deep-Sea research*, Volume 26A, pp. 505-520.

## Appendix A. Qualitative details of grid building in Delft3D and D-flow FM

The main difference between Delft3D and D-Flow FM is the grid. Therefore, in this section the differences between the grids and some things that one should be aware of while building the grid are discussed. Section 2.4.1 covers the curvilinear grid, while section 2.4.2 covers the unstructured grid.

### A1. The curvilinear grid as used by Delft3D

Figure A-1 gives an example of a curvilinear grid. As can be seen, a curvilinear grid basically consists of rectangles and squares that are allowed to vary in shape somewhat. However, for the best accuracy, the deviations from a uniform grid of squares with no curvature should be kept to a minimum. There are three descriptors that determine how much a curvilinear deviates from a

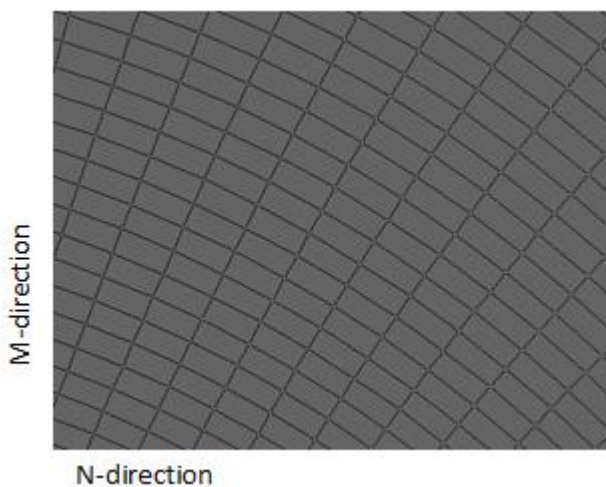


Figure A-1: A curvilinear grid with 2 dimensions.

standard grid: orthogonality, smoothness and aspect ratio. The definitions as described below come from the Delft3D Flow user manual (Deltares, 2011).

Orthogonality is defined as the angle between the grid lines in the M- and N-direction. Hence, a strongly curved grid will have a grid that is not completely orthogonal. The smoothness is defined as the ratio between the sizes of two neighboring cell lines. This means that there is a difference between smoothness in the M-direction and smoothness in the N-direction and these quantities can be treated separately. So if a cell has a different size than its neighbors, the smoothness will be unequal to one. The aspect ratio is defined

as the ratio between the size of a cell in one direction and the size of a cell in the other direction. It follows that a non-square rectangle has an aspect ratio that differs from one.

The user manual recommends the following values:

- Orthogonality: the cosine of the angle between two grid lines should be below 0.02, with an optimum value of 0.
- Aspect ratio: This value should be in the range 1-2, with an optimum value of 1.
- Smoothness: This value should have a maximum of 1.2 in the area of interest up to 1.4 further away, with an optimum value of 1.

In practice however, these values can be somewhat higher since, especially near a coast, it is hard to satisfy all these criteria. Nevertheless, it is important to keep these criteria as close to their optimum values as possible. The grid generator of Delft3D, RGFGrid, has options to display these grid descriptors on the grid as well as an orthogonalization function to improve the quality of the grid.

### A2. The unstructured grid as used by D-Flow FM

Obviously, unlike with the curvilinear grid, an unstructured grid does not only consist of squares and rectangles, but of triangles, quadrilaterals, pentagons and hexagons as well. This variability brings two major advantages. The first is that these different shapes allow for a grid

boundary that more accurately follows a realistic boundary. The second is that this variability allows to locally increase the cell density, hence improving the accuracy in that region. The result is that building an entirely different high accuracy model nested within a larger scale model is unnecessary in D-Flow FM.

In D-Flow FM four elements that make up a mesh can be distinguished:

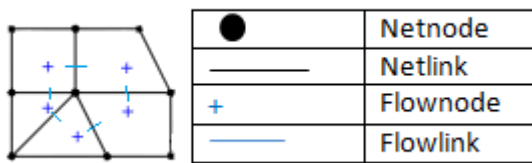


Figure A-2: Grid descriptors in an unstructured mesh.

Netnodes: the corners of a cell

Netlinks: the connection between two netnodes, defining the border of a cell

Flownodes: The circumcenter of a cell, with triangles this is the center of the circumscribed circle (see also Figure A-5)

Flowlinks: a line segment connecting two flownodes.

Figure A-2 shows these net descriptors in a comprehensible way.

Just like with the curvilinear grid, orthogonality and smoothness are important as well, but they have somewhat different definitions. Orthogonality is defined as the cosine of the angle between a flowlink and a netlink, while the smoothness is defined as the ratio of the area between

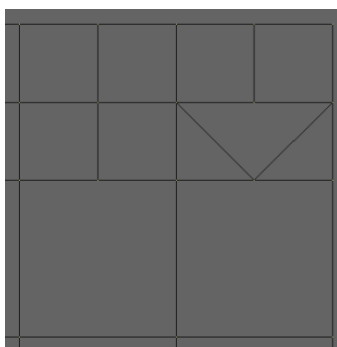


Figure A-3: 2 hanging nodes.

two adjacent cells (van Dam, et al., 2012). Hence, for the same grid, Delft3D and D-Flow FM can display different values for orthogonality and smoothness. Figure A-4 gives an illustration of how either smoothness or orthogonality can be perfect in the mesh while the other one is poor. A special case of an orthogonality problem occurs when one cell is much bigger than another cell, i. e. it is a smoothness problem as well. This problem is illustrated in Figure A-3. It is clear from this figure that the angle between flowlink and netlink is far from 90 degrees at the transition between refined cells and unrefined cells and hence both smoothness and orthogonality are insufficient at a hanging node.

Just like with Delft3D, in D-Flow FM the highest model accuracy is obtained when the orthogonality equals 0 and the smoothness equals 1. No standards for maximum values have been set yet because of the newness of this software.

In addition to these somewhat familiar features, a new feature that requires attention is the presence of so-called 'right triangles' and 'open triangles'. A right triangle is a triangle for which one angle is 90 degrees. An open triangle is a triangle of which one angle is larger than 90 degrees. In grid

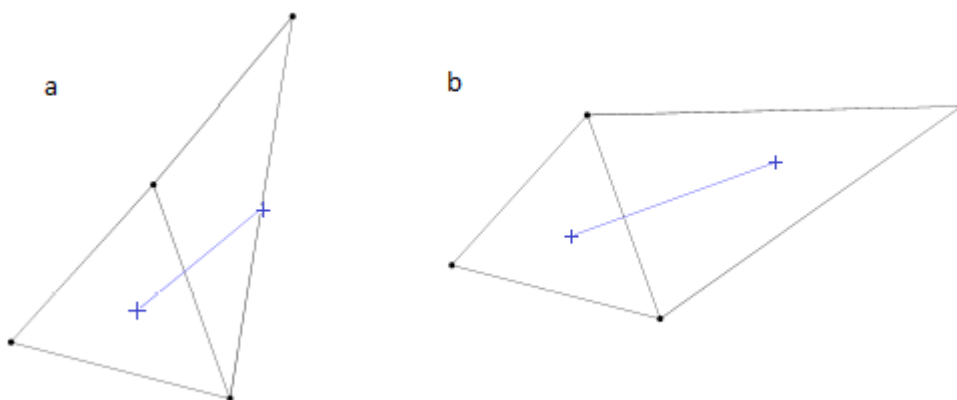
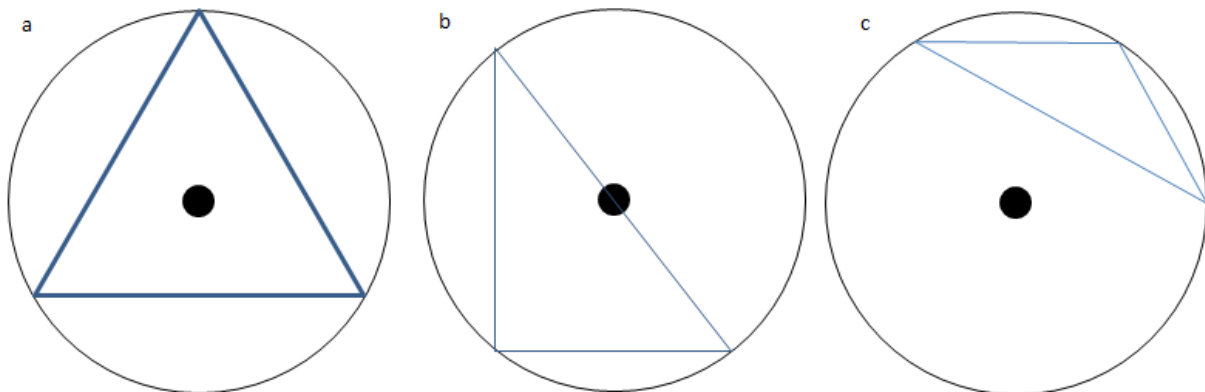


Figure A-4: Poor mesh properties due to violating either the smoothness or the orthogonality at the edge connecting two triangles. (a) shows perfect smoothness, but poor orthogonality. (b) shows perfect orthogonality, but poor smoothness. Source: (van Dam, et al., 2012).

cells of such shape, the flownode lies respectively on the netlink or outside of the cell (see Figure A-5). It isn't hard to imagine that when a flownode, the point at which the water level is calculated, lies on a netlink, or even in a different cell, D-Flow FM has some problems with computing data in that point. The reason for this is that, like Delft3D, D-flow FM works with a so called staggered grid. This grid computes the sea surface level in the center of a grid cell, but the velocity is computed halfway between 2 grid cell centers. In the case of D-Flow FM, open or closed triangles lead to a distance between a sea surface and velocity point that is zero or negative. Therefore, right and open triangles should be avoided as much as possible. When a flow node has the same distance between all net links in the cell, i.e. an equilateral triangle, the accuracy is best and when building a grid this should be taken into account.



**Figure A-5: Illustration of hanging nodes. (a) A perfect equilateral triangle with the highest accuracy. (b) A triangle with one angle of 90 degrees (right triangle): the center of the circumscribed circle (flownode) lies on the edge of the triangle. (c) One angle of the triangle is larger than 90 degrees (open triangle) and the flownode lies outside the cell.**

Despite the fact that D-Flow FM can use and generate curvilinear grids, these grids are still considered as unstructured grids because of the way D-Flow FM works. Hence, the solution schemes and grid descriptors that were mentioned in the previous section are different and it is important to realize that the exact same model can have differing solutions and computation times for Delft3D and D-Flow FM.

But however nice an unstructured grid might sound, according to W. van Balen (personal communication, 14-03-2013) curvilinear grids in D-Flow FM are more accurate than triangular grids. Therefore, unstructured grids should only be applied when curvilinear grids do not suffice. This can be for example at land boundaries or at a transition between a lower resolution part and a higher resolution part.

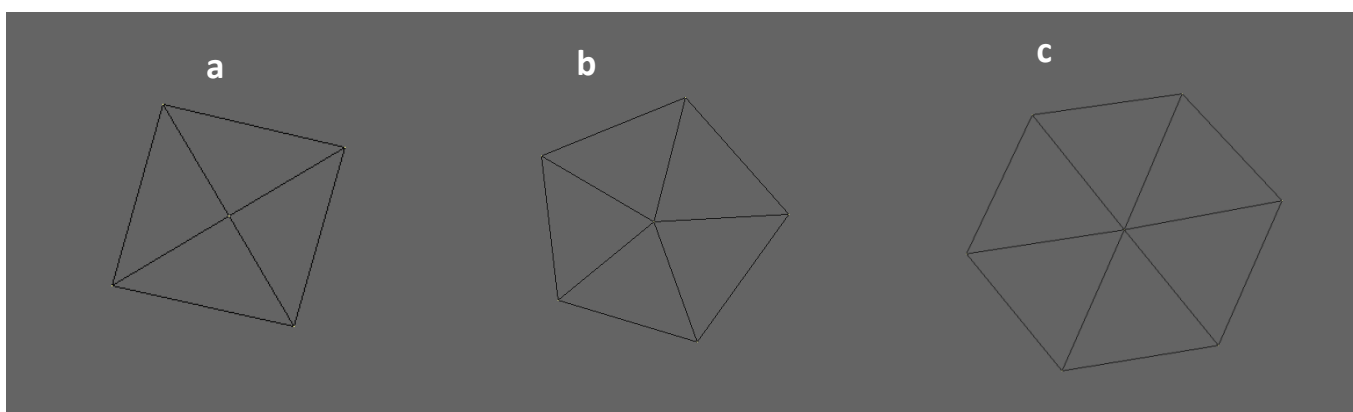


**Figure A-6: Three styles of grid building. (a) A square with a netnode in its center, this yields with perfect orthogonality 4 triangles of 90 degrees and hence should be avoided. (b) A pentagon with a netnode in its center, yielding 5 triangles with angles of 72 degrees near the center node and this is hence a good structure in a grid. (c) A hexagon with a netnode in its center, yielding 6 equilateral triangles when the orthogonality is perfect and hence this is the preferred structure in a grid with triangular cells.**

Taking all the aforementioned things into account it can be realized that different kinds of structures should be avoided or stimulated when building a grid. Figure A-5 displays 3 such structures. The square should be avoided, as they result in 4 right triangles. The pentagon is a good structure, as it yields triangles with angles smaller than 90 degrees. The hexagon is the preferred structure when building grids with triangular cells, because with perfect orthogonality it yields equilateral triangles. Other regular polygons with more than 6 sides (the maximum amount of sides is 8) are good structures as well, but it is best to not deviate from the 6-sided polygon too far. See also Figure A-6 for a clear image of these structures in a grid with very high orthogonality.

Another important thing to watch that does not really have to do with grid building but is nevertheless important has to do with the locations of the observation points. These points are specified by the user. Despite the fact that the specification provides the coordinates for this station, the measured quantities like sea level and velocity are taken from the nearest flownode. This leads to x and y coordinates that do not belong with the measured quantities with inaccuracies as a result. This problem will not be fixed in the near future.

## Appendix B. The collocation method

Recall the equation for  $u$  in a rectangular basin enclosed on three sides by walls (equation (23))

$$u = \Re \left\{ \frac{Z}{H} c_0 \left( R e^{-\frac{y}{a}} e^{i(kx-\sigma t)} - e^{-\frac{B-y}{a}} e^{-i(kx+\sigma t)} \right) + u_n \right\}. \quad \text{i)}$$

At the boundary  $x=0$ , this equation reduces to

$$0 = -Z \left[ e^{-\frac{B-y}{a}} - R e^{-\frac{y}{a}} \right] + \sum_{n=1}^{\infty} Z_n \left[ \frac{i c_0 s_n}{\sigma} \cos\left(\frac{n\pi y}{B}\right) - \frac{fB}{n\pi c_0} \sin\left(\frac{n\pi y}{B}\right) \right]. \quad \text{ii)}$$

The unknowns in this equation are  $R$  and  $Z_n$ . They can be solved by applying a so called collocation technique. This technique assumes that equation (ii) is obeyed at a finite number of collocation points  $y=(j-1)*B/N$ . Since both  $R$  and  $Z_n$  need to be solved, the expansion of equation (ii) into  $(N+1)$  equations can only solve for  $N$  trapped Poincaré waves. The resulting system of equations can be written in matrix form:  $A * X = E$ . In this equation

$$A = \begin{pmatrix} Z e^{-\frac{(1-1)B}{Na}} & D(1,1) & \dots & D(1,n) \\ Z e^{-\frac{(2-1)B}{Na}} & D(2,1) & \dots & D(2,n) \\ \vdots & \vdots & \ddots & \vdots \\ Z e^{-\frac{(N)B}{Na}} & D(j,1) & \dots & D(j,n) \end{pmatrix}, X = \begin{pmatrix} R \\ Z_1 \\ Z_2 \\ \vdots \\ Z_n \end{pmatrix}, E = \begin{pmatrix} Z e^{-\frac{B-(1-1)*\frac{B}{N}}{a}} \\ Z e^{-\frac{B-(2-1)*\frac{B}{N}}{a}} \\ \vdots \\ Z e^{-\frac{B-(N)*\frac{B}{N}}{a}} \end{pmatrix}, \text{ and}$$

$$D(j,n) = \left[ \frac{i c_0 s_n}{\sigma} \cos\left(\frac{n\pi(j-1)}{N}\right) - \frac{fB}{n\pi c_0} \sin\left(\frac{n\pi(j-1)}{N}\right) \right].$$

In these matrices  $E$  represents the incoming Kelvin wave, the first column of  $A$  represents the outgoing wave and  $D(j,n)$  represents the trapped Poincaré waves. This equation can then be solved by matrix division (numerically or analytically). For the relatively simple case that  $N=2$ , there are 3 equations with three unknowns  $R$ ,  $Z_1$  and  $Z_2$ . The analytical solution to this set of equations is

$$R = \frac{c_0^2 \pi s_1 \left(1 + e^{\frac{B}{2a}}\right) - i B f \sigma \left(1 - e^{\frac{B}{2a}}\right)}{c_0^2 \pi s_1 \left(1 + e^{\frac{B}{2a}}\right) + i B f \sigma \left(1 - e^{\frac{B}{2a}}\right)}, \quad \text{iii)}$$

$$Z_1 = \frac{-c_0^2 \pi \sigma e^{-\frac{B}{a}} \left(-1 + e^{\frac{B}{2a}}\right) \left(1 + e^{\frac{B}{2a}}\right)^2}{B f \sigma \left(-1 + e^{\frac{B}{2a}}\right) + i c_0^2 \pi s_1 \left(1 + e^{\frac{B}{2a}}\right)}, \quad \text{iv)}$$

$$Z_2 = \frac{-B \pi \sigma^2 e^{-\frac{B}{a}} \left(-1 + e^{\frac{B}{2a}}\right) \left(1 + e^{\frac{B}{a}}\right)}{c_0 s_2 \left( c_0^2 \pi s_1 \left(1 + e^{\frac{B}{2a}}\right) + i B f \sigma \left(1 - e^{\frac{B}{2a}}\right) \right)}. \quad \text{v)}$$

For higher values of N these expressions change somewhat. The numerical values for the coefficients show a convergence for increasing N. Figure B-1 shows that the reflection coefficient is approximately constant when  $N > 6$ . This validates the truncation of the trapped Poincaré waves at an

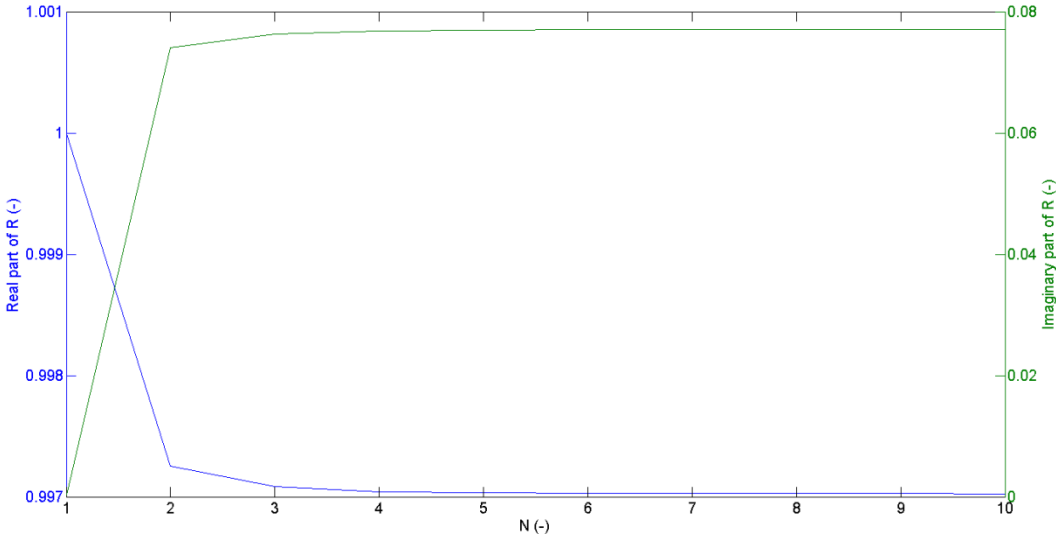


Figure B-1 The imaginary and real parts of the reflection coefficient R as a function of N.

N value of 12.

## Appendix C. Details of the alpha amphidromic points

An alpha line is defined as a line that indicates zero water levels across the domain at a single time step. The intersection between two alpha lines is the only location where the water level is zero at both time steps. Therefore, in the analytical solution, the location of the intersections between all alpha lines is the same and equal to the location of the range amphidromic point.

To illustrate this, Figure C-1 shows the sea surface amplitude as a function of the along channel distance at different time steps and the maximum tidal range averaged over a tidal period. In this figure the analytical solution has been used. The point where 2 blue lines intersect is the point where the sea surface amplitude is equal at both time steps. Since in this figure the line  $y=1/2 B$  is displayed and hence includes the location of the amphidromic point, all lines intersect at  $\eta = 0$ .

The range point definition has the advantage to be close to the original definition of the amphidromic point (or even the same when only a single component is regarded), but the alpha point definition is useful because there are multiple alpha lines and hence multiple intersections. Ideally, in the absence of other components, both definitions would yield the same solution, but in the case where the tide does not consist of a single component, as is the case with the numerical models, the intersections between alpha lines are bound to have different locations. Hence, by taking the mean and standard deviations, a measure of ‘spread’ of the ‘amphidromic’ point of the total solution is obtained. This spread is a measure for the area in which the amphidromic point or ‘area’ is located.

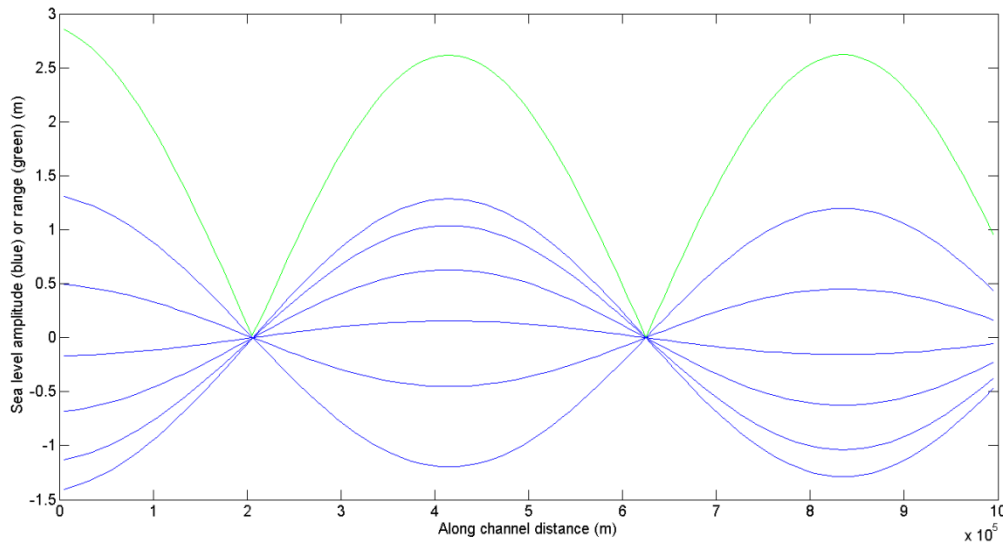


Figure C-1: A cross-section of analytical solution of the rectangular basin at  $y=1/2 B$ . Blue lines display the sea surface along the channel at a few random time steps. Green lines display the maximum tidal range of a tidal period.

The methods to find the alpha and range amphidromic points differ considerably. For the alpha amphidromic points the coordinates of the lines  $\eta = 0$  were obtained and interpolated using Matlab functions. From all intersection points found this way the mean and standard deviations were computed.

For the range points a quadratic relation of the second degree in the 9 points closest to the amphidromic points was assumed. This means in both  $x$  and  $y$  directions. The coefficients of this equation have subsequently been computed using Matlab’s curve fitting toolbox. From these

coefficients it is possible to, using the derivatives in the x and y direction of the quadratic equation, find the location of the minimum value of this curve (see also section 2.4.2).

The difference between the range and alpha amphidromic point method makes itself clear in the differences between the green and blue lines. The tidal range is not exactly zero in the first amphidromic point and its minimum is not at the intersection of the blue lines, which is due to the effect of trapped Poincaré waves which move the amphidromic point slightly away from the predicted value. Since this is the analytical solution, this difference is not really present, but because there is no grid point at the exact x-location of the amphidromic point, the different numerical interpolations have different results. At the second amphidromic point the two different amphidromic point methods match, because here the influence of the trapped Poincaré waves is negligible.

## Appendix D. Grids used for modeling the Arabian Gulf

Figure D-1 displays the grid that was built by ARCADIS. This figure is identical to Figure 4-1 but in this

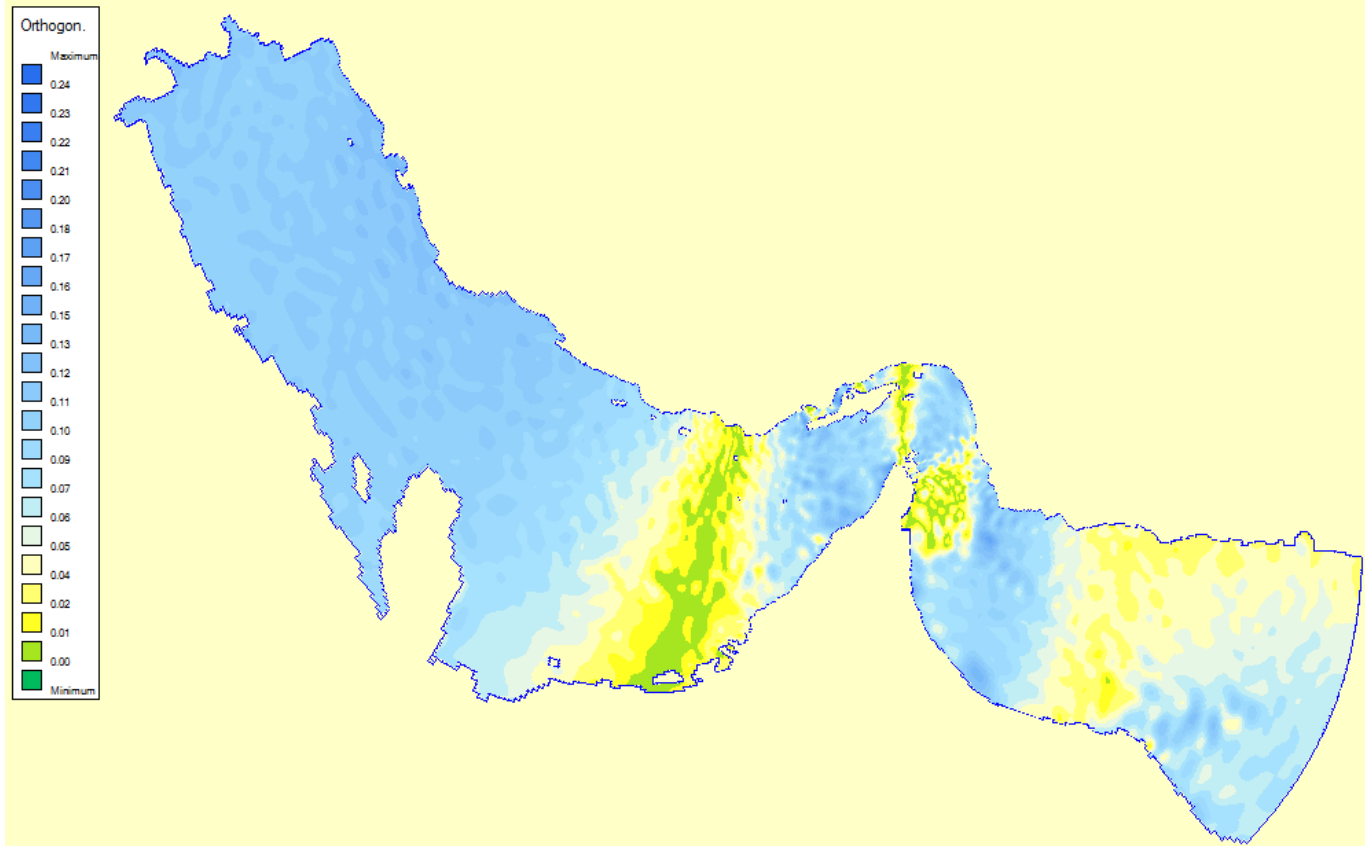


Figure D-1: The orthogonality of the Delft3D grid that was built by ARCADIS.

figure the colors indicate the orthogonality. When recalling Appendix A, it can be seen that the orthogonality of this grid is substantially (more than 10 times) higher than the standards. That is because at the moment when this grid was created it was not yet possible to orthogonalize grids in

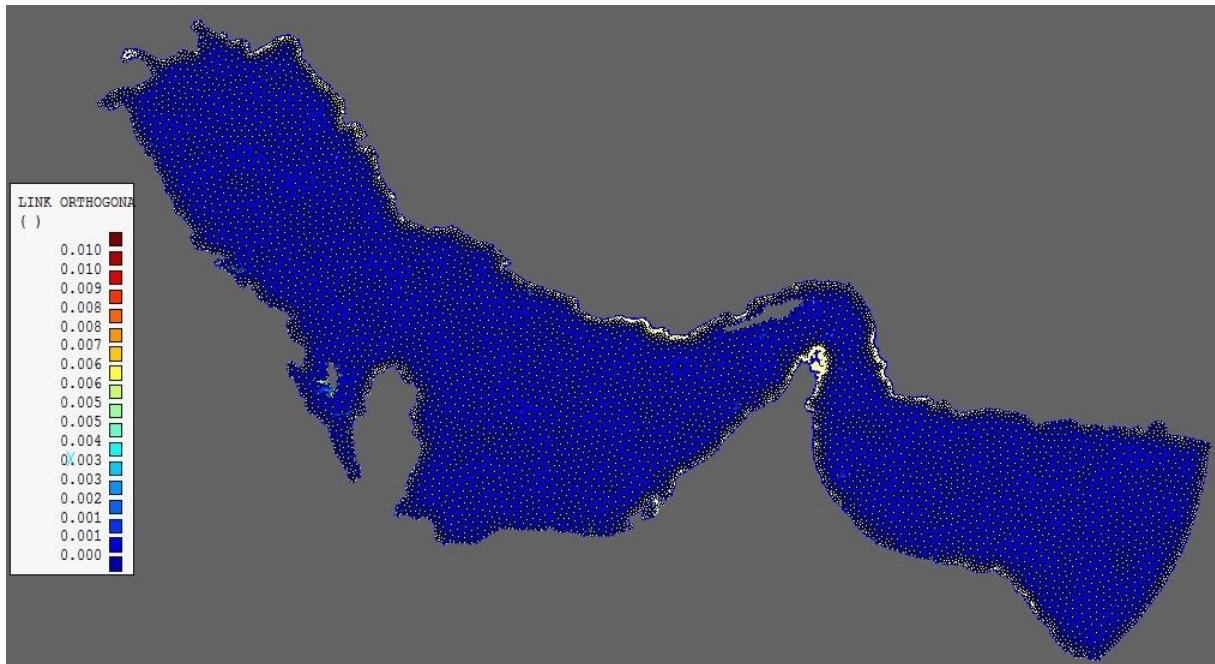


Figure D-2: The orthogonality of the grid with using triangular cells as built with D-Flow FM.

spherical coordinates. Therefore, this grid was orthogonalized in Cartesian coordinates and then converted to spherical coordinates. Because this model was calibrated for this grid, and this grid has proven to function properly in many studies, in this study no efforts were made to improve the orthogonality. In D-Flow FM the grid with triangular cells did not exist prior to this study, and therefore the orthogonality is much lower (see Figure D-2). This grid consists primarily of triangles, but it has some square cells as well. Due to time constraints this grid has not been calibrated to yield optimal results. For better model results for future projects it is therefore recommended to do this before running a model with this grid.

## Appendix E. Tidal motion in the Arabian Gulf

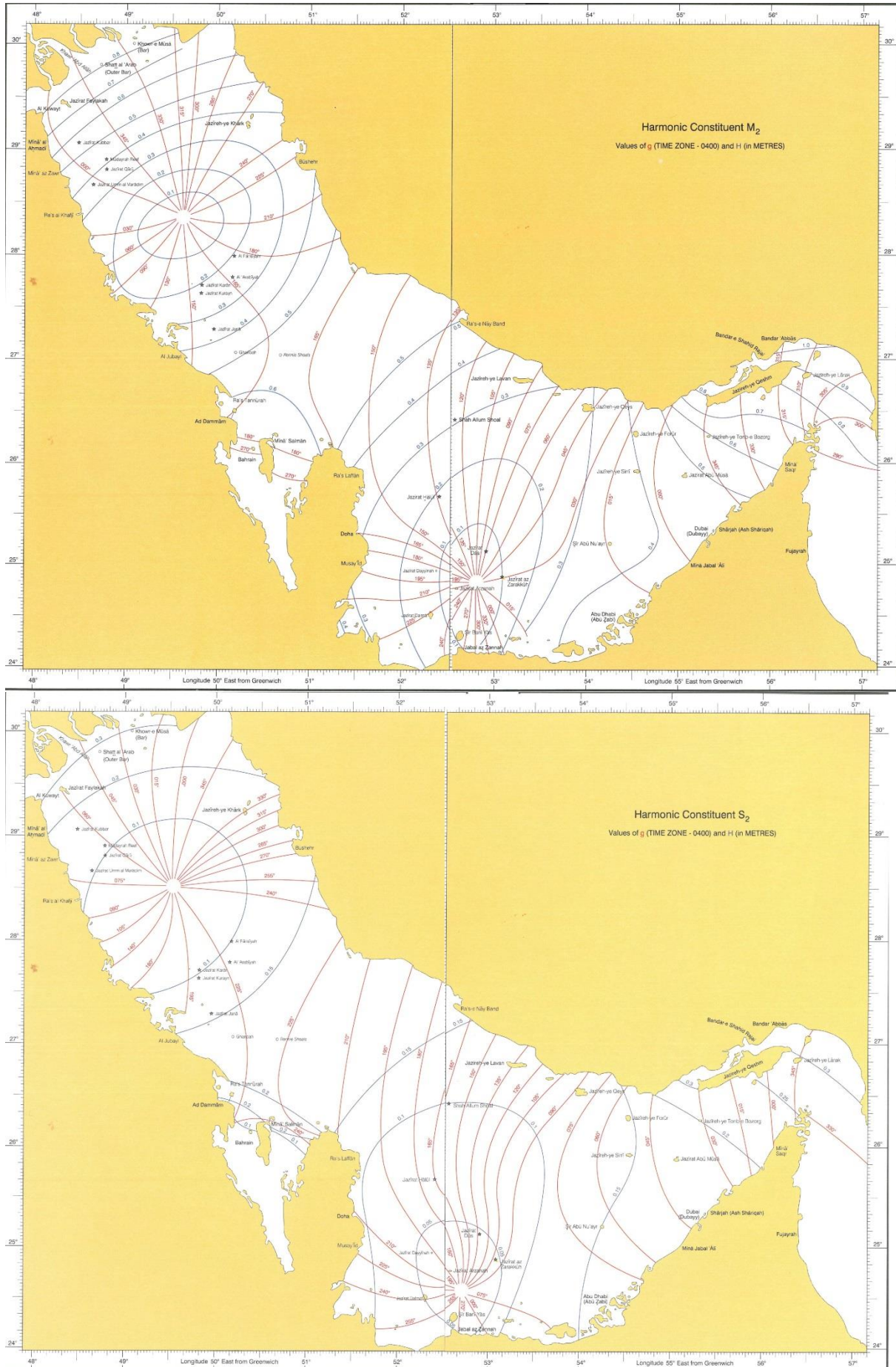


Figure E-1: The co-phase lines (in red) and the co-amplitude lines (in blue) of the  $M_2$  (top panel) and  $S_2$  (lower panel) tide in the Arabian Gulf. From: (Admiralty co-tidal Atlas Persian Gulf, 1999).

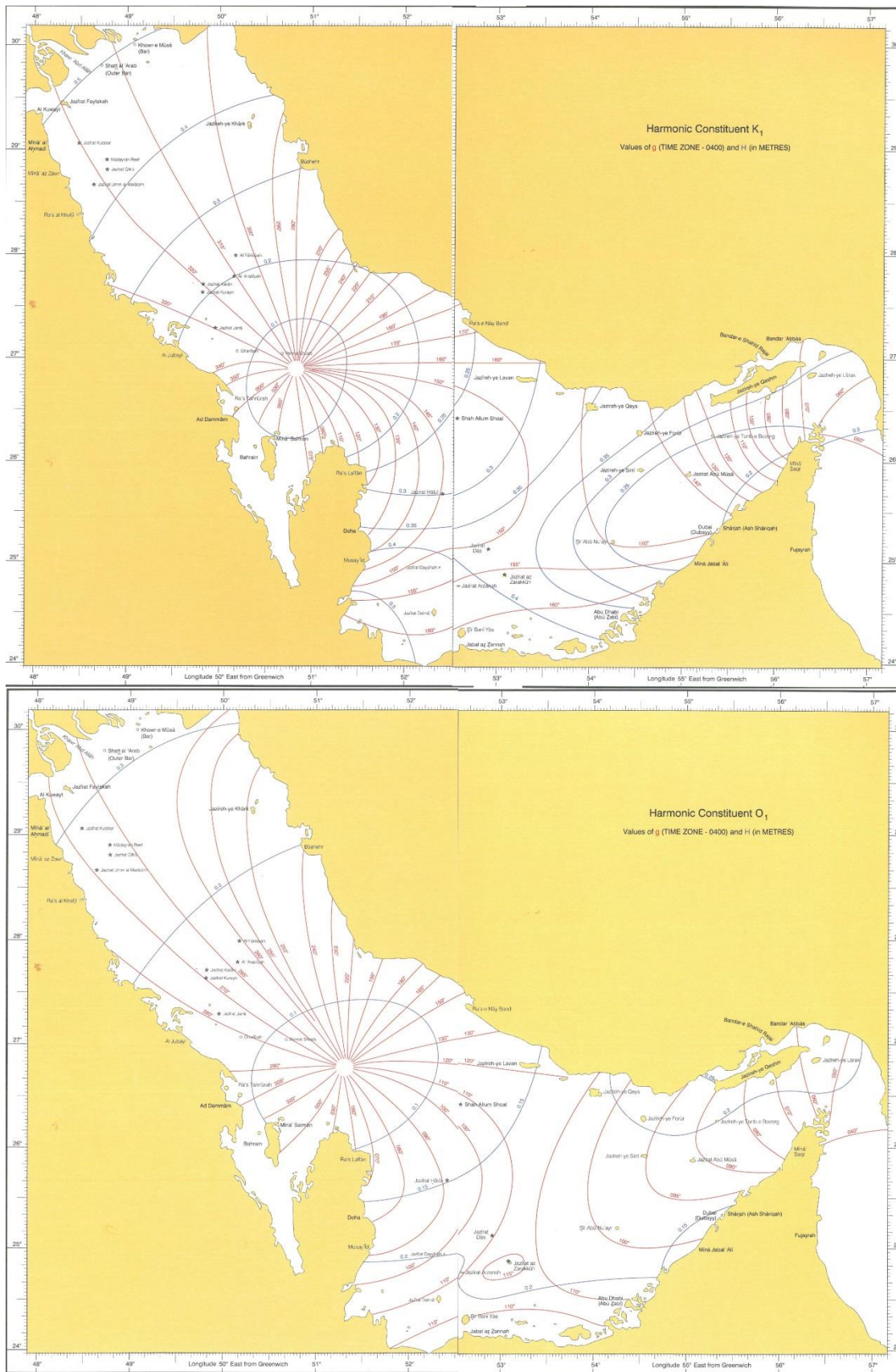


Figure E-2: The co-phase lines (in red) and the co-amplitude lines (in blue) of the  $K_1$  (top panel) and  $O_1$  (lower panel) tide in the Arabian Gulf. From: (Admiralty co-tidal Atlas Persian Gulf, 1999).

Admiralty co-tidal Atlas Persian Gulf (1999) shows the amplitudes and phases of the 4 major tidal components in the Arabian Gulf as deduced from observations. The first of these figures is an enlargement of Figure 2-2. Below these four figures are figures similar to Figure 4-3, but now for the other three major components.